Fluid mechanics of the inner ear

Fluid Mechanics of the Inner Ear

Dominik Obrist

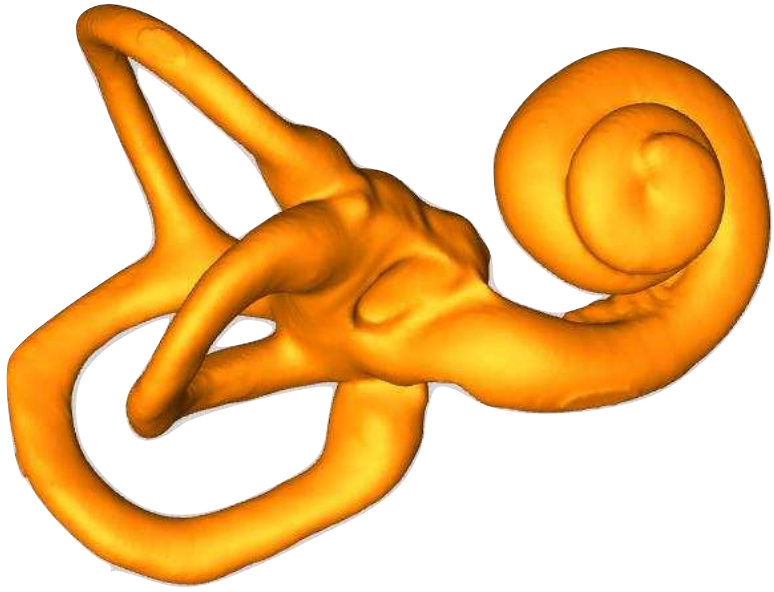

"Fluid Mechanics of the Inner Ear"

Habilitation treatise in Fluid Mechanics at the Department of Mechanical and Process Engineering of ETH Zurich

by

Dominik Obrist, Institute of Fluid Dynamics, ETH Zurich

November 2011

Figure on the title page: μCT visualization of the bony labyrinth of a human inner ear (in collaboration with Prof. A. Huber, Dept. Otorhinolaryngology, University Hospital Zurich and the Institute for Biomechanics, ETH Zurich).

Contents

Preface

This monograph is submitted as a habilitation treatise ("Habilitationsschrift") to the Department of Mechanical and Process Engineering of ETH Zurich. It is a compilation of my work on the fluid mechanics of the inner ear over the past six years. Next to unpublished material and new ideas, this monograph contains material from a number of journal articles, conference proceedings and lecture notes by the author and his co-workers. Some of the presented results were the outcome of Bachelor, semester or Master projects at ETH Zurich performed by the many excellent students whom I had the pleasure to supervise. Finally, I added some results from other authors in order to provide the reader with a more complete picture of our current knowledge on flow phenomena in the inner ear.

Nevertheless, I certainly cannot claim by any means to present a complete and/or conclusive account of the fluid mechanics of the inner ear (although the title might suggest that). Rather, this monograph presents a snapshot of my current understanding of this topic. In particular, in the field of cochlear mechanics the present knowledge is much broader than presented here. In some chapters (e.g. chapters 19 & 21) I have tried to provide some forward-looking information as a guideline for future research.

The monograph is divided into three parts: I. the semicircular canals, II. the cochlea and III. coupled phenomena. There is a total of twenty-three rather short chapters. I have tried to write them in a self-contained manner such that the advanced reader should be able to read them independently. Therefore, certain facts and ideas are repeated in different chapters. For beginners in the field of biomechanics of the inner ear, I suggest to read the chapters in the suggested order as they build up on each other.

Zurich, November 2011 Dominik Obrist

CHAPTER 1

Introduction

The relevance of the research on the inner ear has been recognized for a long time. This is best reflected by two *Nobel prices in physiology or medicine* that were awarded in 1914 to *Robert Bárány* for his "work on the physiology and pathology of the vestibular apparatus" and in 1961 to *Georg von Békésy* for his "discoveries of the physical mechanism of stimulation within the cochlea" (figure 1.1).

The scientific recognition of inner ear research goes along with an increasing social relevance of this topic mainly because of demographic changes. The European Commission states that "by 2020 25% of the EU's population will be over 65. Spending on pensions, health and long-term care is expected to increase

(a) Robert Bárány, 1876–1936

(b) Georg von Békésy, 1899–1972

FIGURE 1.1. Nobel laureates Robert Bárány and Georg von Békésy.

by 4-8% of GDP in coming decades, with total expenditures tripling by 2050"[1]. Promoting health in an aging society is one of today's grand challenges in science and engineering.

One important aspect of human health is the hearing and the balance sense whose primary sensors constitute the inner ear. Apart from various non-age related hearing problems, a progressive hearing loss due to age is definitely a health issue of growing prevalence in our society. Likewise, the most prevalent form of vertigo (benign paroxysmal positional vertigo, BPPV) can be found predominantly in elderly people (over 9% of the US population beyond the age of seventy; Baloh *et al.*, 1989). While hearing loss and/or vertigo are not life threatening diseases, the proper operation of our senses has a strong social and economical relevance. Especially in the western hemisphere, a healthy hearing sense at all stages of our life is regarded as important for maintaining our life style.

Along with the desire for a good hearing, several technology-driven companies develop and manufacture hearing aids of various kinds. A new generation of hearing aids (micromechanical devices such as middle-ear implants, etc.) work directly on or inside the inner ear with various actuator technologies. The technological challenges for such devices are very different from conventional hearing aids which emit the amplified and modulated sound signal via a loudspeaker into the ear canal and which do not interfere directly with the inner ear. To design inner ear devices with good performance, it is not sufficient to understand the inner ear only as a black-box because these devices modify the mechanics of the inner ear itself. Therefore, the different phenomena involved in the mechanics of the inner ear have to be resolved and described by appropriate physical models.

1. The inner ear

The human ear consists of three parts: the outer ear, the middle ear and the inner ear (figure 1.2). The present work addresses only the inner ear which is an anatomically complex structure of only about a centimeter in size (figure 1.3). In addition to the hearing sense, the inner ear also hosts the primary sensors of our balance sense. The different functions can be assigned to principal anatomical structures of the inner ear:

(i) **hearing sense:** the coiled cochlea is able to decompose an acoustic signal into its frequency components.
(ii) **balance sense:** the vestibular apparatus hosts five sensors which are able to detect angular and linear accelerations in all directions.
  (a) **angular:** the three semicircular canals transduce angular accelerations of the head into an angular velocity signal.

[1] `http://ec.europa.eu/information_society/newsroom/cf/itemlongdetail.cfm?item_id=3457`; last accessed 18 November 2011.

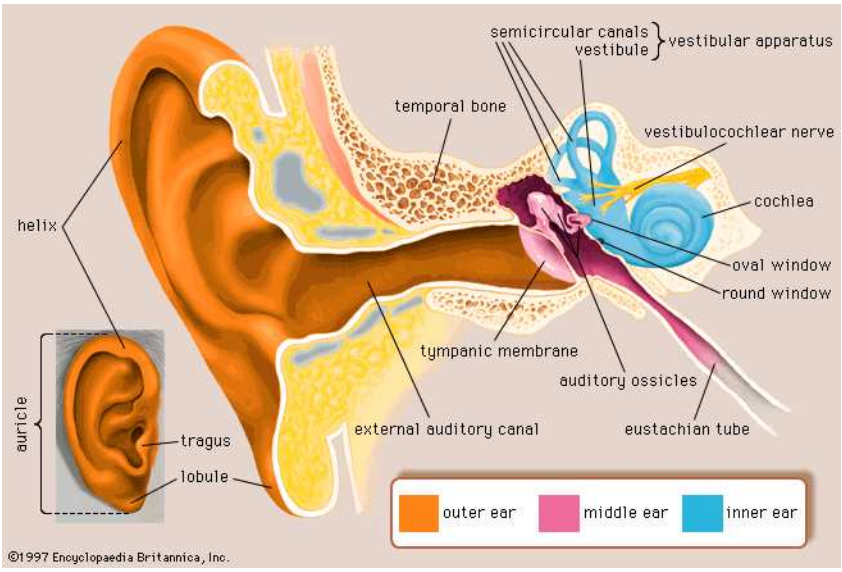

FIGURE 1.2. The human ear.

(b) **linear:** the vestibule hosts the two otolith organs (in the utricle and the saccule) which are able to detect linear accelerations and gravity.

Apparently, this small organ has to serve multiple purposes. This diversity is reflected by a surprisingly large variety of physical phenomena present in the inner ear.

We will put our focus on the fluid mechanics of the inner ear. Nevertheless, our considerations will also include other physical processes (e.g. solid mechanics, electrochemical processes) without which the physiology of the inner ear could not be understood. In that sense, we regard the inner ear as a multi-purpose and multi-physics system. Moreover, it is also a multi-scale system with respect to temporal as well as spatial scales. We will see in the following chapters that typical time scales range from less than 0.1 μs (high-frequency hearing) to several seconds (mechanical adaptation of the angular balance sense) and that length scales of less than a nanometer (membrane displacements at the hearing threshold) co-exist with large scales of up to 35 mm (length of the uncoiled cochlea).

To the present day, our understanding of the anatomy and physiology of the inner ear is incomplete. Moreover, many pathological conditions of high social relevance (e.g. various forms of hearing loss and vertigo) are not properly understood. This goes along with a need for better therapeutic measures (e.g.

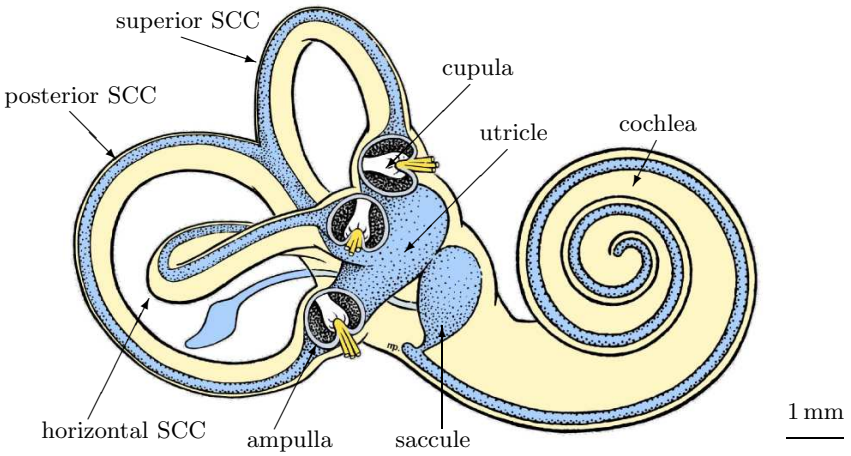

FIGURE 1.3. Schematic of a human inner ear (from Obrist *et al.*, 2010) with the membranous labyrinth (blue) which is filled with endolymph and the bony labyrinth (yellow) filled with perilymph. The width of the slender ducts in the semicircular canals is exaggerated for better visibility. In reality, their diameter is only about 5% of the major diameter of the bony canal (Curthoys *et al.*, 1977*b*).

fully implantable hearing devices) which can only be properly developed once the (patho-)physiology of this organ is sufficiently understood.

2. Challenges when studying the inner ear

Apart from its small size, the main difficulty in studying the inner ear is its location and (in-)accessibility in the human body. Unlike other organs (e.g. heart, lung, eye) the principal structure of the inner ear is not a proper body of its own, but rather a void inside a very dense bone known as the temporal bone. Except for the oval and round windows which connect the inner ear to the middle ear, there exists no practicable access to the inner ear other than access by destruction of the surrounding temporal bone. For this reason, many clinical investigations use secondary phenomena to study the physiology of the inner ear (e.g. the vestibulo-ocular reflex for the balance sense, and psychoacoustic measurements for the cochlea). Direct measurement of physical quantities within the inner ear are very limited and experimentally demanding, e.g. intracochlear

pressure measurements (Nakajima *et al.*, 2009) or in vivo canalith settling in semicircular canals (Rajguru & Rabbitt, 2007).

These practical limitations open the field for theoretical, numerical as well as in vitro experiments which are the primary methods of investigation used in the present work. All three approaches involve the modeling of the functional units of the inner ear. This requires invariably a number of idealizations, simplifications and sometimes even guesswork because certain anatomical features and/or rheological properties are simply not known. Moreover, the multi-scale aspect of the inner ear results in formidable challenges, in particular, for numerical models of the physiological processes.

To address the challenges listed above, we will begin our study of the involved physical processes on the basis of dimensionless numbers and/or integral time scales. We will try to identify appropriate scale separations which allow us to formulate models with manageable complexity. We will find, for instance, that the balance sense can be appropriately modeled, to first order, as a quasi-steady system whereas the operation of the hearing sense is based on highly unsteady phenomena. Therefore, there exists a clear separation of temporal scales between the two senses. This separation is not only relevant for the modeling, it is also physiologically important because the anatomy of the inner ear provides no topological separation between the sensorium of the balance sense and of the hearing sense. As a matter of fact, the sensory hair cells of the respective senses are located in corresponding vessels, i.e. all sensory epithelia of the inner ear are situated within a single endolymphatic fluid space (depicted in blue in figure 1.3). In part 3, we will discuss certain pathologies of the inner ear (e.g. superior canal dehiscence) for which the scale separation between the balance and the hearing sense is disturbed such that we can observe crosstalk between the senses (e.g. Tullio's phenomenon).

3. Overview on the anatomy and physiology of the inner ear

Detailed discussions of the anatomy and the physiology of the inner ear will be given in the respective chapters. Here, we give just a rough anatomical overview to introduce the most important components and mechanisms in the inner ear.

3.1. Lymphatic fluids. The inner ear is filled with two lymphatic fluids: the endolymph and the perilymph (figure 1.3). They are separated from each other by a thin membrane. This membrane forms the so-called *membranous labyrinth* which is filled with endolymph (blue in figure 1.3), in contrast to the *bony labyrinth* which marks the outer bounds of the inner ear.

The flow field of the endolymph is central to the function of the angular balance sense. The perilymphatic fluid space is not regarded as playing a significant

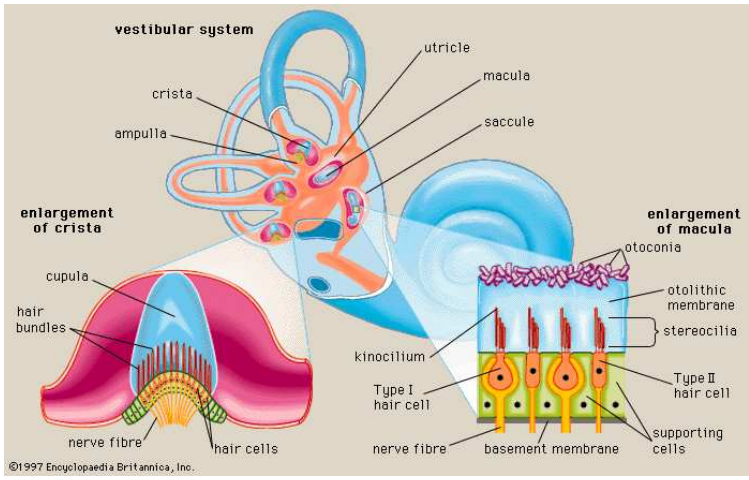

FIGURE 1.4. Sensory epithelia of the vestibular system.

role in the vestibular system (semicircular canals and otolith organs). However, it plays a central role in the cochlea, i.e. in our hearing sense.

The endolymph and the perilymph differ in their ion content. The endolymph has a high content of potassium ions, K^+, such that there exists an electrical potential across the separating membrane. This potential is relevant for the proper operation of the sensory hair cells which have the primary role of transducing mechanical displacements into afferent nerve signals and may even play the role of an active amplifier (outer hair cells of the cochlea). From a purely mechanical point of view, both lymphatic fluids behave like water.

Topologically, there exist just two distinct fluid spaces (figure 1.3). Nevertheless, we can further differentiate the structures of the inner ear based on their morphology and function.

3.2. Vestibular system: Semicircular canals. The membranous ducts of the three semicircular canals (SCC) issue directly from the utricle (figure 1.3). The mutually orthogonal toroidal structures of the SCC feature bulges on one side before converging into the utricle. These bulges are called ampullae and host the cupula (figure 1.4) which is a soft gelatinous membrane that blocks the whole lumen of the endolymphatic ducts. Sensory hair cells are embedded into the cupula.

Under angular motion the inertia of the endolymph in the semicircular canals leads to a deflection of the cupula. This activates sensory hair cells in the cupula leading to afferent nerve signals. For our purposes, it is sufficient to assume

that the sensation of angular motion is roughly proportional to the deflection of the cupula. The relationship between mechanical stimulation and afferent nerve discharge in the cupula is discussed in detail in Yamauchi *et al.* (2001) and Highstein *et al.* (2005).

3.3. Vestibular system: Otoliths. In the central vestibule of the inner ear, the endolymphatic fluid space forms two sacs (saccule and utricle) which contain the sensory maculae (figure 1.4) of the otolith organs. The stereocilia of the otolithic hair cells reach into a gelatinous membrane with otoconia (calcite crystals) sitting on top.

From a mechanical point of view, the otolith organs operate like technical accelerometers. Linear accelerations of the head result in inertial forces acting on the otolithic membrane because the otoconia are heavier than the surrounding endolymph. These inertial forces deform the membrane which leads to a stimulation of the hair cells beneath. Classically, the mechanics of the otolith organs is seen as independent of the flow in the utricle and/or saccule. Only recently, our group (Boselli *et al.*, 2010*c*) has shown that angular accelerations of the head causes a vortical flow inside the utricle which may lead to shear stresses on the utricular macula above its sensation threshold.

3.4. Cochlea. The human cochlea is a small but complex coiled structure with an uncoiled length of approximately 35 mm. It consists of three fluid filled ducts: the scalae vestibuli and tympani which are filled with perilymph and the scala media filled with endolymph (figure 1.5). The three main ducts of the cochlea are separated by two membranes (figure 1.6): Reissner's membrane (RM) and the basilar membrane (BM). While Reissner's membrane is a very supple structure, the basilar membrane's stiffness leads to resonance phenomena at acoustic frequencies.

The base of the scala vestibuli communicates with the middle ear through the oval window (OW). At its far end, i.e. at the cochlear apex, the scala vestibuli connects to the scala tympani through a hole known as the helicotrema (H). At the base of the cochlear coil, the scala tympani connects mechanically to the middle ear through the membrane of the round window (RW).

The scala media contains the organ of Corti (OC) which is by itself a very complex fluid-filled system whose internal mechanisms are not fully understood. It includes several membranes, structural elements, fluid spaces and two types of hair cells (figure 1.7). These hair cells fill several roles in our hearing sense. Primarily, they act as mechanotransducers from acoustic to nerve signals. The acronyms for the cochlear anatomy are summarized in table 1.1.

The cochlea performs a 'real-time Fourier transform' on acoustic signals. These enter the inner ear primarily through the oval window by vibrations of

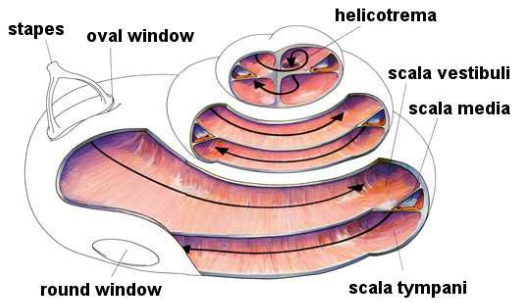

FIGURE 1.5. Coiled human cochlea (adapted from `www.tz-wien.at/Informationen/wiefunktioniertdashoren.htm`).

TABLE 1.1. List of anatomical acronyms for the inner ear.

SCC	semicircular canal	figure 1.3
BM	basilar membrane	figure 1.6 & 1.7
TM	tectorial membrane	figure 1.6 & 1.7
OW	oval window	figure 1.5
RW	round window	figure 1.5
H	helicotrema	figure 1.5
OHC	outer hair cell	figure 1.7
IHC	inner hair cell	figure 1.7
OC	organ of Corti	figure 1.6 & 1.7

the stapes (the third ossicle of the middle ear; figure 1.2) which lead to a pulsating flow of the perilymph in the axial direction of the cochlea. Because the walls between the perilymphatic ducts and the scala media are compliant, the pulsating flow results in a traveling wave in the perilymph and on the basilar membrane. The stiffness of the basilar membrane is strongly graded in axial direction (stiffer at the base) partly due to its local mechanical properties and partly due to an increasing width of the BM. Therefore, the magnitude of the traveling wave has a distinct peak where the stimulation frequency is in resonance with the local mechanical properties of the basilar membrane and its surrounding fluid. This (passive) frequency selection process is in tight interaction with active processes in the organ of Corti which lead to a nonlinear amplification of the oscillating basilar membrane.

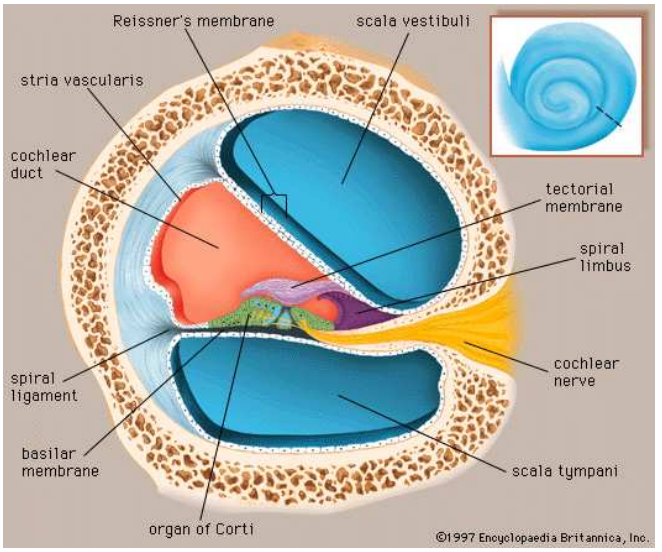

FIGURE 1.6. Cross section through the cochlear ducts (scalae vestibuli, tympani and media) which are separated by Reissner's membrane (RM) and the basilar membrane (BM). The organ of Corti (OC) is located within the scala media.

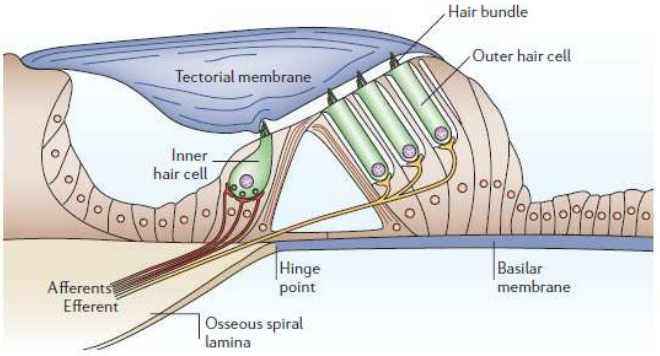

FIGURE 1.7. Sketch of the Corti organ with inner (IHC) and outer hair cells (OHC), the tectorial membrane (TM) and the basilar membrane (BM). Reprinted from Fettiplace & Hackney (2006) with permission from the publisher.

4. Scope and organization of this monograph

This monograph focuses exclusively on the (patho-)physiology of the inner ear as it relates to fluid mechanics. In general, numerical and experimental methods and biomedical details will not be discussed in detail; where appropriate, the reader is referred to the relevant publications.

The first part on the semicircular canals begins by introducing the physiology of this organ on the basis of a heuristic model (Chapter 2: Steinhausen's model). In Chapters 3, 4 & 5 Van Buskirk's model for semicircular canals will be studied in detail. It will help us to put the results from Steinhausen's model on a solid foundation. Chapter 6 completes our discussion of the fluid mechanics of healthy semicircular canals by presenting results obtained with modern methods of computational fluid dynamics. The remainder of the first part (Chapters 7– 11) is concerned with a pathology of the semicircular canals: benign paroxysmal position vertigo (BPPV) which is one of the most common causes for vertigo. We will study this disease on the basis of analytical (Chapter 8) and in vitro (Chapter 9) models. Results from these models are used in Chapter 11 to discuss a clinical phenomenon of BPPV.

The second part of this monograph is dedicated to cochlear mechanics. It has a strong focus on global cochlear modeling which indicates that we will study the cochlea as a complete system instead of studying the details of different subsystems of the cochlea. We present three cochlear models of increasing complexity: a one-dimensional passive model (Chapter 13), a two-dimensional passive model (Chapter 14) and a three-dimensional active model (Chapter 17). The presentation of these models is interspersed with a chapter on the modeling of active processes in the cochlea (Chapter 15) and two chapters on specific flow phenomena within the cochlea (Chapters 16 & 18). The final chapter of the second part presents a blueprint of a virtual cochlea which is a comprehensive multi-scale and multi-physics model of the complete cochlea.

The third part addresses the fact that the different sensory organs in the inner ear are in immediate neighborhood of each other and that they share the same fluid spaces. Chapter 20 explains how this apparent lack of separation between the organs is overcome in human physiology such that most humans have a properly working balance and hearing sense. Chapters 21 & 22 discuss two examples where the separation between the organs is insufficient such that we observe a sensory crosstalk.

Chapter 23 concludes this monograph with a discussion biomedical applications of the presented results and models as well as an outline of thoughts and ideas for a comprehensive mechanical model of the inner ear.

Part 1

The Semicircular Canals

CHAPTER 2

Introduction to the fluid mechanics of semicircular canals

The semicircular canals (SCC) are part of the vestibular system (figure 1.2). They belong to the balance sense and are responsible for sensing rotations. In each ear there are three semicircular canals which are oriented in mutually orthogonal directions. The canals are carved in bone and are filled with *perilymph* and *endolymph*, two fluids with mechanical properties similar to water. The endolymph and the perilymph are separated by a membranous duct. At one end of each semicircular canal there is the *ampulla* which contains the *cupula* (figure 1.4). The cupula is a gelatinous structure which fills the entire cross-section of the canal such that the flow of the endolymph is blocked (McLaren & Hillman, 1976). All three canals connect to the *utricle*, a larger chamber which also contains one of the sensors for linear motion.

The fluid dynamics in the semicircular canals is the key to the proper operation of the sensor for angular motion. Theoretical work on the fluid mechanics of SCC dates back to Breuer (1874), Crum Brown (1874) and Mach (1875). The actual discovery of the role of the vestibular organ as the main source of sensation of motion is due to Ewald (1892). Steinhausen (1933) was the first to postulate a mathematical description for the sensation of angular motion. This model will be discussed in § 2.

1. Basic physiology of semicircular canals

Angular acceleration of the head leads to inertial forces on the endolymph inside the membranous labyrinth. This generates a flow in the SCCs which is proportional to the angular acceleration in the plane of the respective canal. This flow deflects the cupula which acts as a temporal integrator such that the cupula deflection is (roughly) proportional to the angular velocity. Because the cupula is elastic, the cupula deflection leads to a restoring force pushing on the endolymph. This results in a slow mechanical adaptation process which lets the cupula return to its rest position if the angular velocity is held constant (zero acceleration) for a longer time.

When the cupula is deflected the sensory hair cells increase or decrease their firing rate depending on the orientation of the deflection. The brain determines the direction of the head rotation by vectorial summation of the inputs of all six SCC (from the left and the right ear) which results in the perception of angular motion. The perceived velocity signal leads to an eye movement which compensates for the head movement such that we are able to maintain our focus on an object while moving (figure 2.1). This is called the vestibulo–ocular reflex (VOR).

During continued angular motion in the same direction the eyes have to be reset at some point by quick eye movements. The repetitive pattern of slow compensatory movements (slow phases) and quick resetting movements (quick phases) is called *nystagmus*. We call the velocity of the compensatory eye movements (slow phase) the nystagmus velocity N. It is known that the nerve signal from the cupula is controlled and altered by several intricate mechanisms of the central nerve system before it is translated to the ocular muscles (Robinson, 1977; Cohen *et al.*, 1977; Raphan *et al.*, 1979). For the scope of our investigation, however, it is sufficient to simply assume that the volume V displaced cupula is proportional to the nystagmus velocity, $V \propto N$. The cupular volume displacement $V(t)$ is given as

$$V(t) = \int_0^t \iint_{A_c} u \,\mathrm{d}A \,\mathrm{d}\tau, \tag{1}$$

where u is the axial velocity component of the endolymph flow in the semicircular canal and A_c is the area of the cross-section of the canal.

The aim of most research on semicircular canals is to show under which conditions the cupular displacement is proportional to the angular velocity of the head. To this end, the nystagmus velocity is measured. It is found that the nystagmus velocity is nearly proportional to the angular velocity for oscillatory head movements in the horizontal and vertical planes with frequencies between 0.5 Hz and 5 Hz (Grossman *et al.*, 1988). This range covers the predominant frequencies occurring during natural head movements.

2. Steinhausen's model

Steinhausen (1933) modeled the dynamics of semicircular canals as a strongly damped torsional pendulum, i.e. the cupular displacement $V(t)$ is governed by an equation of the form

$$m\ddot{V} + r\dot{V} + kV = \ddot{\alpha}(t), \tag{2}$$

where $\ddot{\alpha}$ describes the angular acceleration of the head. The parameters r and k are the damping and stiffness parameters, respectively, whereas m reflects the mass of the fluid inside the SCC. The damping parameter r is mainly governed by the viscous drag of the fluid inside the slender ducts of the SCC whereas k

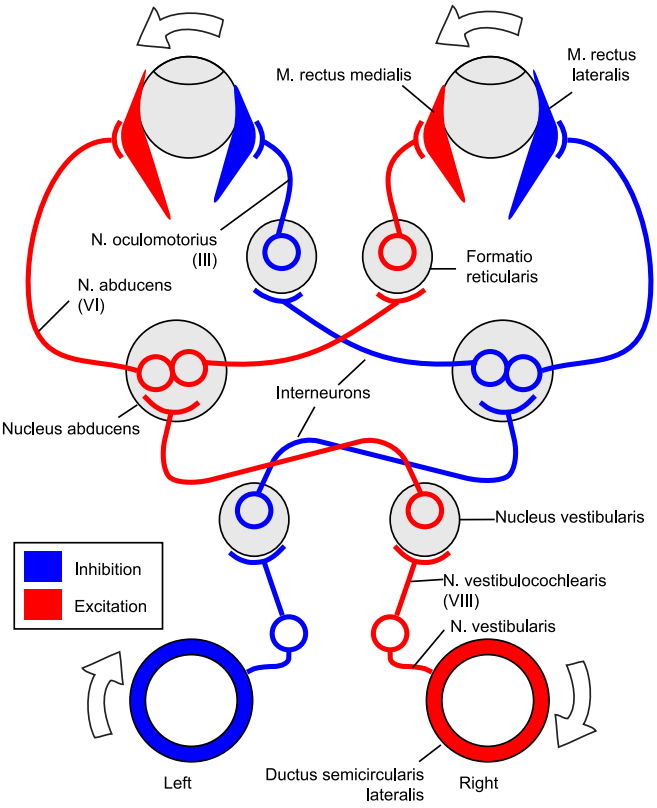

FIGURE 2.1. Schematic of the coupling between the SCC and the extraocular muscles (vestibulo–ocular reflex). The example shows a rotation of the head to the right with a compensatory eye movement to the left. (© .Koen / Wikimedia Commons / CC-BY-SA-3.0)

reflects the elasticity of the cupula. The eigenvalues of this second order system are given by

$$\sigma = -\frac{r}{2m} \pm \sqrt{\left(\frac{r}{2m}\right)^2 - \frac{k}{m}}. \tag{3}$$

If the damping is sufficiently weak, $r^2 < 4mk$, the two eigenvalues are complex valued such that Eq. (2) describes a damped oscillation. For $r^2 \ll 4mk$, the eigenfrequency of the oscillation is given by $\sqrt{k/m}$. Because of tje small diameter of the semicircular canals, approximately 0.3 mm, the damping parameter r is large. Therefore, we obtain two real valued eigenvalues and the system has no

eigenfrequency, i.e. it is an *overdamped* pendulum. The eigenvalues σ can be approximated as

$$\sigma_+ \approx -\frac{r}{m} \gg 1, \tag{4a}$$

$$\sigma_- \approx -\frac{k}{r} \ll 1. \tag{4b}$$

Although we will show in the following that Eq. (2) is not an accurate description of an SCC, Eq. (4) tells us that there exist two characteristic time scales of an SCC which are given by $|1/\sigma_\pm|$. The time scale $T_c = |1/\sigma_-| \approx r/k$ is the *slow time scale* of the SCC which is commonly known as the *cupula time constant*. It scales with the inverse stiffness of the cupula, i.e. the softer the cupula, the longer the cupula time constant. The *fast time scale* $T_v = |1/\sigma_+| \approx m/r$ relates the fluid inertia to its viscous forces. Later, we will refer to this time scale as the *viscous time scale*. Typical values for the cupula time constant are $T_c = 4.2\,\mathrm{s}$ (Dai *et al.*, 1999) but even values beyond 100 s have been reported (Rabbitt *et al.*, 2009). The viscous time scale T_v is on the order of $10^{-2}\,\mathrm{s}$.

The transfer function $G(s)$ which relates the cupula displacement V to the rotational head velocity $\dot{\alpha}$ can be written as

$$G(s) = \frac{ms}{(s - T_c^{-1})(s - T_v^{-1})}. \tag{5}$$

It describes a band pass filter as illustrated in figure 2.2. This indicates that the two time scales, T_c and T_v, define a frequency band within which the SCC transduce the angular head velocity $\dot{\alpha}$ *proportionally* into a cupular displacement V. It is worthwhile mentioning that the width of this frequency band increases with r, because r is in the nominator of T_c and in the denominator of T_v. Therefore, a high damping parameter r contributes to a large operating range of SCCs.

3. Further models of healthy semicircular canals

Steinhausen's model describes the main features of the dynamics of the semicircular canals. The values for the parameters of this simple macroscopic model, however, remain unclear. Several authors (e.g. Schmaltz, 1931; Van Egmond *et al.*, 1949) have tried to determine these parameters by assuming Poiseuille flow in the semicircular canals.

Van Buskirk & Grant (1973) and later Van Buskirk *et al.* (1976) departed from the macroscopic Steinhausen model and derived equations for the axisymmetric flow in the slender part of the canals directly from the Navier–Stokes equations. They derived a partial integro-differential equation which describes the axial velocity profile. The restoring force of the deflected cupula enters this equation in the form of a double integral. Oman *et al.* (1987) introduced a more complex description of the geometry of semicircular canals but remained with a

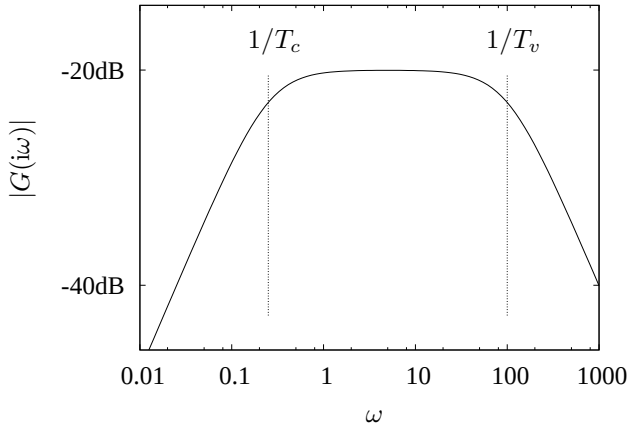

FIGURE 2.2. Bode diagram of the band pass filter defined by Steinhausen's model for the SCC. ($m = 1$, $T_c = 4$, $T_v = 0.01$)

one-dimensional model for the dynamics. Rabbitt & Damiano (1992) introduced a three-dimensional description of the SCC and found an asymptotic solution for the flow field. This work was followed by Damiano & Rabbitt (1996) who performed a detailed analysis of the flow field within the ampulla. They used the slenderness ratio (ratio between the minor and the major radius of the torus) as their asymptotic variable ϵ. The flow field in the slender part is considered the outer solution, whereas the flow in the ampulla is considered the 'boundary layer' or inner solution. The two solutions are asymptotically matched by balancing terms with equal powers of ϵ. They found that the flow in the slender part is barely influenced by the more complicated flow field in the ampulla. In other words, the dynamics of the endolymph is dominated by the viscous flow in the slender part of the canal. In retrospect, this important result is justification for the simplifications by Van Buskirk *et al.* (1976) who only looked at the flow in the slender part of the canal for which a constant circular cross-section was assumed. Ifediba *et al.* (2007) used the results of Damiano & Rabbitt (1996) to simulate and study the biomechanics of the complete 3-canal system. Obrist (2008) based his study on the model by Van Buskirk *et al.*. Whereas the latter used asymptotics to solve the equation, Obrist found an exact solution to the problem. He analyzed the eigenvalue spectrum of the model and used a modal expansion to give an explicit expression for the cupula displacement as a functional of the head maneuver. A recent overview on the biomechanics of SCC can be found in Rabbitt *et al.* (2004).

Although all these later investigations used different models and assumptions, they all agree with the basic dynamic features of Steinhausen's model (2) which postulates a overdamped system with two characteristic time scales.

CHAPTER 3

Van Buskirk's model of a semicircular canal

In this chapter, we present the model for the flow in semicircular canals proposed by Van Buskirk *et al.* (1976), hereafter referred to as VB. This model provides a solid fluid-mechanical foundation for research on semicircular canals. In the following Chapter 4, we will derive an exact analytical solution for this model.

For the purpose of the present investigation, we neglect the flow in the perilymph and consider only the endolymph and its surrounding membranous duct. Furthermore, we limit our investigation to a single semicircular canal which is a sensible simplification as long as we consider only head maneuvers in the plane of the respective semicircular canal. With this simplification the membranous duct has the topology of a torus. The slender part of the duct spans an angle β and has a constant circular cross-section of radius a which is much smaller than the main radius R of the torus (figure 3.1). The utricle spans an angle γ. The rotation angle $\alpha(t)$ is a function of the time t. It describes the actual head maneuver.

An observer moving with the canal perceives an axial fluid motion u relative to the canal. This fluid motion obeys the Navier–Stokes equations. In the slender part of the semicircular canal the axial component of the Navier–Stokes equations takes the simple form

$$\frac{\partial u}{\partial t} + R\ddot{\alpha} = -\frac{1}{\rho}\frac{\partial p}{\partial x} + \frac{\nu}{r}\frac{\partial}{\partial r}\left(r\frac{\partial u}{\partial r}\right), \tag{6}$$

where we have neglected the influence of curvature since $R \gg a$. In this equation $\ddot{\alpha}(t)$ is the angular acceleration, ρ is the fluid density, p is the pressure and ν is the kinematic viscosity. The variables r and x are components of a cylindrical coordinate system with the origin on the canal centerline. The axial velocity u is a function of r and t and but is independent of x due to continuity. Note that this equation is linear. The nonlinear terms which are usually present in the Navier–Stokes equations are identical to zero because we assume a one-dimensional flow in the axial direction x.

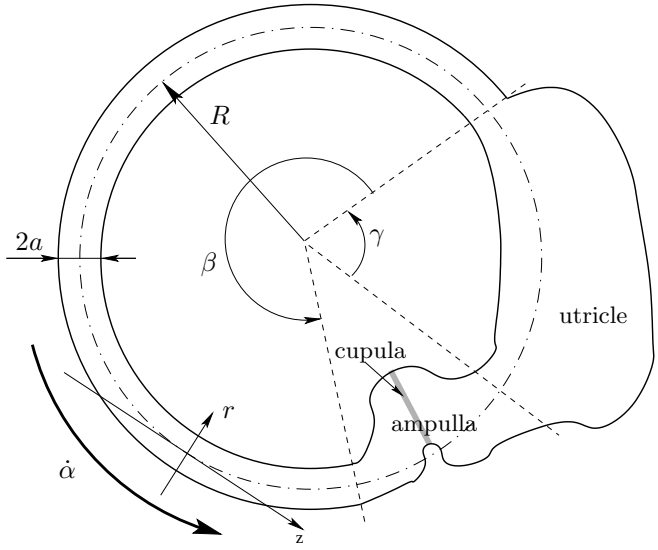

FIGURE 3.1. Schematic of a single semicircular canal with the utricle.

TABLE 3.1. Physical and geometrical parameters

description	symbol	value
major canal radius	R	$3.2 \times 10^{-3}\,\mathrm{m}$
duct radius	a	$1.6 \times 10^{-4}\,\mathrm{m}$
angle subtended by the canal	β	1.4π
angle subtended by the utricle	γ	0.42π
endolymph density	ρ	$10^3\,\mathrm{kg/m^3}$
kinematic viscosity of the endolymph	ν	$10^{-6}\,\mathrm{m^2/s}$
cupular stiffness	K	$13\,\mathrm{GPa/m^3}$

Table 3.1 lists the values for the physical and geometric parameters as they are used in this section. As a matter of fact, these parameters may vary significantly for different individuals. Curthoys & Oman (1987) and, more recently, Bradshaw *et al.* (2010*b*) a good overview on the geometry of SCC including variations by individual.

We differentiate the axial momentum equation once with respect to x to find an expression for the pressure gradient. All terms with w and $\dot{\alpha}$ drop out since

they are constant in x and we obtain

$$\frac{\partial^2 p}{\partial x^2} = 0. \tag{7}$$

Therefore, $\partial p/\partial x$ is a constant and the pressure $p(x)$ is a linear function of x. It can be expressed through the pressure difference Δp between the two ends of the slender part of the semicircular canal,

$$\Delta p = p(\beta R) - p(0) = \beta R \left(\frac{\partial p}{\partial x}\right). \tag{8}$$

This pressure difference is caused by an external force F which exerts a pressure $F/(\pi a^2)$ to one end of the semicircular canal. This leads us to the following expression for the pressure gradient,

$$\frac{\partial p}{\partial x} = \frac{F}{\pi a^2 \beta R}. \tag{9}$$

We model the external force F as the sum of the reactive force F_c of the deflected cupula and the inertial force F_i of the fluid in the utricle. In the present model, we assume the fluid motion within the utricle to be negligibly small with respect to the magnitude of u Van Buskirk (1977). Recent results (Boselli *et al.*, 2010*c*, and Chapter 6) have shown, however, that this assumption is not correct. Nevertheless, we will continue with the original model of VB because the impact of the fluid motion in the utricle on the transduction of angular motion is indeed small.

The reactive force F_c of the cupula is a function of time and is proportional to the volumetric deflection of the cupula,

$$\frac{F_c(t)}{\pi a^2} = KV = K\,2\pi \int_0^t \int_0^a u(\varrho, \tau)\varrho \,\mathrm{d}\varrho \,\mathrm{d}\tau. \tag{10}$$

where K determines the mechanical stiffness of the cupula and the volumetric displacement V is computed as

$$V(t) = \pi \int_0^t \int_0^a u(\varrho, \tau)\varrho \,\mathrm{d}\varrho \,\mathrm{d}\tau. \tag{11}$$

More sophisticated mechanical models for the cupula were studied by Rabbitt & Damiano (1992) and Yamauchi *et al.* (2001).

The inertial force F_i of the fluid in the utricle is approximated by Newton's second law as

$$F_i = m_u R\ddot{\alpha}. \tag{12}$$

Most of the inertial force of the fluid in the utricle is absorbed by the walls at the end of the utricle. Only the fluid volume which directly pushes onto the fluid in the slender part of the canal is relevant to F_i. Therefore, we choose the mass m_u to be equal to the mass of the endolymph which is contained in a torus section of

length γR (arc length of the utricle) with cross-section πa^2 (cross-section of the slender canal),

$$F_i = \rho\pi a^2 \gamma R^2 \ddot{\alpha}. \tag{13}$$

With these expressions, we arrive at the linear inhomogeneous equation for the endolymph flow field in the slender part of the SCC as proposed by VB,

$$\frac{\partial u}{\partial t} + (1+\gamma/\beta)\, R\ddot{\alpha} = -\frac{2\pi K}{\rho\beta R}\int_0^t \int_0^a u\varrho \,\mathrm{d}\varrho \,\mathrm{d}\tau + \frac{\nu}{r}\frac{\partial}{\partial r}\left(r\frac{\partial u}{\partial r}\right). \tag{14}$$

(Note that in contrast to VB we have named the angular acceleration $\ddot{\alpha}$ instead of α.)

We introduce the following dimensionless variables:

$$\tilde{r} = \frac{r}{a}, \quad \tilde{t} = \frac{t}{T_v}, \quad \tilde{u} = \frac{uT_v}{R}, \tag{15}$$

where $T_v = a^2/\nu$ is a time scale which balances the viscous term $\nu\nabla^2 u$ with the unsteady term $\partial u/\partial t$. Note that our definition of the dimensionless variables differs slightly from the choice of VB who introduced an additional time scale Ω^{-1} which characterizes the head maneuver $\dot{\alpha}$.

With (15), we obtain the dimensionless form of (14),

$$\frac{\partial \tilde{u}}{\partial \tilde{t}} + (1+\gamma/\beta)\,\frac{\partial^2 \alpha}{\partial \tilde{t}^2} = -\epsilon\int_0^{\tilde{t}}\int_0^1 \tilde{u}\varrho \,\mathrm{d}\varrho \,\mathrm{d}\tau + \frac{1}{\tilde{r}}\frac{\partial}{\partial \tilde{r}}\left(\tilde{r}\frac{\partial \tilde{u}}{\partial \tilde{r}}\right), \tag{16}$$

where

$$\epsilon = \frac{2\pi a^2 K T_v^2}{\rho\beta R} \ll 1 \tag{17}$$

can be regarded as a dimensionless stiffness parameter. Together with the initial condition $\tilde{u}(r,0) = 0$ and the boundary conditions $\tilde{u}(1,\tilde{t}) = \partial\tilde{u}(0,\tilde{t})/\partial\tilde{r} = 0$ we have arrived at a well-posed problem for $\tilde{u}(\tilde{r},\tilde{t})$ and the cupula deflection $V(t)$.

CHAPTER 4

Solution of Van Buskirk's model

In this chapter[1], we present a solution to Van Buskirk's model that has been introduced in the previous chapter. Van Buskirk *et al.* (1976) make use of $\epsilon \ll 1$ and compute an asymptotic solution of Eq. (16) . In contrast to this approach, we will show in the following that (16) can be solved exactly for an arbitrary head maneuver $\alpha(t)$.

1. Homogeneous solution

At first, we examine (16) without forcing (and for the ease of writing we drop the tilde of the non-dimensionalized variables). To this end, we set $\alpha(t) = 0$ and differentiate (16) once with respect to t to arrive at the equation

$$\frac{\partial^2 u}{\partial t^2} - \frac{1}{r}\frac{\partial}{\partial r}\left(r\frac{\partial^2 u}{\partial r\,\partial t}\right) + \epsilon \int_0^1 u\varrho \,\mathrm{d}\varrho = 0. \tag{18}$$

The ansatz $u(r,t) = \hat{u}(r)e^{-\sigma t}$ reduces the partial integro-differential equation (18) to an ordinary integro-differential equation,

$$\sigma^2 r\hat{u} + \sigma\hat{u}' + \sigma r\hat{u}'' + r\epsilon \int_0^1 \hat{u}\varrho \,\mathrm{d}\varrho = 0, \tag{19}$$

where $\hat{u}' \equiv \mathrm{d}\hat{u}/\mathrm{d}r$. Together with the boundary conditions $\hat{u}(1) = \hat{u}'(0) = 0$ this equation is a nonlinear eigenvalue problem for the eigenvalue σ. The solution of this eigenvalue problem yields modal solutions of the form $\hat{u}_k(r)\exp(-\sigma_k t)$. For eigenvalues $\sigma = \sigma_r + \mathrm{i}\sigma_i$ with a positive real part σ_r the modal solution decays in time. Vice versa we obtain growing solutions for $\sigma_r < 0$. For $\sigma_i \neq 0$ the modal solutions oscillate in time.

[1]This chapter is based on the article 'Fluidmechanics of semicircular canals – revisited', Z. angew. Math. Phys. 59:475-497, 2008 by D. Obrist.

We can recast the nonlinear eigenvalue problem (19) into a linear general eigenvalue problem by defining a new dependent variable $\mathbf{v}(r) = (\hat{u}(r), \sigma\hat{u}(r))^T$,

$$\mathbf{A}\mathbf{v} = \sigma\mathbf{B}\mathbf{v}, \tag{20}$$
$$\mathbf{A} = \begin{pmatrix} -\epsilon\, r \int_0^1 (\cdot)\varrho \,\mathrm{d}\varrho & 0 \\ 0 & r \end{pmatrix},$$
$$\mathbf{B} = \begin{pmatrix} r\,\partial^2/\partial r^2 + \partial/\partial r & r \\ r & 0 \end{pmatrix}.$$

The method of expanding the dependent variable is often used in hydrodynamic stability, where the eigenvalue in a spatial stability investigation can appear up to its fourth power (e.g. Schmid & Henningson, 2000)). In the case of hydrodynamics the expanded variables $\alpha^n\hat{u}$ have no particular physical meaning. In our case, $-\sigma\hat{u}(r)$ corresponds to the acceleration $\partial u/\partial t$. Therefore (20) is nothing more than a reformulation of (18) in phase space $(u, \partial u/\partial t)$ which reduces (18) from a second order to a first order equation in t.

In the form (20) the matrices $\mathbf{A}$ and $\mathbf{B}$ are matrices of differential and integral operators, and the vector $\mathbf{v}$ is a vector of continuous functions. By applying an appropriate spatial discretization scheme we can approximate $\mathbf{A}$ and $\mathbf{B}$ by matrices with scalar entries and $\mathbf{v}$ becomes a vector of function values at discrete grid points r_j. In our case, we use a compact finite difference scheme of fourth order and equidistant grid spacing to discretize (20). The discretized eigenvalue problem can be solved numerically with a standard eigenvalue solver. Already less than one hundred grid points give enough accuracy to resolve the first few eigenmodes. Figure 4.1 shows the numerically computed eigenvalue spectrum for $\epsilon = 0.017$ which is the value used by Van Buskirk *et al.* (hereafter VB). For reasons that will become clear in the following, we name the first and least damped mode the *cupula mode* and the remaining modes the *duct modes*.

We have listed the five least stable eigenvalues for different ϵ in table 4.1. All eigenvalues are real and positive and therefore the physical system described by (18) is asymptotically stable and does not have any oscillating eigenmodes. This observation corresponds well to the findings for Steinhausen's model (Chapter 1).

Although convenient in use, the numerical solution of (20) does not provide us with any profound insight into the true structure of the eigenvalue spectrum. It merely gives us numerical values for $\{\sigma_k, \hat{u}_k(r)\}$. Therefore we put the numerical solution aside and proceed to solve (19) analytically.

At this point we make the important observation that the integral in (19) is proportional to the volume flow through the duct. This definite integral yields a value which is independent of r, i.e. , a constant. With the definition of the

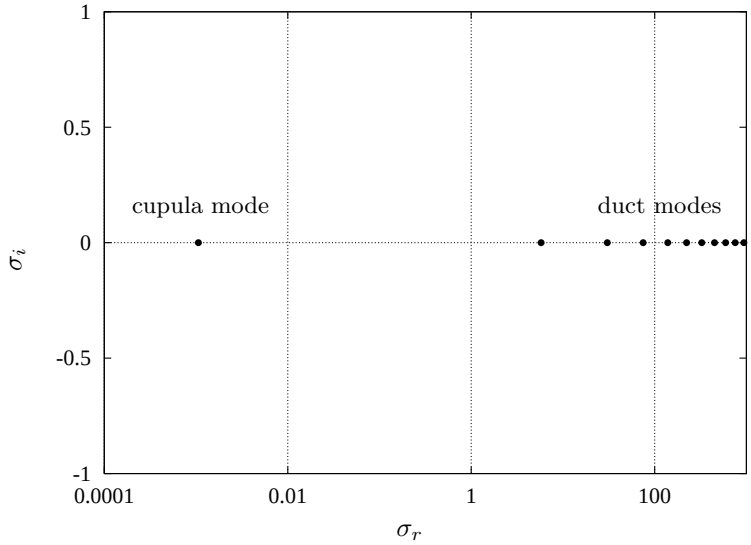

FIGURE 4.1. Eigenvalues $\sigma = \sigma_r + \mathrm{i}\sigma_i$ for $\epsilon = 0.017$. (Note the logarithmic scale of the abscissa.)

TABLE 4.1. Eigenvalues σ_k and volume flow κ_k of the five least stable modes

	$\epsilon = 0.01$	$\epsilon = 0.017$	$\epsilon = 0.05$	$\epsilon = 0.09752$	$\epsilon = 0.2$
σ_0	6.251×10^{-4}	1.063×10^{-3}	3.127×10^{-3}	6.102×10^{-3}	1.253×10^{-2}
σ_1	5.783	5.782	5.780	5.777	5.771
σ_2	3.047×10^{1}	3.047×10^{1}	3.047×10^{1}	3.047×10^{1}	3.047×10^{1}
σ_3	7.488×10^{1}	7.488×10^{1}	7.488×10^{1}	7.488×10^{1}	7.488×10^{1}
σ_4	1.390×10^{2}	1.390×10^{2}	1.390×10^{2}	1.390×10^{2}	1.390×10^{2}
$\lvert\kappa_0\rvert$	0.2500	0.2501	0.2501	0.2503	0.2505
$\lvert\kappa_1\rvert$	0.2446	0.2446	0.2447	0.2448	0.2451
$\lvert\kappa_2\rvert$	0.04643	0.04643	0.04643	0.04642	0.04642
$\lvert\kappa_3\rvert$	0.01890	0.01890	0.01890	0.01890	0.01890
$\lvert\kappa_4\rvert$	0.01019	0.01019	0.01019	0.01019	0.01019

dimensionless volume flow rate κ,

$$\kappa \equiv \int_0^1 \hat{u}(\varrho)\, \varrho \, \mathrm{d}\varrho, \tag{21}$$

we can rewrite (19) as an inhomogeneous ordinary differential equation for $\hat{u}$,

$$\sigma r\hat{u}'' + \sigma\hat{u}' + \sigma^2 r\hat{u} = -r\epsilon\kappa. \tag{22}$$

The particular solution of (22) is $\hat{u}_i = -\epsilon\kappa/\sigma^2$. The homogeneous part of (22) is a Bessel equation of order zero with the solutions $J_0(\sqrt{\sigma}r)$ and $Y_0(\sqrt{\sigma}r)$ (Abramowitz & Stegun, 1965). We can discard the solution $Y_0(\sqrt{\sigma}r)$ because it is singular at $r = 0$ and does not satisfy the boundary condition there. Thus, we get

$$\hat{u}(r) = AJ_0(\sqrt{\sigma}\, r) - \epsilon\frac{\kappa}{\sigma^2}, \tag{23}$$

where A is an arbitrary constant. We can now substitute $\hat{u}$ in (21) by (23) which gives us following expression for κ

$$\kappa = A\zeta_\sigma \frac{\sigma^2}{\sigma^2 + \epsilon/2}, \tag{24}$$

with

$$\zeta_\sigma \equiv \int_0^1 J_0(\sqrt{\sigma}\varrho)\, \varrho\, \mathrm{d}\varrho. \tag{25}$$

It remains to satisfy the boundary condition $\hat{u}(1) = 0$. From (23) and (24) we get the relation

$$J_0(\sqrt{\sigma}) = \frac{\epsilon\zeta_\sigma}{\sigma^2 + \epsilon/2} \tag{26}$$

which can be understood as a dispersion relation for the semicircular canal. Its solutions determine all eigenvalues σ.

Although there is no explicit solution to (26) we can find the locus of all eigenvalues by simple graphical examination. To this end, we plot the function values of the left-hand side and of the right-hand side of (26) against $\sqrt{\sigma}$ (figures 4.2 & 4.3). The eigenvalues σ_k correspond to the intersections of the two curves (marked by circles). As expected from the numerical solution all eigenvalues are positive.

The dashed curve in figure 4.2, i.e. the right-hand side of (26), drops rapidly to zero, such that it intersects with the solid line in the vicinity of the first root of the Bessel function. For larger choices of ϵ the dashed curve drops more slowly. Theoretically, we can choose ϵ so large that the dashed and the solid curve do not intersect until around the second root of the Bessel function (or even later). In that case, we would loose our first few real eigenvalues and we would obtain instead a pair of complex conjugate eigenvalues (indicating that the system is now underdamped). However, the situation remains qualitatively as shown in figure 4.2 for all physiologically sensible choices of ϵ.

We observe that the least damped eigenvalue σ_0 is very close to 0. Numerical investigation shows that σ_0 is approximately proportional to ϵ (figure 4.4). If we

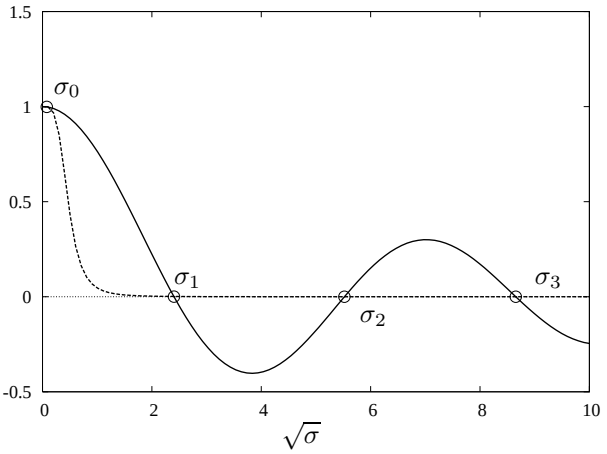

FIGURE 4.2. Graphical solution of the dispersion relation (26) for $\epsilon = 0.09752$: intersections of the left-hand side (——) with the right-hand side (– – –) of (26) correspond to eigenvalues.

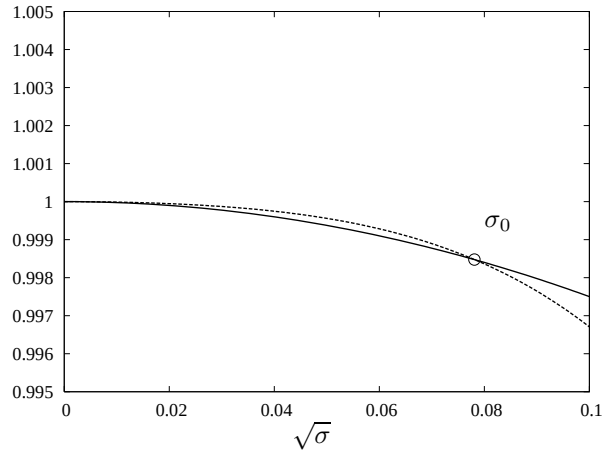

FIGURE 4.3. Close-up of the graphical solution of the dispersion relation (26); cf. figure 4.2.

use the approximation $J_0(s) = 1 - s^2/4 + s^4/64 + O(s^6)$ for small s (and $\sigma^2 \ll \epsilon$) we can show that this eigenvalue is approximately given by

$$\sigma_0 \approx \epsilon/16. \tag{27}$$

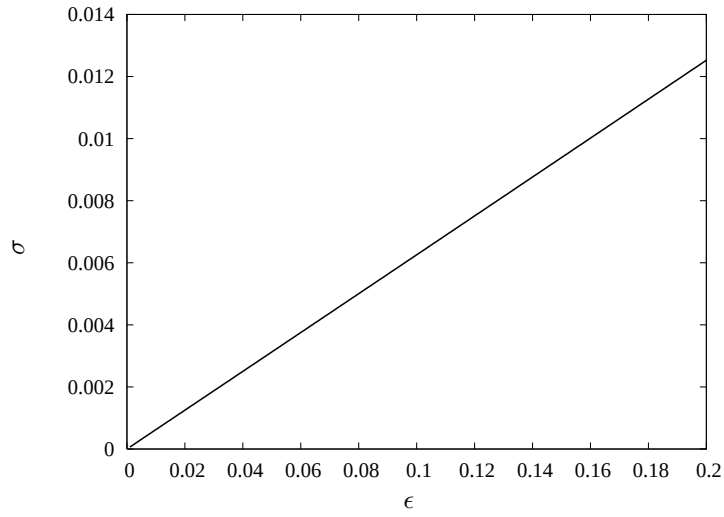

FIGURE 4.4. Numerically computed least damped eigenvalue σ_0 as a function of ϵ.

The result (27) is consistent with the result of VB who arrived at $\sigma_0 = \epsilon/16$ through asymptotics for $\epsilon \ll 1$. All other eigenvalues $\sigma_1, \sigma_2, \ldots$ (there are infinitely many) correspond approximately to the roots of $J_0(\sqrt{\sigma})$ since the right-hand side of (26) is almost zero for $\sigma > 1$,

$$\sigma_j \approx \lambda_j^2, \quad j = 1, 2, \ldots, \tag{28}$$

where λ_j is the j-th root of the Bessel function J_0.

From the approximate expressions (27) and (28) we see that there is a fundamental difference between the least damped eigenvalue σ_0 and all other eigenvalues. To illustrate this difference, we briefly re-consider our problem for a semicircular canal without a cupula. We can eliminate the cupula from our equations by setting $\epsilon = 0$. In that case, the right-hand side of (26) is zero. Obviously, the least stable eigenvalue σ_0 is no longer a solution. The other eigenvalues, however, remain approximately at the same locations. Apparently, these modes do not depend on the presence of the cupula. They are directly related to the modes of a normal pipe flow. Therefore, we call them *duct modes*. The least stable mode exists only because of the cupula and its eigenvalue, i.e. its damping, is approximately proportional to the cupula stiffness. Therefore, we call it the *cupula mode* and we denote its eigenvalue also by

$$\sigma_c \equiv \sigma_0. \tag{29}$$

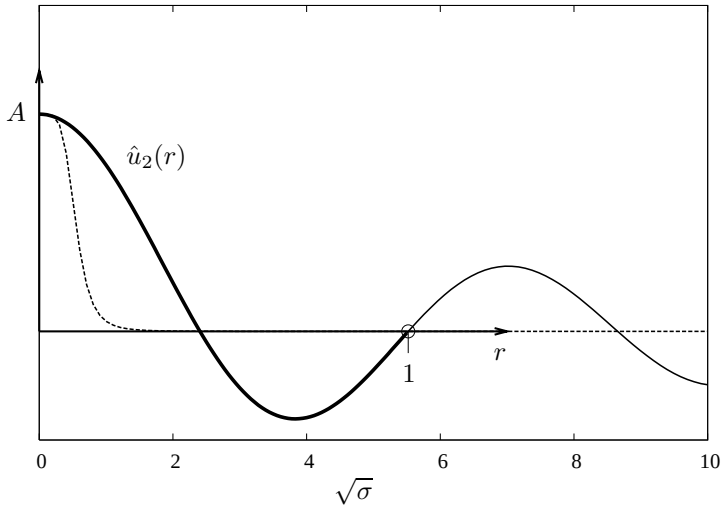

FIGURE 4.5. Construction of eigenfunctions from the graphical solution of (26) on the example of the eigenfunction $\hat{u}_2(r)$ which is plotted as a thick solid line. (note that this plot uses two different sets of axes: one with $\sqrt{\sigma}$ on the abscissa for plotting (26) and one with the abscissa r for the eigenfunction $\hat{u}_2(r)$)

To conclude our discussion of the eigenvalue spectrum, we note that although $\sigma = 0$ satisfies (26) it is not an eigenvalue, since its corresponding eigenfunction is the trivial solution $\hat{u} = 0$.

In addition to the eigenvalues σ, we can also extract the shape of the eigenfunctions $\hat{u}(r)$ directly from figure 4.2. According to (23) the eigenfunctions $\hat{u}(r)$ have the form of Bessel functions of order zero which are shifted by a constant such that $\hat{u}(r = 1) = 0$. Therefore, we can find the shape of the j-th eigenfunction by placing the abscissa r such that $r = 1$ cuts the Bessel function at $J_0(\sqrt{\sigma_j})$. Figure 4.5 demonstrates this graphical construction of the eigenfunctions on the example of $\hat{u}_2$ which is the eigenfunction associated with σ_2. The higher eigenfunctions consist of increasingly larger sections of the Bessel function.

Because the Bessel function J_0 behaves like a parabola in the vicinity of zero, the eigenfunction $\hat{u}_0$ of the least damped mode has a nearly parabolic shape. This is illustrated in figure 4.6 which shows that also the first duct mode $\hat{u}_1$ has a velocity profile which is close to a parabola.

The reason for the (nearly) parabolic velocity profiles of the two least damped modes becomes clearer when we relate our modal ansatz $u(r,t) = \hat{u}(r)e^{-\sigma t}$ to a well known result for pulsating pipe flow. Womersley (1955) introduced the

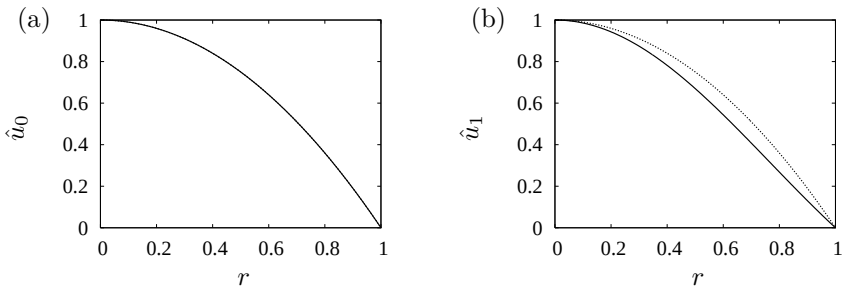

FIGURE 4.6. The two least stable eigenfunctions $\hat{u}_0(r)$ and $\hat{u}_1(r)$. For comparison, the dotted line shows the parabolic profile $1-r^2$.

dimensionless frequency parameter

$$Wo = a\sqrt{\frac{\omega}{\nu}} \tag{30}$$

where ω is the angular frequency of the pulsation. This number is nowadays commonly known as the *Womersley number*. We can recover the Womersley number in our ansatz if we replace the frequency ω in (30) by $1/T$ where T describes the e-folding time of a decaying eigenmode. We find that

$$\sqrt{\sigma} = a\sqrt{\frac{1}{T\nu}} = Wo_T \tag{31}$$

where Wo_T indicates that the Womersley number is built with the inverse time scale $1/T$ instead of the frequency ω. Therefore, the square root of the eigenvalue σ can be interpreted as a (modified) Womersley number. This also explains why the eigenfunction of the cupula mode (with $\sqrt{\sigma_c} \ll 1$) has a parabolic shape.

We should note that the duct modes have also been found by Rabbitt & Damiano (1992). However, they were missing the cupula mode which they introduced only later by asymptotic matching of the flow field in the ampulla Damiano & Rabbitt (1996). Furthermore, we find that the two asymptotic solutions of VB correspond to the cupular mode and the first duct mode, respectively. Whereas VB have arrived at this result through multiple-scale analysis in t and ϵt, we have reproduced their results *and* revealed the complete modal structure by straightforward analytical reasoning. The eigenvalues of the cupula mode and the least damped duct mode correspond directly to the two time scales (4) extracted from Steinhausen's model: the dimensional damping rate of the cupula mode scales like $\epsilon/(a^2/\nu)$ which is therefore a physically meaningful expression for the ratio k/r in Steinhausen's model; the least damped eigenvalue of the duct modes scales with the viscous time scale a^2/ν which relates to the ratio r/m.

This concludes our discussion of the homogeneous problem (18). We have found the complete spectrum with its corresponding eigenfunctions. In its general form the solution to (18) is

$$u(r,t) = \sum_{k=0}^{\infty} A_k \hat{u}_k(r) e^{-\sigma_k t}, \tag{32}$$

where the coefficients A_k are determined through the initial conditions. One might argue that the higher modes are physically irrelevant since they are so heavily damped that they cannot be observed in nature. However, we will show in the following section that the knowledge of the complete set of modal solutions is a useful asset for the computation of the inhomogeneous solution of (16).

2. Impulse response

In this section we find the solution of Eq. (16) for an impulsive acceleration $\ddot{\alpha}(t) = B\delta(t)$ of the semicircular canal. This corresponds to a sudden acceleration of the head at rest to a constant velocity $\dot{\alpha} = Ba^2/\nu$ (the factor a^2/ν arises because the dots in $\dot{\alpha}$ and $\ddot{\alpha}$ stand for the derivative with respect to the *dimensional* time variable, cf. Eq. (15)).

We solve this inhomogeneous problem by recasting it into a homogeneous initial value problem. To this end, we integrate (16) with respect to t from $-T$ to $+T$ and let $T \to 0$. The left-hand side gives us values for u immediately before and after $t = 0$ as well as a constant term from the integration of $\delta(t)$. The right-hand side vanishes due to the boundedness of u, $(1/r)\partial u/\partial r$ and $\partial^2 u/\partial r^2$ (these values are bounded since there cannot be infinite velocities or infinite viscous forces),

$$u(r, t = 0^+) - u(r, t = 0^-) + (1 + \gamma/\beta)\, B = 0. \tag{33}$$

Causality tells us that $u(r, t = 0^-)$ must be zero such that we obtain the initial condition

$$u(r, t = 0^+) = u_0 = -(1 + \gamma/\beta)\, B. \tag{34}$$

Since (16) is a second order equation in t we need a second initial condition. We obtain this second condition by differentiating (16) once with respect to t. Then we integrate this equation as before from $-T$ to T with $T \to 0$. In this case the forcing term on the left-hand side is zero due to the symmetry of $\delta(t)$. We obtain

$$\begin{aligned}\left.\frac{\partial u}{\partial t}\right|_{t=0^+} - \left.\frac{\partial u}{\partial t}\right|_{t=0^-} &= -\epsilon \lim_{T\to 0} \int_{-T}^{T}\int_{0}^{1} u\varrho \,\mathrm{d}\varrho \,\mathrm{d}s \\ &\quad + \frac{1}{r}\frac{\partial}{\partial r}\left(r\frac{\partial}{\partial r}u(r, t = 0^+)\right) - \frac{1}{r}\frac{\partial}{\partial r}\left(r\frac{\partial}{\partial r}u(r, t = 0^-)\right).\end{aligned}$$

The integral on the right-hand side goes to zero due to the boundedness of u. For the remaining two terms on the right-hand side we use the causality argument

and (34). This gives us the second initial condition

$$\left.\frac{\partial u}{\partial t}\right|_{t=0^+} = 0. \tag{35}$$

With this we have shown that the homogeneous problem (18) together with the initial conditions (34) and (35) is equivalent to the inhomogeneous problem (16) with impulsive forcing $\ddot{\alpha} = B\delta(t)$ (Kevorkian, 1990). Or in other words, the impulsive forcing at $t = 0$ leads to a non-zero state at $t = 0^+$ which is given by (34) and (35). This allows us to use the general solution (32) for the homogeneous problem that we have derived in the previous section. The unknown coefficients A_k are now determined through the initial conditions,

$$u(r, t = 0) = u_0 = \sum_{k=0}^{\infty} A_k \hat{u}_k(r), \tag{36}$$

$$\frac{\partial}{\partial t} u(r, t = 0) = 0 = \sum_{k=0}^{\infty} A_k \sigma_k \hat{u}_k(r). \tag{37}$$

In order to get explicit expressions for A_k, we need an orthogonality relation for the eigenfunctions $\hat{u}_k$. We obtain such an orthogonality relation by the theory of adjoint operators (see, for example, § 3.3.1 in Schmid & Henningson (2000) for a brief introduction to adjoint problems). The adjoint problem to (20) is defined as

$$\mathbf{A}^+ \mathbf{v}^+ = \eta \mathbf{B}^+ \mathbf{v}^+.$$

The vector $\mathbf{v}^+$ is called the adjoint eigenvector and η is the adjoint eigenvalue. The adjoint operators $\mathbf{A}^+$ and $\mathbf{B}^+$ are defined as

$$\begin{aligned} (\mathbf{p}, \mathbf{A}\mathbf{q}) &= (\mathbf{A}^+ \mathbf{p}, \mathbf{q}), \\ (\mathbf{p}, \mathbf{B}\mathbf{q}) &= (\mathbf{B}^+ \mathbf{p}, \mathbf{q}), \end{aligned}$$

where $\mathbf{p}$ and $\mathbf{q}$ are arbitrary vectors and $(\cdot, \cdot)$ is the inner product which we define as

$$(\mathbf{p}, \mathbf{q}) \equiv \int_0^1 \mathbf{p}^* \mathbf{q} \, \mathrm{d}r. \tag{38}$$

Trough integration by parts we find that

$$\begin{aligned} \mathbf{A}^+ &= \begin{pmatrix} -\epsilon \, r \int_0^1 (\cdot) \, r \mathrm{d}r & 0 \\ 0 & r \end{pmatrix} = \mathbf{A}, \\ \mathbf{B}^+ &= \begin{pmatrix} r \, \partial^2/\partial r^2 + \partial/\partial r & r \\ r & 0 \end{pmatrix} = \mathbf{B}. \end{aligned}$$

Therefore (20) is formally self-adjoint and $\{\eta, \mathbf{v}^+\} = \{\sigma, \mathbf{v}\}$.

From the theory of adjoint eigenvalue problems we know that $(\sigma-\eta^*)(\mathbf{v}^+, \mathbf{B}\mathbf{v}) = 0$. For self-adjoint operators, this orthogonality relation reduces to

$$(\mathbf{v}_k, \mathbf{B}\mathbf{v}_l) = \pm\delta_{kl}, \tag{39}$$

where we assume appropriate scaling of $\mathbf{v}$.

Note that $(\mathbf{v}_k, \mathbf{B}\mathbf{v}_k)$ may be negative for certain eigenfunctions $\mathbf{v}_k$. Thus, $\mathbf{B}$ is indefinite. It is worthwhile to take a closer look at this peculiar situation. To this end, we write the left-hand side of (39) in a more explicit form,

$$\begin{aligned}(\mathbf{v}_k, \mathbf{B}\mathbf{v}_k) &= \int_0^1 (\hat{u}_k, \sigma_k\hat{u}_k) \begin{pmatrix}(r\,\partial^2/\partial r^2 + \partial/\partial r + \sigma_k r)\hat{u}_k \\ r\hat{u}_k\end{pmatrix} \mathrm{d}r \\ &= -\frac{\epsilon\kappa_k}{\sigma_k}\int_0^1 \hat{u}_k\, r\mathrm{d}r + \sigma_k\int_0^1 \hat{u}_k r\,\mathrm{d}r \\ &= -\frac{\epsilon\kappa_k^2}{\sigma_k} + \sigma_k\int_0^1 \hat{u}_k^2 r\,\mathrm{d}r, \end{aligned} \tag{40}$$

where we have used the definition of κ (21) and the original eigenvalue problem (22). We see that this expression may become negative (independent of the scaling of $\hat{u}_k$) if $|\sigma_k|^2 \ll \epsilon$. In the previous section we have seen that this is indeed the case for the first mode. For all other modes $(\mathbf{v}_k, \mathbf{B}\mathbf{v}_k)$ is positive. So, we can write our orthogonality relation in the more precise form,

$$(\mathbf{v}_k, \mathbf{B}\mathbf{v}_l) = \begin{cases} -\delta_{kl} & k,l = 0, \\ \delta_{kl} & k,l \neq 0. \end{cases} \tag{41}$$

With this result at hand we can return to (36) and (37). We apply $(\mathbf{v}_l, \mathbf{B}\,\cdot)$ to both sides of these equations and obtain the following simple expression for A_n

$$A_l = \pm\left((\hat{u}_l^*, \sigma_l^*\hat{u}_l^*)^T, \mathbf{B}(u_0, 0)^T\right), \tag{42a}$$

$$A_l = \pm\int_0^1 u_0\sigma_l\hat{u}_l r\,\mathrm{d}r, \tag{42b}$$

$$A_l = \pm u_0\sigma_l\kappa_l. \tag{42c}$$

Therefore, the response $u(r,t)$ to the impulsive forcing $\partial^2\alpha/\partial t^2 = B\delta(t)$ is

$$u(r, t\geq 0) = B\,(1+\gamma/\beta)\left[\sigma_0\kappa_0\hat{u}_0(r)e^{-\sigma_0 t} - \sum_{k=1}^{\infty}\sigma_k\kappa_k\hat{u}_k(r)e^{-\sigma_k t}\right]. \tag{43}$$

For the clinical application it is more interesting to look at the volume displacement $V(t)$ of the cupula, Eq. (11), which is indicative of the perception of angular motion,

$$V(t\geq 0) = B\,2\pi(1+\gamma/\beta)\left[\kappa_0\left(1-e^{-\sigma_0 t}\right) - \sum_{k=1}^{\infty}\kappa_k^2\left(1-e^{-\sigma_k t}\right)\right]. \tag{44}$$

Note that we do not need any explicit knowledge of the shape of the eigenfunctions to compute $V(t)$. It is sufficient to know the eigenvalues σ_k and the absolute values of the dimensionless flow rates κ_k. In practice it is sufficient to use the first five modes due to the fast convergence of the infinite sum in (44). In table 4.1 we have listed σ_k and $|\kappa_k|$ of the five least stable modes for different values of ϵ.

Before we conclude this section let us make an interesting observation which will be of good use in the following section. From a physical point of view it is clear that $V(t) \to 0$ as $t \to \infty$ (i.e. the cupula must return to its relaxed state in the absence of external forcing). At the same time, equation (44) tells us that

$$V(t \to \infty) = B\, 2\pi(1 + \gamma/\beta) \left[\kappa_0^2 - \sum_{k=1}^{\infty} \kappa_k^2 \right]. \tag{45}$$

Therefore, the following relation between the factors κ_k must hold

$$\kappa_0^2 = \sum_{k=1}^{\infty} \kappa_k^2. \tag{46}$$

3. Arbitrary forcing

In this section, we find the solution to (16) for arbitrary forcing $\ddot{\alpha}(t)$. The theory of Green's functions (Bender & Orszag, 1978) provides us with a simple and efficient way to find this solution. Green's function $G(t, \tau)$ is the response of the dynamic system to an impulsive forcing $\ddot{\alpha}(t) = \delta(t - \tau)$. The volume displacement for arbitrary forcing can then be computed with the integral

$$V(t) = \int_{-\infty}^{\infty} \ddot{\alpha}(\tau) G(t, \tau) \mathrm{d}\tau. \tag{47}$$

We can easily find $G(t, \tau)$ by using our result for impulsive forcing (44) with $B = 1$ and t replaced by $t - \tau$,

$$G(t, \tau) = \begin{cases} 2\pi(1 + \gamma/\beta) \sum_{k=0}^{\infty} \mp\kappa_k^2 \left(1 - e^{-\sigma_k (t-\tau)}\right) & t \geq \tau, \\ 0 & t < \tau, \end{cases} \tag{48}$$

where we use the plus sign for $k = 0$ and the minus sign for all other modes. Therefore, the volume displacement $V(t)$ is given by the integral expression

$$V(t) = 2\pi(1 + \gamma/\beta) \sum_{k=0}^{\infty} \mp\kappa_k^2 \left[\int_{-\infty}^{t} \frac{\partial^2}{\partial t^2} \alpha(\tau) \left(1 - e^{-\sigma_k (t-\tau)}\right) \mathrm{d}\tau \right]. \tag{49}$$

With this result we have already completed the main task of this section. However, we can still greatly simplify the integral in (49).

We use integration by parts to find

$$\int_{-\infty}^{t} \frac{\partial^2}{\partial t^2} \alpha(\tau) \left(1 - e^{-\sigma_k (t-\tau)}\right) \mathrm{d}\tau = \sigma_k \int_{0}^{\infty} \frac{\partial}{\partial t} \alpha(t - \tau) e^{-\sigma_k \tau} \mathrm{d}\tau, \tag{50}$$

where we assume that $\partial\alpha/\partial t \to 0$ for $t \to -\infty$. In order to make further progress we need to make use of the particular structure of the eigenvalue spectrum. In § 1 we have found that all eigenvalues except σ_0 have a large positive value[2]. This allows us to replace the integral for $k \geq 1$ by its asymptotic expansion (Bender & Orszag, 1978)

$$\sigma_k \int_0^\infty \frac{\partial}{\partial t}\alpha(t-\tau)e^{-\sigma_k\tau}\mathrm{d}\tau \simeq \frac{\partial}{\partial t}\alpha(t). \tag{51}$$

We get our final expression for the volume displacement by Introducing this result into (49) and by using relation (46),

$$V(t) \approx -2\pi(1+\gamma/\beta)\kappa_0^2\left[\frac{\partial\alpha}{\partial t} - \sigma_0\int_0^\infty \frac{\partial}{\partial t}\alpha(t-\tau)e^{-\sigma_0\tau}\mathrm{d}\tau\right]. \tag{52}$$

This is a remarkable result. First, it allows us to compute easily the volume displacement $V(t)$ requiring only knowledge of σ_0 and $|\kappa_0|$. Second, and more importantly, it reveals in mathematical terms how the fluid dynamics of the semicircular canal translates the angular velocity $\partial\alpha/\partial t$ directly to a volume displacement $V(t)$ of the cupula.

Apart from the second term on the right-hand side of (52) the cupula displacement V is proportional to the angular velocity $\dot{\alpha}$. We can interpret the second term as the difference between the perceived and the actual angular velocity $\dot{\alpha}$. We define this difference as the velocity error $\dot{\alpha}_e$,

$$\dot{\alpha}_e = -\sigma_0\int_0^\infty \dot{\alpha}(t-\tau)e^{-T_v\sigma_0\tau}\mathrm{d}\tau \tag{53}$$

where we have returned to dimensional variables (note the factor T_v in the exponent). With this definition, the perceived velocity is $\dot{\alpha}+\dot{\alpha}_e$. For a velocity profile $\dot{\alpha}(t)$ which changes rapidly with respect to the cupula time scale $T_c = a^2/(\nu\sigma_0)$ (as it is the case for most natural movements of the head) the relative velocity error $\dot{\alpha}_e/\dot{\alpha}$ is only of order σ_0, i.e. of order ϵ. For a velocity $\dot{\alpha}(t)$ that changes very slowly or remains constant (like when spinning continuously on an office chair) the error term $\dot{\alpha}_e$ grows steadily until it nearly cancels $\dot{\alpha}$. In that sense, the velocity error can be understood as a mechanical adaptation of the SCC.

It has been postulated many times in literature that semicircular canals are transducers of angular motion. Equation (52) is mathematical evidence for this postulate and relates it directly and explicitly to fluid mechanics. This result has been derived from the fundamental law of conservation of momentum (6) and not from a macroscopic model that already implies the above postulate.

[2]In this context large means that these modes are heavily damped. In physical time scales the mode $\sigma_1 \approx 5.78$, for instance, has decayed to about 1% of its initial value after only 0.02 s.

We conclude this section by giving an approximate value for the proportionality factor (or gain) between $\dot{\alpha}$ and the dimensional volume displacement $V^\star$,

$$V^\star(t) \approx -1.07 \times 10^{-12} \cdot \left[\dot{\alpha}(t) - \sigma_0 \int_0^\infty \dot{\alpha}(t-\tau) e^{-\sigma_0 a^2 \tau/\nu} \mathrm{d}\tau \right] \quad [\mathrm{m}^3], \qquad (54)$$

where the time has to be understood as a dimensional value. This formula is accurate up to a factor $1 + O(\epsilon)$.

CHAPTER 5

Reaction of semicircular canals to typical head maneuvers

In this chapter, we apply our results for the dynamics within semicircular canals to maneuvers of the head as they may occur in daily life and as they are performed in clinical experiments.

Obrist (2008) showed that the cupula displacement is given by

$$V(t) \approx -A_c R T_v \frac{1+\gamma/\beta}{8} \left[\dot{\alpha}(t) - \sigma_c \int_0^\infty \dot{\alpha}(t - \tau T_v) e^{-\sigma_c \tau} \, \mathrm{d}\tau \right], \qquad (55)$$

where the factor in front of the square bracket amounts to approximately $1.07 \times 10^{-12}\,\mathrm{m^3 s}$ (using the values from table 3.1). This equation is approximate in the sense that it yields accurate results for head maneuvers with angular velocities that change slowly with respect to the viscous time scale $T_v = a^2/\nu$. For most natural head maneuvers (55) is sufficiently accurate.

Equation (55) is analytical evidence that SCC are indeed good sensors for angular motion, since it shows that $V \propto \dot{\alpha}$ apart from the *velocity error*

$$\dot{\alpha}_e \equiv -\sigma_c \int_0^\infty \dot{\alpha}(t - \tau T_v) e^{-\sigma_c \tau} \mathrm{d}\tau. \qquad (56)$$

If the velocity error is strong enough it may lead to a sensation of reverse angular motion after the actual angular motion has ended. In any case, the velocity error leads to an overshoot in the cupula displacement at the end of a head maneuver. Figure 5.1 demonstrates this effect by numerical integration of (16) for a smooth head rotation from an upright (0°) to a supine position (120°) in 3 s. Such a head maneuver is part of a diagnostic sequence known as the Dix–Hallpike maneuver (Dix & Hallpike, 1952). It is often used in clinical and numerical experiments (e.g. in figure 7.3 and Rajguru *et al.*, 2004) and we will use it throughout this work. The angle of rotation α for this head maneuver is given by

$$\alpha(t) = \begin{cases} 0, & t < -3\mathrm{s} \\ \frac{2\pi}{3 \cdot 2187} \left(2187 - 20t^7 - 210t^6 - 756t^5 - 945t^4\right), & -3\mathrm{s} < t < 0\mathrm{s} \\ \frac{2\pi}{3}, & 0\mathrm{s} < t \end{cases} \qquad (57)$$

The time axis is adjusted such that $t = 0\,\mathrm{s}$ coincides with the end of the maneuver. The particular choice for Eq. (57) ensures that the slopes of the angle α, the velocity $\dot{\alpha}$ and the acceleration $\ddot{\alpha}$ are continuous at $t = -3\,\mathrm{s}$ and $0\,\mathrm{s}$ (cf. figure 5.1b).

Figure 5.1 shows that the cupula displacement $V(t)$ is nearly proportional to the angular head velocity $\dot{\alpha}(t)$ during the maneuver. At $t = 0\,\mathrm{s}$ when the maneuver has finished the cupula has overshot its relaxed position and returns only slowly (with time constant $T_v/\sigma_c \approx 4.2\,\mathrm{s}$) to its relaxed position. This *post-rotatory overshoot* (including its effect on the firing rate) can also been seen in figure 3 of Rabbitt *et al.* (2009).

1. Constant velocity

It is well known that the sensation of angular motion decreases over time even if the angular velocity is kept constant. This phenomenon is governed by different mechanisms. On the one hand, we have several adaptation and storage mechanisms in the nerve system and, on the other hand, there is an adaptation in the mechanical system. This mechanical adaptation leads to the velocity error $\dot{\alpha}_e$ of (52).

Clinical tests show that the overall adaptation process has a time constant[1] of approximately 21 s (Malcom, 1968). We must not use this value, however, since it includes the so-called *velocity storage* mechanism of the nerve system which is not part of our model (e.g. Robinson, 1977; Cohen *et al.*, 1977; Raphan *et al.*, 1979). Rather, we must look at the time constant of the mechanical system alone which corresponds to the relaxation time of the cupula. Here, we use the value $T_c = 4.2\,\mathrm{s}$ reported by Dai *et al.* (1999).

From (52) and (27) we can derive that the appropriate time constant is attained for

$$\epsilon \approx 16\sigma_c = \frac{16a^2}{\nu T_c} = 0.09752. \tag{58}$$

From this value for ϵ we can compute a value for the cupular stiffness $K \approx 13\,\mathrm{GPa/m^3}$. Note that this value is much larger than the value given by Van Buskirk *et al.* (1976) because of the larger time constant T_c used by these authors.

2. Sensation threshold

There exists a threshold value for the angular velocity $\dot{\alpha}_t$ (Groen & Jongkees, 1948). Below this threshold value angular motion cannot be sensed with the vestibular organ. Oman *et al.* (1987) report the threshold value $\dot{\alpha}_t = 2^\circ/\mathrm{s}$.

From (52) we know that the volume displacement of the cupula is linearly dependent on the amplitude of $\dot{\alpha}$. If we neglect the velocity error $\dot{\alpha}_e$, we find

[1] The time constant is defined as the time after which the amplitude has decayed to $1/e$ of its initial value.

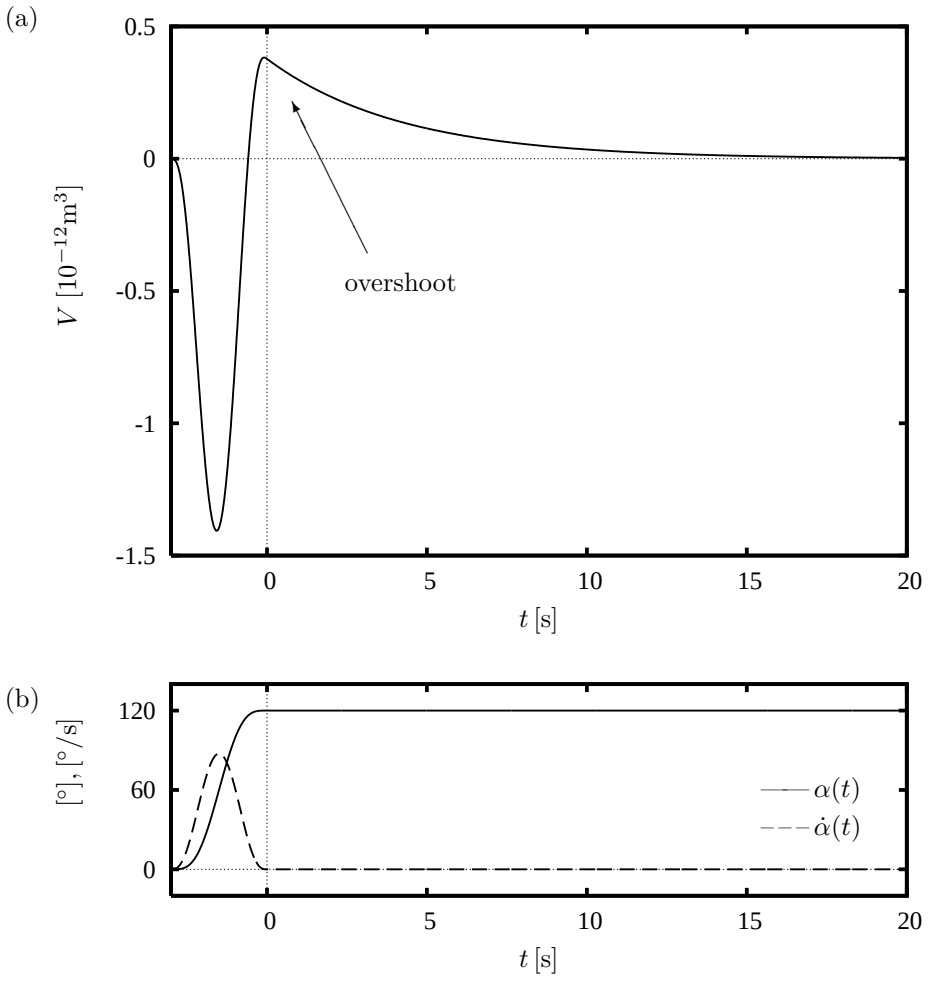

FIGURE 5.1. (a) Cupular displacement $V(t)$ in a healthy SCC during and after (b) a head maneuver from $\alpha = 0°$ to $120°$ ($\epsilon = 0.09752$, $\sigma_c \approx 0.00610$)

from (54) that the threshold value for the volume displacement V_t is approximately

$$|V_t| \approx 3.74 \times 10^{-14}\mathrm{m}^3. \tag{59}$$

The value V_t is important for the investigation of *canalithiasis* (which can cause *benign paroxysmal positional vertigo* or BPPV, Chapter 7). In *canalithiasis* the endolymph flow is disturbed by small particles falling through the duct. This disturbed flow may lead to a secondary and pathological deflection of the cupula which causes vertigo. A symptomatic feature of canalithiasis is the latency between the head maneuver and the onset of vertigo. This latency period (typically a few seconds) may be interpreted as the time during which the cupular displacement $|V(t)|$ is smaller than the threshold value V_t. Apart from the threshold value, we will show in Chapter 8 that also the cupular mode plays an important role in canalithiasis. It is the only mode that decays slowly enough to be relevant during the pathological deflection of the cupula which typically lasts for several seconds.

3. Comparison of different motion patterns

We are interested in the influence of the motion pattern on the response from the SCC. To this end we study three different acceleration patterns $\ddot{\alpha}(0 \le t \le 3\text{s})$ which lead to a rotation by 120°:

$$\ddot{\alpha}_{\mathrm{I}}(t) = \frac{2\sqrt{\pi}}{9 \cdot 0.004} \left[e^{-\left(\frac{t-0.02}{0.004}\right)^2} - e^{-\left(\frac{t-3.02}{0.004}\right)^2} \right], \tag{60a}$$

$$\ddot{\alpha}_{\mathrm{II}}(t) = \frac{8\sqrt{\pi}}{27 \cdot 0.004} \int_0^t \left[e^{-\left(\frac{\tau-0.01}{0.004}\right)^2} - 2e^{-\left(\frac{\tau-1.51}{0.004}\right)^2} + e^{-\left(\frac{\tau-3.01}{0.004}\right)^2} \right] \mathrm{d}\tau, \tag{60b}$$

$$\ddot{\alpha}_{\mathrm{III}}(t) = \frac{80\pi}{243} \left[t^3 - \frac{9}{2}t^2 + \frac{9}{2}t) \right]. \tag{60c}$$

The first pattern $\ddot{\alpha}_{\mathrm{I}}$ consists of two impulsive accelerations with opposite sign which lead to a constant angular velocity of 40°/s. This pattern cannot be realized in a clinical test since the peak accelerations are far too high. However, its mathematical treatment is straightforward and it provides a good reference for the other patterns. The second pattern $\ddot{\alpha}_{\mathrm{II}}$ prescribes a piecewise constant acceleration/deceleration of $53.3°/\mathrm{s}^2$ which causes a linear velocity increase up to 80°/s. It is a realistic pattern in the sense that such patterns can be tested in clinical experiments using computer-controlled three-dimensional rotating chairs. The third pattern $\ddot{\alpha}_{\mathrm{III}}$ follows a simple polynomial function. It leads to smooth velocity changes and comes closest to natural movements. Figure 5.2 shows the three patterns as functions of time.

Figure 5.3 shows the cupular volume displacement $V(t)$ according to (52) for the three different acceleration patterns. For small t we see that the cupular volume displacement V is approximately proportional to the respective angular velocity $\dot{\alpha}$ from figure 5.2. As time progresses the velocity error $\dot{\alpha}_e$ increasingly distorts the curves in figure 5.3 and V is now far from proportional to $\dot{\alpha}$. In particular, the velocity error (53) leads to a post-rotatory overshoot of V such

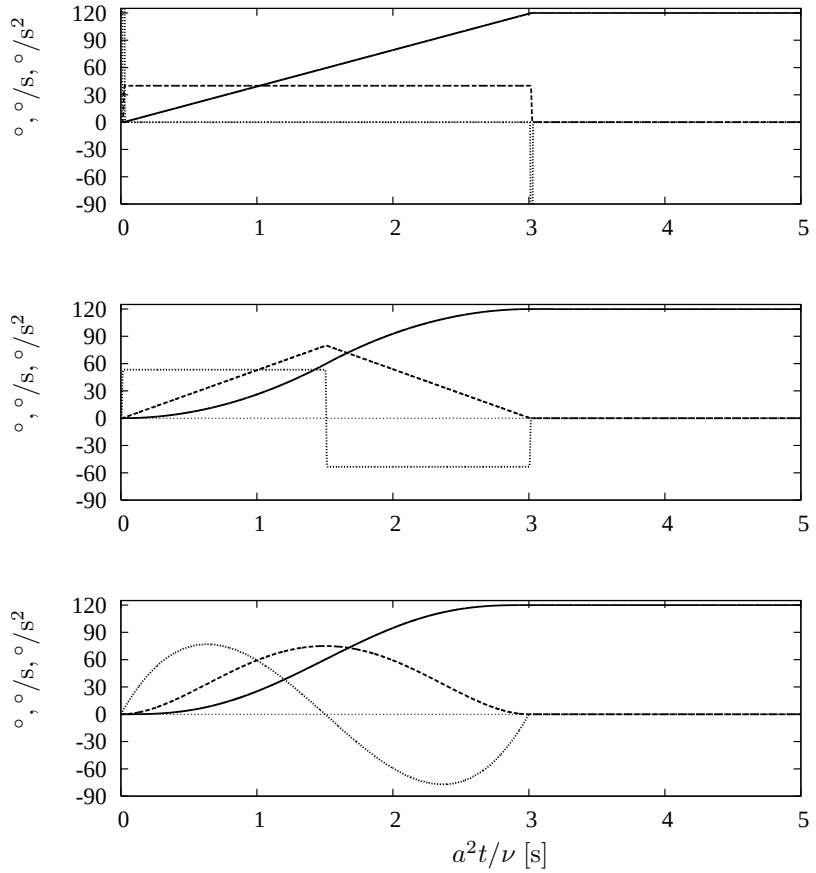

FIGURE 5.2. Acceleration patterns I, II & III (—— angle α, – – – angular velocity $\dot{\alpha}$, $\cdots$ angular acceleration $\ddot{\alpha}$)

that the cupula is deflected to the opposite side during the deceleration phase (for patterns II and III the overshoot starts at $t \approx 2.5$s). Moreover, after the head has come to a complete stop the cupula has not returned to its initial state. It returns only slowly with a fluid motion that is solely governed by the least stable eigenvalue σ_c. Note that the magnitude of the overshoot is approximately independent of the acceleration pattern.

One might expect that the overshoot of V creates a sensation of negative angular velocity since the value of V is beyond the threshold value V_t that we have derived in § 2. And indeed, such a sensation can be observed after a sudden

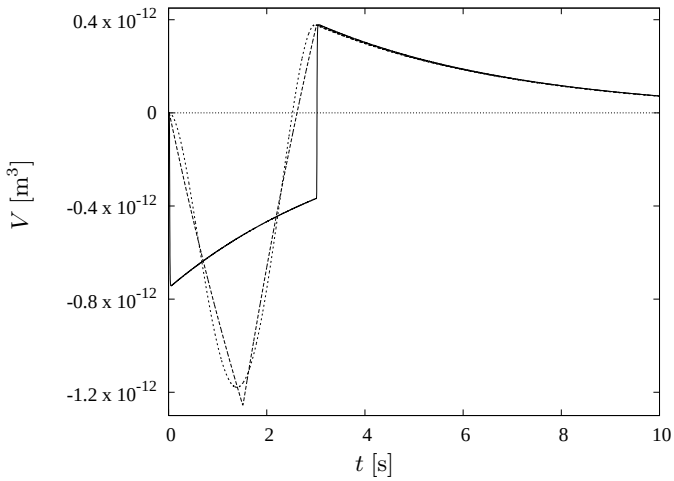

FIGURE 5.3. Cupular volume displacement V for the Dix-Hallpike maneuver (—— acceleration pattern I,– – – acceleration pattern II, $\cdots$ acceleration pattern III)

deceleration following a long period of constant angular velocity. However, we typically do not see it for the short Dix-Hallpike maneuver considered here. This apparent discrepancy between clinical experiments and our model could either be explained by the velocity storage mechanisms (see e.g. Raphan *et al.* (1979)) or by inappropriate choices for the geometrical parameters (Curthoys & Oman, 1987) or for the cupula time constant (Rabbitt *et al.*, 2009).

CHAPTER 6

Endolymphatic flow field in semicircular canals

The endolymphatic flow in the slender ducts of the SCCs is almost a Poiseuille flow with a parabolic velocity profile. We have already obtained this result from solving van Buskirk's equations which showed that the cupula mode and the slowest duct mode feature a (nearly) parabolic flow profile (cf. figure 4.6). Note that these results have been obtained without making any assumptions about the Reynolds or Womersley numbers. In this context, we only assumed that the flow in the SCCs is unidirectional along the main axis of the ducts. Furthermore, van Buskirk's model assumed that the flow in the utricle is very slow such that the viscous losses in the utricle can be neglected (Van Buskirk, 1977).

The results from van Buskirk's model for the semicircular canals indicate that typical endolymph flow velocities are on the order of $10^{-4}\,\mathrm{m/s}$. The Reynolds number for the slender duct is then on the order of 10^{-2}. Furthermore, most natural head maneuvers are sufficiently slow such that the associated Womersley number is below unity. Therefore, it is appropriate to assume that the endolymphatic flow field in semicircular canals is governed by the Stokes equations.

In order to compute numerical solutions of the Stokes equations in the complex morphology of the vestibular labyrinth, it is sensible to use boundary element methods (BEM). Boselli *et al.* (2010*b*) (see also Boselli *et al.*, 2010*a*, 2009; Obrist, 2007) developed a singularity method which is well suited for this study and which is closely related to BEM. We have used this method to compute the endolymphatic flow field in a single SCC for a rotatory motion from 0° to 120° as we have it used in Chapter 5 (cf. Eq. (57) and figure 5.1). The resulting flow field in the symmetry plane of the SCC is shown in figure 6.1.

1. Vortical flow in the SCC

The flow field within the slender duct exhibits, as expected, parabolic velocity profiles reminiscent of Poiseuille flow. The flow field after the maneuver due to the relaxation of the cupula after the post-rotatory overshoot (figure 6.1c) features parabolic velocity profiles also in the utricle. Obviously, the maximum velocity along the center-line of the utricle must be very small due to the continuity

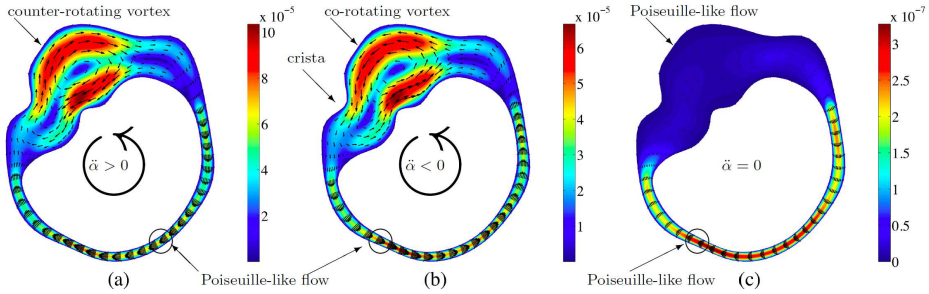

FIGURE 6.1. Velocity field in the symmetry plane at (a) $t = 0.8\,\mathrm{s}$ (acceleration), (b) $t = 1.8\,\mathrm{s}$ (deceleration), and (c) $t = 4\,\mathrm{s}$ (SCC at rest) for the head maneuver given in Eq. (57) and figure 5.1(b). The arrows are velocity vectors, while the color shows the velocity magnitude in m/s. ($T_c = 16\,\mathrm{s}$). The big arrows at the center indicate the direction of head rotation (from Boselli *et al.*, 2011).

equation. It is clear that the viscous losses in the utricle are negligible in this configuration.

The utricular flow fields during the acceleration and deceleration phases, however, show striking differences to the unidirectional flow that we have assumed in Chapter 3 for Van Buskirk's model. Instead of a Poiseuille-like flow, we find large vortical flows in the utricle. With respect to the head maneuver, the vortex is counter-rotating during acceleration and co-rotating during deceleration. Moreover, the maximum velocities within the utricle turn out to be of equal magnitude as the velocities in the slender duct. A careful analysis of the flow field reveals that there is a second vortex within the ampulla.

Further studies have shown that the existence of the utricular and ampullary vortices depends on the morphology of the SCC. It is clear that there are no vortices if we idealize the SCC as a perfect torus. Boselli *et al.* (2010*d*) showed that the vortices only exist if there are strong variations of the duct lumen. This is illustrated in figure which compares the flow in the membranous duct of a posterior SCC and a (hypothetical) flow in the bony labyrinth.

In order to confirm that the assumptions leading to the (steady) Stokes equations are correct, we performed simulations with a state-of-the-art finite volume solver for the incompressible Navier–Stokes equations (OpenFOAM). Figure 6.3 shows the flow field computed with this simulation. A detailed analysis of the velocity profiles shows that (a) the nonlinear advective terms as well as the Coriolis forces are negligible and that (b) the unsteady solution lags approximately

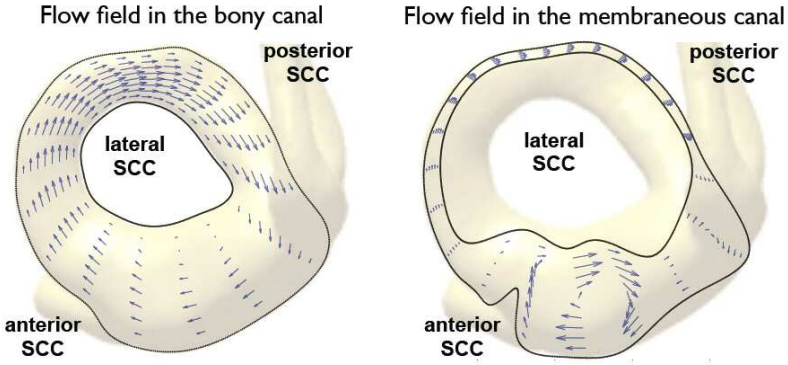

FIGURE 6.2. Flow fields during the counter-clockwise acceleration of a SCC in (a) the bony labyrinth (assuming that there is no membranous labyrinth) and (b) the flow field in the membranous duct a the SCC (from Boselli *et al.*, 2010*d*).

6 ms (in the slender duct) behind the quasi-steady solution for the Stokes equations. This time lag corresponds well to the time scale $T \approx a^2/(5.8\nu)$ of the first duct mode (which is neglected in the Stokes equations). We conclude that the observed vortices are genuine features of the endolymphatic flow during the acceleration and deceleration of the head. It should also be noted that these vortices are different from the vortical flow reported by Pau & Limberg (1990*b*) which were probably due to inertial flow caused by an improper scaling of the in vitro experiment.

2. Effect on the transduction of angular velocity

It remains to discuss the influence of the vortical flow in the ampulla and utricle on the normal operation of the vestibular system. It turns out that the utricular vortex has only very little effect on the proper operation of the SCCs. The cupular deflection remains well described by Van Buskirk's model (16). The otolith organs, however, may be influenced by the utricular vortex. This potential crosstalk between angular and linear acceleration sensors is discussed in Chapter 22.

The vortex in the ampulla may have a direct effect on the cupula which will deflect into an S-shape rather than a axisymmetric deflection in the shape of a paraboloid as suggested by Damiano & Rabbitt (1996). This S-shape results in larger deflection angles at the base of the cupula where the sensory hair cells are sitting. Therefore, the ampullary vortex may enhance the sensitivity of the SCC to angular motion. Furthermore, this vortex could also explain the phenomenon

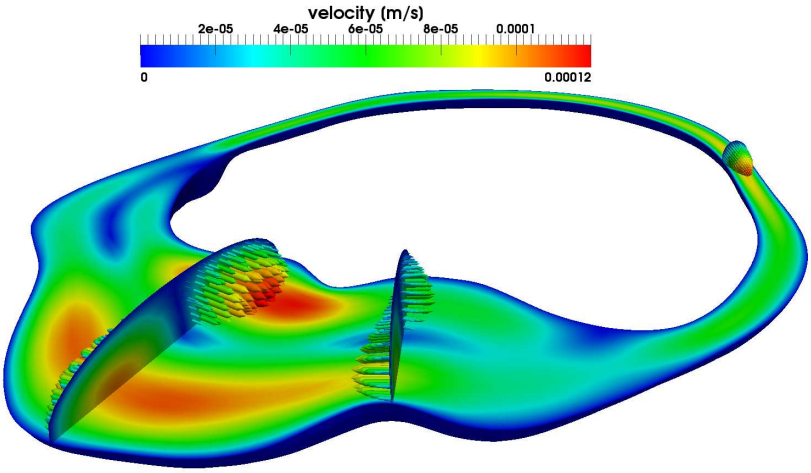

FIGURE 6.3. Rendering of the endolymphatic flow field within a single SCC during an acceleration of $120°/s^2$ in counter-clockwise direction (results obtained with an finite-volume solver for the Navier–Stokes equations with approximately 200 000 cells; courtesy of B. Grieser).

that there can remain some residual sensitivity to angular motion after a surgical plugging of an SCC. This plugging inhibits the flow in the slender duct, but it does not inhibit the formation of an ampullary vortex.

These results for the vortical flow in SCCs and its potential effect on the vestibular system is discussed in more detail in Boselli *et al.* (2011).

CHAPTER 7

Canalithiasis and BPPV

Benign paroxysmal positional vertigo (also known as *BPPV* or *top-shelf vertigo*) accounts for $20 - 30\%$ of all vertigo syndromes in humans (Baloh *et al.*, 1989). BPPV is suspected to be caused by small calcite particles floating freely in the semicircular canals (SCC) of the vestibular system located in the inner ear. This condition, known as *canalithiasis*, is the main subject of the present chapter.

The calcite particles are known as canaliths (figure 7.1). Most likely, these canaliths are otoconia (cf. figure 1.4) which have detached from the utricular macula due to traumatic impact or age. Their typical size is between 0.5 and $15\,\mu$m (Campos, 1990). There are reports (e.g. Parnes & Mcclure, 1992; Welling *et al.*, 1997) that canaliths can form larger clusters which can separate again into single canaliths due to repositioning. The relevance of this phenomenon will be discussed in Chapter 11.

The diagnosis of BPPV typically uses a series of head maneuvers commonly known as the Dix–Hallpike maneuver (Dix & Hallpike, 1952). First, the head is yawed by 45° toward the side of the ear to be tested. This aligns the plane of the posterior semicircular canal (this is the canal which is oriented like the rim of the pinna) with the sagittal direction of the body. The body is then tilted backward and the head extended so as to reach a rotation of 120° in the plane of the posterior semicircular canal. Figure 7.2 illustrates the Dix–Hallpike maneuver for a patient with the right ear affected by canalithiasis and BPPV.

Similar to the diagnostic head maneuver due to Dix & Hallpike (1952), there exist therapeutic head maneuvers known as Epley maneuvers (Epley, 1992). The Epley maneuvers aim at removing the canaliths from the slender ducts of the SCC by shifting them into the utricular cavity.

1. Theoretical, experimental and computational models of BPPV

BPPV due to canalithiasis has been studied theoretically and numerically by several authors (House & Honrubia, 2003; Squires *et al.*, 2004; Rajguru *et al.*, 2005; Obrist & Hegemann, 2008). Experiments investigating the physical mechanisms of BPPV on animal SCC have been presented by Suzuki *et al.* (1996*a*,*b*),

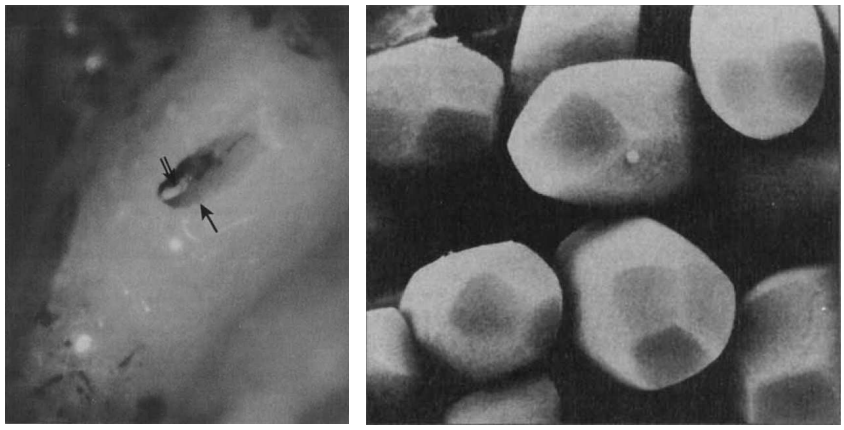

(a) (b)

FIGURE 7.1. (a) Canaliths (open arrow) in a fenestrated left posterior semicircular canal (filled arrow). (b) Normal human otoconia (courtesy of D. J. Lim, House Ear Clinic, Los Angeles, CA). Reprinted from Welling *et al.* (1997) with permission from the publisher.

Otsuka *et al.* (2003), Rajguru & Rabbitt (2007) and Valli *et al.* (2008). A review of BPPV from a medical point of view has been given by Furman & Cass (1999).

In vitro experiments with SCC are sparse although they allow a clearer definition of the experimental configuration, a better repeatability of the experiments and the possibility to perform larger systematic studies with varying experimental parameters. To our best knowledge, only the work of Pau & Limberg (1990*b*,*a*, 1988) on the flow in a healthy SCC and the work by Valli *et al.* (2006) and Obrist *et al.* (2010) on canalithiasis have been published so far. To improve the handling, these in vitro models are usually scaled up while it must be ensured that this scaling does not alter the relevant physical processes. The in vitro model by Obrist *et al.* (2010) will be presented in detail in Chapter 9.

2. Landmarks of top-shelf vertigo symptoms

Results from clinical experiments are widely available. Figure 7.3 shows the nystagmus velocity of a typical BPPV patient with canalithiasis during and after a head maneuver. In this clinical experiment (performed at the *Interdisciplinary Center for Vertigo & Balance Disorders* by Drs. C. Bockisch and S. Hegemann) the eye movements were recorded in a magnetic frame (Remmel-type system,

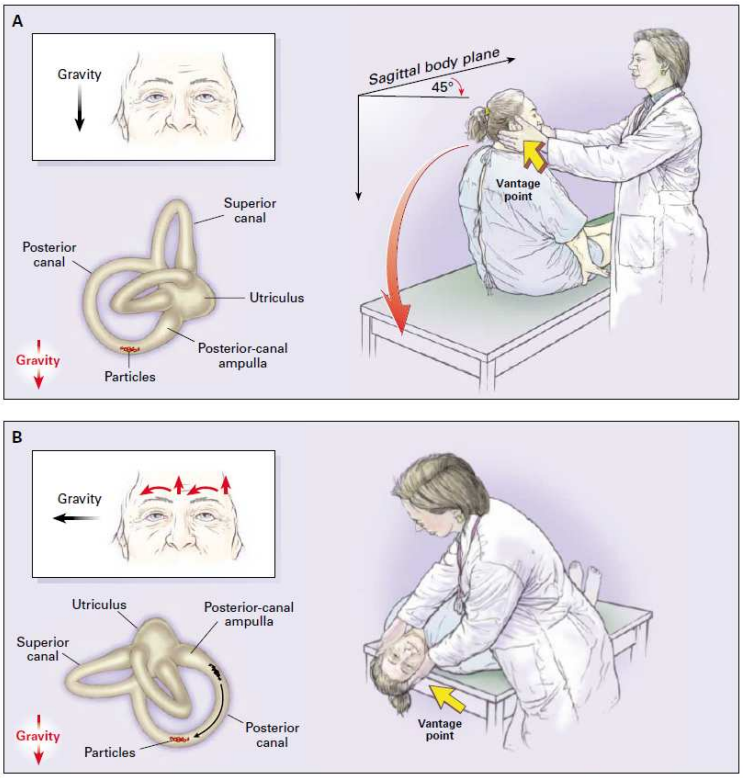

FIGURE 7.2. Illustration of the Dix–Hallpike maneuver for a patient with canalithiasis in the right ear. Reprinted from Furman & Cass (1999) with permission from the publisher.

modified by Lasker, Baltimore) using dual scleral search coils (Skalar Instruments, Delft). A search coil was placed on the right eye around the cornea (after anesthetizing the conjunctiva with oxybuprocaine 0.4%). The angular velocity was computed according to Hepp (1990) and Tweed *et al.* (1990).

During the movement of the head ($-3\text{s} < t < 0\text{s}$) the nystagmus velocity N is approximately proportional to the head velocity. This is called the *per-rotatory nystagmus* which is the normal reaction to an angular head movement. It is symptomatic for canalithiasis patients that there is a second nystagmus after a certain *onset-latency* T_L. We call this the *positional nystagmus*. It is pathological and causes vertigo. The onset-latency T_L, the time to peak T_P and the maximum strength of the nystagmus $N_{\max}$ are the landmarks which characterize a positional nystagmus. In clinical testing it is found that these values may differ

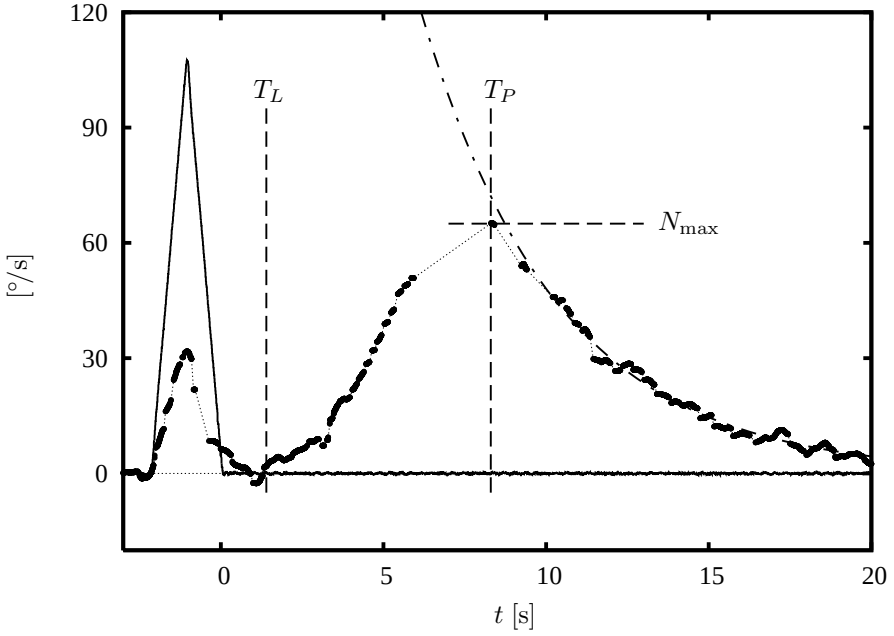

FIGURE 7.3. Nystagmus velocity N (•) and head velocity (——) of a canalithiasis patient during and after a head maneuver. The time T_P and magnitude $N_{\max}$ of the maximum nystagmus velocity are only estimates due to incomplete data between $t = 6$s and 10s. After its peak ($t > 10$s) the positional nystagmus decays approximately like $\exp(-t/4.2\text{s})$ (— · —).

substantially between different patients, different head maneuvers or even different instances of the same experiment. The onset-latency, for instance, typically lasts for a few seconds but there are also cases where the positional nystagmus starts immediately after the head maneuver. The total duration of the positional nystagmus ranges typically from 10 to 60s (Aw *et al.*, 2005). A priori, it is not clear whether these different characteristic values are related to different sizes or numbers of particles in the SCC. However, we will present results (e.g. figure 8.4) which show that different particle sizes and numbers have a direct effect on the duration and intensity of the positional nystagmus, and we will show (figure 8.5) that certain particle sizes and numbers may lead to a vanishing onset-latency.

CHAPTER 8

Analytical model for canalithiasis

Theoretical work on BPPV is still relatively sparse. Only recently papers by House & Honrubia (2003), Rajguru *et al.* (2004, 2005), Squires *et al.* (2004) and Obrist & Hegemann (2008) brought forward mathematical models for BPPV. This chapter is based on the most recent paper (Obrist & Hegemann, 2008) which presented an analytical study of BPPV on the basis of Van Buskirk's model for SCC (Chapter 3). It has the aim to reveal the principal mechanisms leading to the positional nystagmus. We will identify the important parameters and their relation to the landmarks of BPPV (e.g. onset-latency, time to peak and peak nystagmus velocity; Chapter 7).

In contrast to earlier investigations, we deliberately choose an idealized geometry limited to a single SCC with constant circular cross-section in the slender part. This is in strong contrast to the work of Squires *et al.* (2004) which heavily relies on the varying cross-section of the SCC. It is also different from Rajguru *et al.* (2004, 2005) who used a detailed three-dimensional model of all three SCC which allowed them to study complex head maneuvers. Here, we aim to idealize the problem as much as possible and to retain as little as necessary. This will allow us to study the principal mechanisms in great detail. Our idealized model is able to offer: clear explanations for certain phenomena, explicit expressions for the characteristic features of the positional nystagmus, and the dimensionless numbers which are most relevant to canalithiasis.

The fluid dynamics of healthy SCC (without particles) has been discussed previously in chapters 3, 5 and 6. Here, we start by deriving a fluid-particle model for canalithiasis with two-way coupling (§ 1). The governing equations feature several dimensionless coefficients which indicate the relevance of the different physical phenomena. Numerical solutions of the governing equations are studied in § 2 which will explain the central mechanisms of canalithiasis. We will describe a mechanism for the onset-latency. In contrast to the explanation offered by Squires *et al.* (2004) this mechanism does not require the particles to be located within the ampulla at the beginning of the maneuver. Also, it will be shown that the onset-latency may vanish under certain conditions (figure 8.5). In addition, section 2 includes a parameter study to illustrate the influence of size and number of the particles on the positional nystagmus. In § 3 a linearized

version of the governing equations is analyzed in detail. We will find analytical approximations for the temporal eigenvalues. From this we will define a Stokes number which relates the particle size directly to the positional nystagmus. These results will allow us to formulate a reduced order model in § 4 from which we can derive explicit relations between the landmarks of BPPV and the particle properties. These relations show that the Stokes number is one of the most relevant parameters for canalithiasis. We will demonstrate how these relations might be used to diagnose the particle size from clinical data. We conclude this chapter with an brief excursion to non-normal operators (§ 5) where we will show that top-shelf vertigo can also be understood as a transient growth phenomenon in a damped mechanical system.

1. Governing equations for the semicircular canal with particles

The governing equations for the particulate flow in the SCC are based on Van Buskirk's equation (16) to which we add an equation for the particle motion. In addition, we introduce coupling terms to model the fluid-particle interaction.

The modeling of the particle dynamics is a critical issue. The particle velocities and trajectories have a direct impact on the endolymph flow and on the positional nystagmus. The particles are calcite particles (otoconia) presumably detached from the macula of the utricle. Campos (1990) reports radii in the range from $0.5\,\mu$m to $15\,\mu$m. However, the actual number, size and shape of particles in the SCC of canalithiasis patients is not known, and it is likely that the particles are non-spherical and that collisions between particles will occur. It is also clear that the particles will directly interact with the wall at some point. Whether they are likely to stick to the wall or whether they will roll or slide along the wall is not known. An accurate prediction of the particle trajectories is obviously very difficult. Nevertheless, it is possible to make some reasonable idealizations which allow us to understand the principal mechanisms of canalithiasis.

Squires *et al.* (2004) used a two-dimensional particle model which keeps track of the radial and the axial position of a particle. Their model is based on asymptotic results for small spheres settling in circular pipes under Stokes flow conditions (Bungay & Brenner, 1973; Happel & Brenner, 1973). In this model the pressure drop due to a settling particle is highest if the particle falls along the centerline of the pipe. As the particle approaches the wall the pressure decreases. Further, Squires *et al.* introduce a lubrication gap between the particle and the wall (1μm) to prevent the particles from sticking to the wall. This lubrication gap allows the particles to slide along the wall with 30% or more of their free-fall velocity. At the same time Squires *et al.* assume that the pressure drop due to particles is negligibly small if they slide along the wall.

Rajguru & Rabbitt (2007) showed recently in an animal experiment that the hair cells in the cupula are also stimulated by particles which are sliding along

the wall. They explain this apparent contradiction between their experiment and the assumptions of Squires *et al.* with the size of the particles: whereas the model of Squires *et al.* is derived for small particles, Rajguru & Rabbitt used relatively large particles ($> 10\%$ of the canal diameter). This suggests that the pressure drop due to (larger) particles sliding along the wall is not negligible.

A more pragmatic approach to particle modeling was taken by House & Honrubia (2003) and Rajguru *et al.* (2004). They formulated a one-dimensional particle model based on Stokes' formula for the drag of a sphere in an unbounded fluid. This model tracks only the axial position of the particles in the SCC. The most striking difference between the two approaches lies in the pressure drop. Whereas the pressure drop of Squires *et al.* varies strongly with respect to the radial position, the pressure drop of House & Honrubia is independent of the radial position. If the particle is at the center of the canal the model of House & Honrubia underpredicts the pressure drop by a factor two and it overpredicts the pressure drop if the particle is close to the wall. Averaged over the circular cross-section, however, the pressure drop is equal for both models. In this light, we can expect that (on average) the two models should give similar predictions for the cupula displacement if we assume that a particle passes through different radial positions during the course of a positional nystagmus. In the present chapter, we assume that the one-dimensional particle model is sufficiently accurate for a study of the principal mechanisms of canalithiasis. We will discuss this assumption in Chapter 10 by studying experimental and further numerical results obtained with more sophisticated particle models.

For the formulation of our one-dimensional particle model we consider n_p particles of radius a_p and mass m_p which move freely in a SCC (figure 8.1). Their motion is governed by the particle inertia, the Stokes drag of the particle, the particle gravity and an external forcing (angular motion of the head). Their axial position is denoted by $x_p(t)$ (measured relative to the SCC). The origin $x_p = 0$ is set to the (initially) lowest point in the canal,

$$x_p(0) = \dot{x}_p(0) = 0. \tag{61}$$

The particle equation of motion,

$$m_p(\ddot{x}_p + R\ddot{\alpha}) = F_s + F_g, \tag{62}$$

includes a term for the particle inertia $m_p(\ddot{x}_p + R\ddot{\alpha})$ and two terms for external forces: the gravitational force,

$$F_g = -m_p(1 - \rho/\rho_p)g\sin(x_p/R + \alpha), \tag{63}$$

and a Stokes drag force for a sphere of radius a_p,

$$F_s = -6\pi\nu\rho a_p(\dot{x}_p - u_p). \tag{64}$$

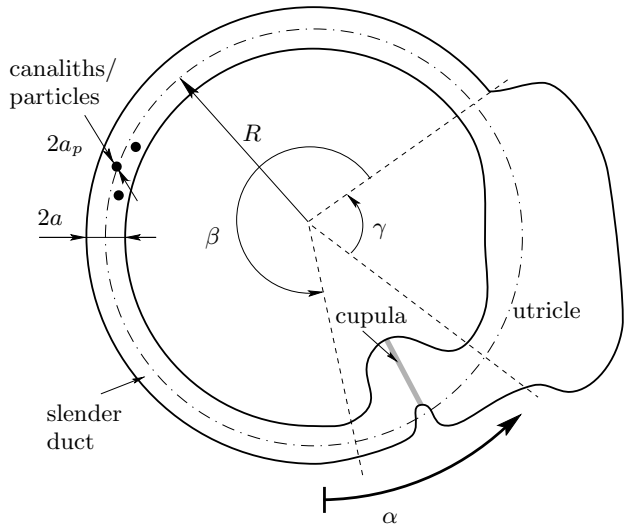

FIGURE 8.1. Schematic of a single SCC with geometrical parameters (not to scale).

The velocity u_p is the local fluid velocity at the particle location. Since we do not keep track of the radial position we approximate the u_p by the bulk velocity of the fluid,

$$u_p = \frac{2\pi}{A_c} \int_0^a u(r', t)\, r' \mathrm{d}r'. \tag{65}$$

At the same time we introduce the Stokes drag (64) to the fluid equation (14). To this end, we assume that the Stokes drag F_s of n_p particles induces an axial pressure gradient $-n_p F_s/(A_c \beta R)$ along the slender duct.

Again, we use the dimensionless variables (15) and $\tilde{x}_p(\tilde{t}) = x_p(t)/R$. Furthermore, we define the Froude number Fr as

$$Fr^2 = \frac{R}{g T_v^2 (1 - \rho/\rho_p)}. \tag{66}$$

The Froude number is a dimensionless coefficient occurring frequently in problems which involve fluid dynamics and gravity. It relates inertial forces ($\sim a_p^3 \rho_p R/T_v^2$) to gravity forces ($\sim a_p^3(\rho_p - \rho)g$). For the parameters from table 3.1 we get $Fr^2 = 0.79052$. Since $Fr^2 = O(1)$ the inertial and gravity forces play an equally important role in canalithiasis. With these definitions the governing equations

for the particulate flow in a SCC are

$$\frac{\partial}{\partial\tilde{t}}\tilde{u} - \frac{1}{\tilde{r}}\frac{\partial}{\partial\tilde{r}}\left(\tilde{r}\frac{\partial}{\partial\tilde{r}}\tilde{u}\right) + \epsilon\int_0^{\tilde{t}}\int_0^1 \tilde{u}\,r'\mathrm{d}r'\mathrm{d}t' + \chi\left(2\int_0^1 \tilde{u}\,r'\mathrm{d}r' - \frac{\partial}{\partial\tilde{t}}\tilde{x}_p\right) = -(1+\gamma/\beta)\frac{\partial^2}{\partial\tilde{t}^2}\alpha, \quad (67a)$$

$$\frac{\partial^2}{\partial\tilde{t}^2}(\tilde{x}_p+\alpha) + \xi\left(\frac{\partial}{\partial\tilde{t}}\tilde{x}_p - 2\int_0^1 \tilde{u}\,r'\mathrm{d}r'\right) + \frac{1}{Fr^2}\sin(\tilde{x}_p+\alpha) = 0, \quad (67b)$$

with the initial and boundary conditions

$$\tilde{u}(\tilde{r},0) = \frac{\partial}{\partial\tilde{t}}\tilde{u}(\tilde{r},0) = \tilde{x}_p(0) = \frac{\partial}{\partial\tilde{t}}\tilde{x}_p(0) = 0, \quad (68a)$$

$$\tilde{u}(1,\tilde{t}) = \frac{\partial}{\partial\tilde{r}}\tilde{u}(0,\tilde{t}) = 0. \quad (68b)$$

In contrast to Van Buskirk's equation (16) the system of equations (67) is now nonlinear because of the circular shape of the SCC which leads to a sine function in the gravitational force term in (63). The governing equations contain two new dimensionless coefficients ξ and χ,

$$\xi = \frac{9\rho a^2}{2\rho_p a_p^2}, \quad (69a)$$

$$\chi = \frac{3a_p n_p}{\beta R}. \quad (69b)$$

It will become clear in § 3 that the coefficient ξ determines the time it takes for particles to adjust their own velocity to the velocity of the surrounding flow. The higher the value of ξ, the quicker the particles adjust their velocities to the surrounding flow. Typical values for ξ lie around 10^2 (for large particles, $a_p \approx 20\mu$m) and 10^5 (for very small particles, $a_p < 1\mu$m) which means that particles adjust their velocity 10^2 times (or 10^5 times, respectively) more rapidly than T_v. The physical meaning of the coefficient χ is much different. Its value determines the impact of the particle motion on the fluid flow. Typically, χ is very small ranging from approximately 10^{-4} (one very small particle) to 10^{-2} (many large particles). Nevertheless, it would be wrong to neglect χ since no positional nystagmus could be observed without it. Typical values for the used dimensionless coefficients are listed in table 8.1. Unless noted otherwise these values will be used in the following sections.

TABLE 8.1. Values of the dimensionless coefficients for different particle sizes a_p (the Stokes number St will be defined in § 3).

a_p	ξ	χ	St	ϵ	Fr^2
1μm	42666.67	$0.000213 \times n_p$	205.58	0.09752	0.79052
5μm	1706.67	$0.001066 \times n_p$	8.22	0.09752	0.79052
10μm	426.67	$0.002132 \times n_p$	2.06	0.09752	0.79052
15μm	189.63	$0.003197 \times n_p$	0.91	0.09752	0.79052
20μm	106.67	$0.004263 \times n_p$	0.51	0.09752	0.79052
25μm	68.27	$0.005329 \times n_p$	0.33	0.09752	0.79052
30μm	47.41	$0.006395 \times n_p$	0.23	0.09752	0.79052

2. Numerical study of the principal mechanisms

The governing equations (67) can be solved numerically in a straightforward manner. The nonlinear terms are integrated with respect to time with an explicit scheme and we use an implicit Crank–Nicolson scheme for the linear terms to cope with the numerical stiffness of the problem. The spatial derivatives are discretized with a central sixth-order compact finite difference scheme (one-sided lower order schemes at the boundaries) on an equidistant grid (e.g. Ferziger & Perić, 2002). This discretization method yields an efficient and robust simulation code.

Figure 8.2 shows a typical solution of (67) for the maneuver from figure 5.1(b). During the head maneuver (*per-rotatory phase*, $t < 0$) we observe that the cupula displacement $V(t)$ follows qualitatively the curve of the head velocity $\dot{\alpha}(t)$. Immediately after the head maneuver has ended there is an overshoot. This overshoot is somewhat smaller than the overshoot in the healthy SCC due to influence of the particles. Up to this point the solution is qualitatively the same as for the healthy SCC. In the *post-rotatory phase* ($t > 0$) the cupula displacement $V(t)$ crosses the zero axis a second time at $t = T_L$ (onset-latency) instead of relaxing to zero slowly and monotonically. The cupula only returns to its relaxed position after its deflection has reached a local extremum $-V_{\max}$ at $t = T_P$ (time to peak). This behaviour of the cupula corresponds to the positional nystagmus observed with canalithiasis patients (cf. figure 7.3). The second crossing of the zero axis and the subsequent local extremum of the cupula displacement is perceived as a secondary angular motion which leads to the positional nystagmus and causes vertigo.

We would like to emphasize the observation that the onset-latency is caused by the overshoot of the cupula. This is an alternative to the explanation offered by Squires *et al.* (2004) who related the onset-latency to the passage of the particles from the ampulla into the slender duct. Our explanation also holds if the initial

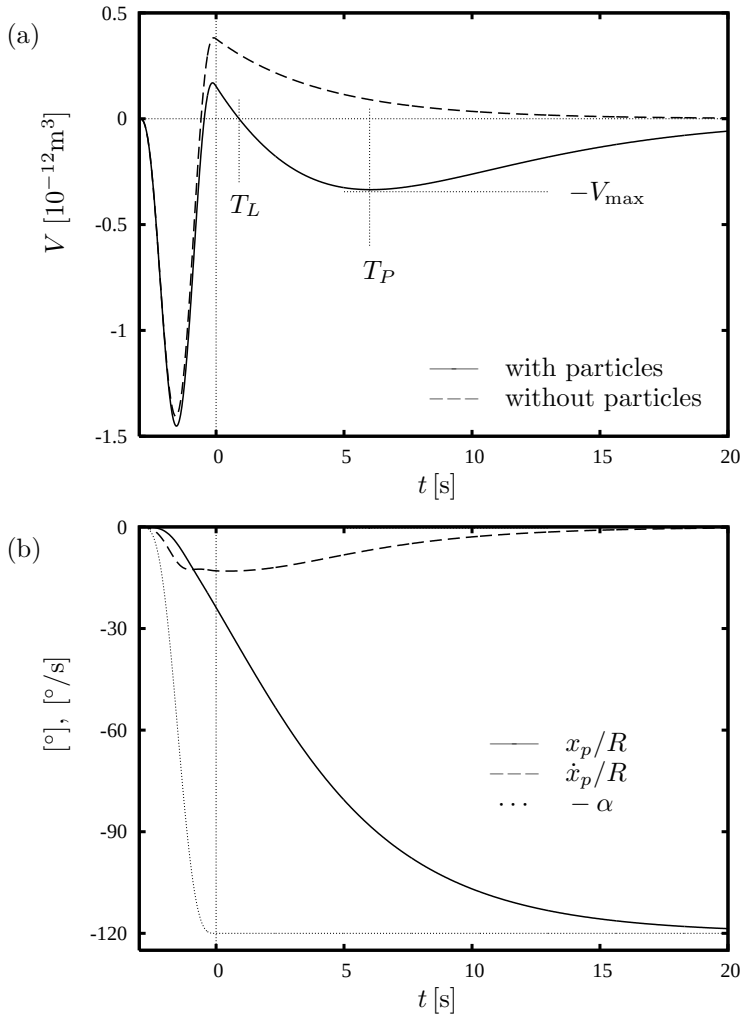

FIGURE 8.2. Numerical simulation of (a) the cupula displacement $V(t)$ and the (b) particle position $x_p(t)$ and velocity $\dot{x}_p(t)$ for a SCC with seven particles ($n_p = 7$) of radius $a_p = 14\mu$m ($\epsilon = 0.09752$, $Fr^2 = 0.79052$, $\xi = 217.69$, $\chi = 0.02089$). For comparison (a) shows again the cupula displacement of a healthy SCC from figure 5.1(a).

location of the particles is not in the ampulla (a possibility indicated, for instance, in Appendix A of Rajguru *et al.*, 2004).

The particle motion $x_p(t)$ can also be split into a per-rotatory and a post-rotatory phase. In the per-rotatory phase ($t < 0$) the particles accelerate such that they attain their maximum velocity at the end of the head maneuver. During the post-rotatory phase ($t > 0$) the particles fall down through the canal. At the same time they gradually decelerate such that they come to a halt when they reach the lowest position in the canal. There is no oscillation about the lowest position. The particles behave like the mass of an overdamped pendulum.

The corresponding results for $n_p = 10$ and $a_p = 11\mu$m are shown in figure 8.3 as a sequence of schematic drawings. It documents the two-phase process of canalithiasis: particle positioning during the per-rotatory phase and secondary endolymph flow during the post-rotatory phase which is induced by the falling particles.

We study the influence of n_p and a_p on the characteristic values T_L, T_P, and $V_{\max}$ by varying n_p from 1 to 50 and a_p from 1 to 30μm (figure 8.4). Note that we are covering here a wider range of particle sizes than suggested by Campos (1990) because we also want to consider large lumps of smaller particles. As mentioned earlier, the actual number and size of particles present in the SCC of a canalithiasis patient is not known. We can only estimate the particle size and number by comparing clinical data to results from theoretical models and experiments. Rajguru & Rabbitt (2007) concluded from their study that canalithiasis "most likely involves particles on the order of 5-20μm". We will try in § 4 to estimate the particle size for the data shown in figure 7.3.

As a general trend we observe that more and larger particles lead to a shorter onset-latency and an earlier and more intense peak nystagmus. Curve fitting suggests that the magnitude of the positional nystagmus is proportional to the total particle cross-section ($\pi a_p^2 n_p$). There are also configurations for which the onset-latency T_L vanishes (figure 8.5a). In these cases the particle-induced flow is so strong that there is no overshoot, i.e. the positional nystagmus follows the head movement seamlessly (figure 8.5b). This phenomenon has also been observed in clinical experiments.

Rajguru *et al.* (2004) found that the time to peak is proportional to $1/a_p^2$ if the total particle mass $M_p = n_p m_p$ is kept constant (figure 5(c) in their paper). Our results (figure 8.6a) agree with their observations at least for smaller particles and large M_p. Furthermore, in figure 8.6(b) we observe that the peak nystagmus decreases for larger particles if M_p is kept constant. To understand this effect we need to take into account our previous observation that $V_{\max}$ scales approximately like $a_p^2 n_p$, at the same time we keep the total particle mass constant, i.e. , $n_p \propto a_p^{-3}$ constant. It follows that $V_{\max}$ must decrease with increasing particle size.

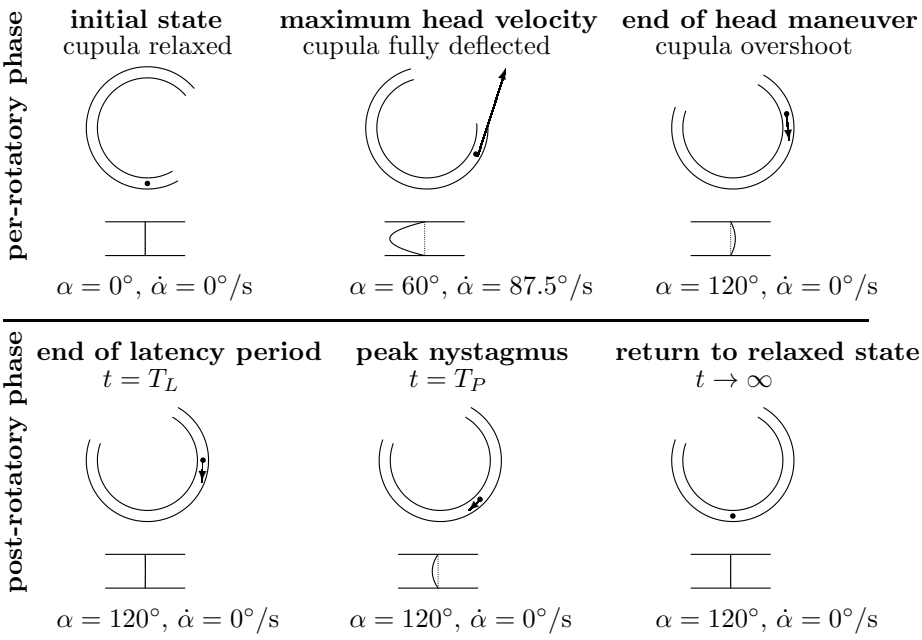

FIGURE 8.3. Schematics of the SCC with particles ($a_p = 11\mu$m, $n_p = 10$; $\epsilon = 0.09752$, $Fr^2 = 0.79052$, $\xi = 352.61$, $\chi = 0.02345$) during a head maneuver (the arrow shows the absolute particle velocity $\dot{x}_p + R\dot{\alpha}$; the cupula is drawn separately below the canal as a bulged membrane).

3. Analysis of the linearized equations

In order to obtain a deeper understanding of the fluid-particle dynamics in SCC we linearize the governing equations (67). To this end, we assume that the angle $\phi = x_p/R + \alpha$ (spanned by the particle angle x_p/R and the direction of gravity $-\alpha$) is small, such that

$$\sin\phi \approx \phi = x_p/R + \alpha.$$

This approximation may introduce a sizable error for angles of 90° and more, but we will see that the results obtained from the linearized problem remain qualitatively correct and that they will help us to understand the observations of § 2.

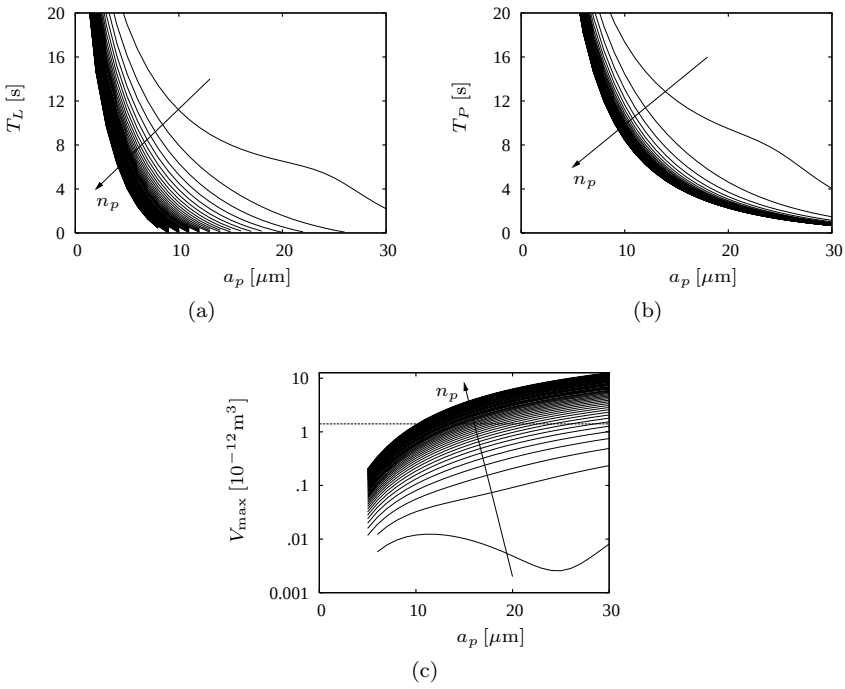

FIGURE 8.4. Influence of the particle size a_p and the particle number n_p on the characteristic values of the positional nystagmus (curves for $n_p = 1, 2, \ldots, 50$); the dotted line in (c) indicates the maximum cupula displacement in the per-rotatory phase.

We write the linearized governing equations (67) as

$$\frac{\partial}{\partial \tilde{t}}\mathbf{Q}\mathbf{u} = \mathbf{P}\mathbf{u} + \mathbf{f}, \tag{70}$$

where $\mathbf{Q}$, $\mathbf{P}$ are operator matrices. The vector $\mathbf{u}$ contains the dependent variables $\tilde{u}$ and $\tilde{x}_p$ and $\mathbf{f}$ contains the forcing terms.

To study the temporal spectrum of (70) we set $\dot{\alpha}$ to zero which corresponds to the situation after the head maneuver ($t > 0\,\mathrm{s}$). The governing equations (70) then form a homogeneous initial value problem in which the initial values are the result of a completed head maneuver. With the separation ansatz

$$\mathbf{u}(\tilde{r}, \tilde{t}) = \hat{\mathbf{u}}(\tilde{r})e^{-\sigma\tilde{t}}, \tag{71}$$

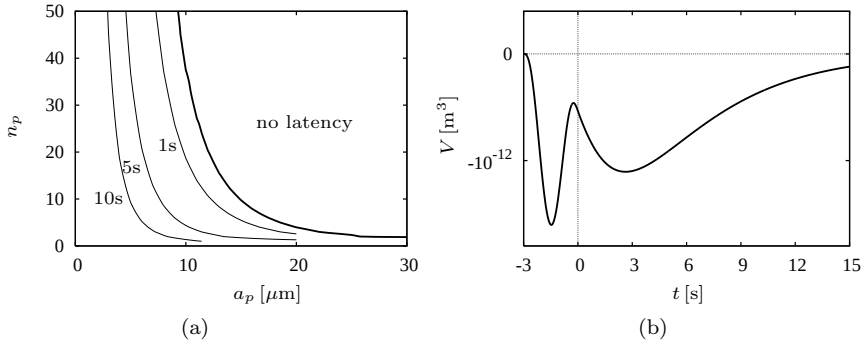

FIGURE 8.5. Vanishing onset-latency: (a) latency T_L as a function of the particle size a_p and number n_p; (b) cupula displacement $V(t)$ for a configuration without onset-latency ($a_p = 20\mu$m, $n_p = 10$).

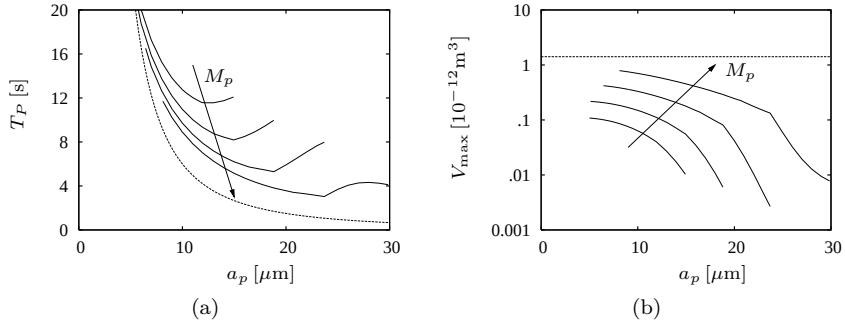

FIGURE 8.6. (a) Time to peak T_P and (b) cupula displacement $V_{\max}$ as a function of a_p if the total particle mass M_p is kept constant ($n_p \propto a_p^{-3}$). The dotted line in (a) indicates the proportionality of T_P to $1/a_p^2$; the dotted line in (b) indicates the maximum cupula displacement in the per-rotatory phase.

we obtain the generalized eigenvalue problem

$$-\sigma \mathbf{Q}\hat{\mathbf{u}} = \mathbf{P}\hat{\mathbf{u}}. \tag{72}$$

A numerical solution of this problem is shown in figure 8.7(a). The eigenvalues of the cupular mode and the duct modes are nearly at the same locations as in the configuration without particles (cf. figure 4.1). In addition, there are two new eigenvalues attributable to the particle equation. We can find estimates for the two new eigenvalues by analyzing the decoupled linearized particle equation

$$\frac{\partial^2}{\partial \tilde{t}^2}\tilde{x}_p + \xi \frac{\partial}{\partial \tilde{t}}\tilde{x}_p + Fr^{-2}\tilde{x}_p = 0. \tag{73}$$

Assuming that $Fr^{-2} \ll \xi$ we find

$$\sigma_s \approx \frac{1}{Fr^2 \xi}, \qquad \sigma_f \approx \xi, \tag{74}$$

We name the corresponding modes the *slow particle mode* σ_s and the *fast particle mode* σ_f. Inspection of the numerical results shows that the expressions (74) are indeed good estimates for the eigenvalues of (72).

These results motivate the definition of a Stokes number which relates a typical time constant for the particle motion to a typical time constant of the fluid flow. The classical choice for a Stokes number relates the fast particle mode to the viscous time scale T_v,

$$St_{\text{classical}} = \xi^{-1} \ll 1 \tag{75}$$

The fact that $St_{\text{classical}}$ is very small for typical particle sizes suggests that the particles behave like passive tracers which follow the streamlines and have negligible influence on the fluid (e.g. Clift *et al.*, 1978). Obviously, this Stokes number does not tell the full story and it is not useful in the context of canalithiasis. Therefore, we discard the definition (75) and define a different Stokes number from the estimated time scales for the slow particle mode and the cupula mode,

$$St = \frac{\sigma_c}{\sigma_s} = \frac{\epsilon Fr^2 \xi}{16} = \frac{9\pi K a^4}{16\beta\, a_p^2\, g(\rho_p - \rho)}. \tag{76}$$

For the typical parameters from table 3.1 we find that St may be below as well as above unity. We will see in the following that this Stokes number and the two least stable modes (cupula mode and slow particle mode) play a central role in canalithiasis.

Therefore, we examine these two modes in some more detail. The two estimates (27) and (74) actually suggest that the two eigenvalues coincide for $St = 1$. For the standard parameters from table 3.1 this would be the case for $a_p \approx 14.3\mu$m. Figure 8.7(b) investigates this idea by comparing the approximate expressions (27) and (74) to the numerically computed eigenvalues. We find that the two eigenvalues never coincide. Rather, they repel each other as we approach $St = 1$. This repulsion becomes stronger for larger numbers of particles n_p. For small particle radii ($St > 1$) the eigenvalues follow closely the estimates (27) and (74). For $St < 1$, however, the eigenvalues have switched roles:

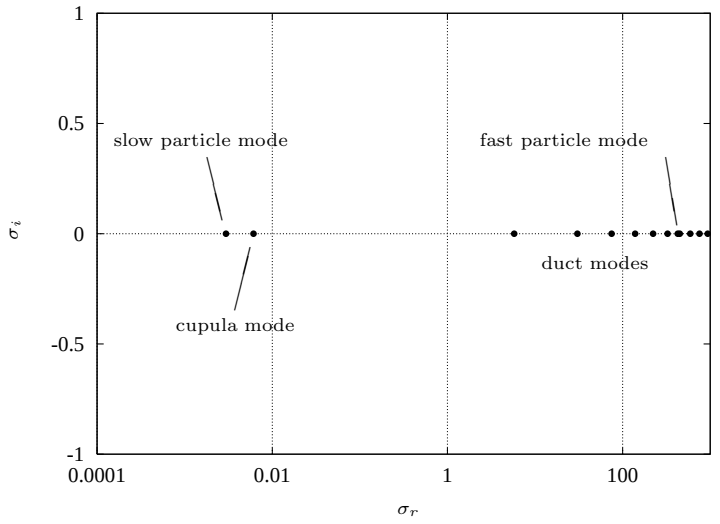

(a)

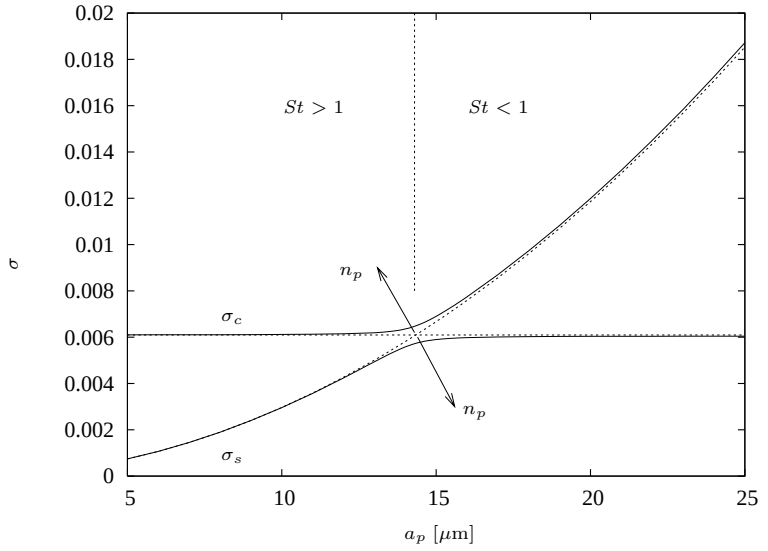

(b)

FIGURE 8.7. (a) Eigenvalues $\sigma = \sigma_r + \mathrm{i}\sigma_i$ for ten particles with radius $a_p = 10\mu$m. (b) Eigenvalues σ_s (slow particle mode) and σ_c (cupula mode) as a function of the particle radius a_p (n_p=10); the dashed lines show the estimates $\epsilon/16$ and $1/(Fr^2\xi)$.

the cupula eigenvalue σ_c follows the estimated curve for the slow particle mode and vice versa. As a result, the cupula mode always decays faster than the slow particle mode. In other words, the slow particle mode will prevail as $t \to \infty$.

The change of roles shows also in figure 8.8(a) where we plotted the ratio θ between the bulk velocity

$$\bar{u} = 2 \int_0^1 u\, r \, \mathrm{d}r \tag{77}$$

and the particle velocity $-\sigma\hat{x}_p$ where θ_c and θ_s are the ratios for the cupula mode and the slow particle mode, respectively. This plot shows us two things. First, we note that the fluid velocity and the particle velocity always point in the same direction (co-flow) in the cupula mode whereas they always point in opposite directions (counter-flow) in the slow particle mode. Second, we find that the particle velocity is dominant ($|\bar{u}| \ll |-\sigma\hat{x}_p|$) in the slow particle mode for $St > 1$ and that it is dominant in the cupula mode for $St < 1$. Hence, the switching of roles at $St = 1$ is manifested in the dominance of the particle velocity over the fluid velocity.

As a final result in this section we derive the universal approximation θ_u for the ratio between the fluid bulk velocity and the particle velocity. To this end, we enter the approximate eigensolution for the slow particle mode into the linearized governing equations, i.e. , a parabolic velocity profile for the endolymph and $\hat{x}\exp(-\tilde{t}/Fr^2\xi)$ for the particle motion. From this we obtain

$$\theta_u = \frac{\bar{u}}{-\sigma\hat{x}} = \frac{-\chi St}{16St^2 - (16 + 2\chi)St + \epsilon/4}. \tag{78}$$

This expression approximates θ_c for $St < 1$ and θ_s for $St > 1$ (figure 8.8(b)).

We would like to emphasize that the number of particles n_p plays a small but, nevertheless, very important role here. Figure 8.7(b) shows that the values of σ_c and σ_s can be predicted relatively well by the estimates (27) and (74) which are both independent of the particle number. Only for $St \approx 1$ the particle number has a noticeable influence on σ_s and σ_c. In that sense, the influence of n_p is small. At the same time the effect of a non-zero n_p is huge in the sense that the cupula mode and the fast particle mode switch roles at $St = 1$. They would not do that if n_p were zero. This observation goes along with our comment at the end of § 1, where we mentioned that χ (which is proportional to n_p) must not be neglected even though it is very small.

4. Reduced-order model for canalithiasis

Figures 7.3 and 8.2 suggest that the cupula oscillates about its relaxed state at least once during the first few seconds after the head maneuver. This appears to contradict the results from the previous section where we have found that all modes decay monotonically as $t \to \infty$. To explain this transient oscillation

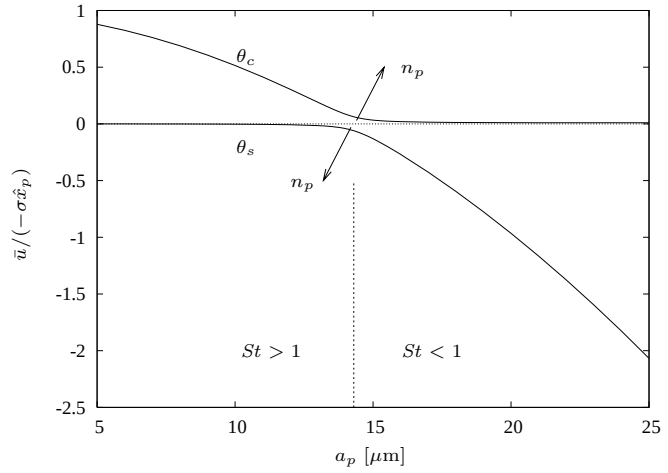

(a)

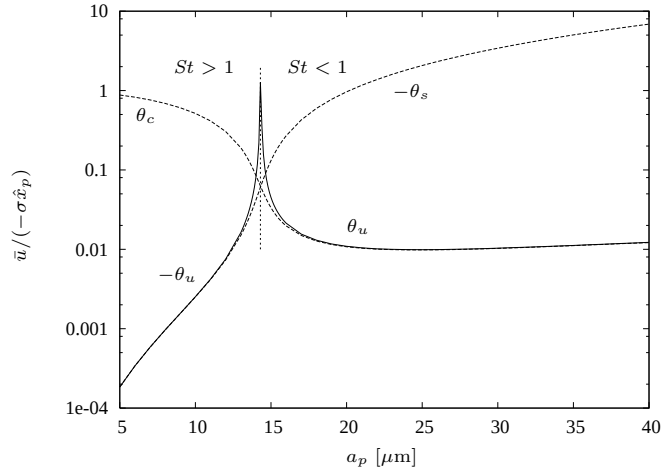

(b)

FIGURE 8.8. (a) Ratio θ between the average fluid velocity $\bar{u}$ and the particle velocity $-\sigma\hat{x}_p$ of the cupula mode and of the slow particle mode as a function of the particle radius a_p (n_p=10). Subfigure (b) shows the same data on a logarithmic scale together with the approximate expression θ_u.

we reduce our dynamical system to the two least stable modes. We can do this because all energy in the other modes dissipates faster than T_v after the head maneuver has ended. Therefore these higher modes are irrelevant to the slow dynamics of the positional nystagmus. (They are very relevant, however, during the per-rotatory phase as shown in Chapter 4.)

To formulate the reduced-order model we reduce the flow profile $\tilde{u}(\tilde{r},\tilde{t})$ to the bulk velocity $\bar{u}(\tilde{t})$. Likewise the k-th eigenfunction $(\hat{u}_k(\tilde{r}), -\sigma_k\hat{x}_{p,k})$ reduces to the vector $(\bar{u}_k, -\sigma_k\hat{x}_{p,k})$. This reduced system has the general solution

$$\begin{pmatrix} \bar{u} \\ \partial\tilde{x}_p/\partial\tilde{t} \end{pmatrix} = A_1 \begin{pmatrix} \bar{u}_s \\ -\sigma_s\hat{x}_{p,s} \end{pmatrix} e^{-\sigma_s\tilde{t}} + A_2 \begin{pmatrix} \bar{u}_c \\ -\sigma_c\hat{x}_{p,c} \end{pmatrix} e^{-\sigma_c\tilde{t}}. \tag{79}$$

If we know the initial conditions, i.e. the fluid velocity $\bar{u}_0$ and the particle velocity $\tilde{x}^{(1)}_{p,0}$ immediately after the head maneuver ($\tilde{t}=0$), we can determine the constants $A_{1,2}$.

We will see in the following that for appropriate choices of $A_{1,2}$ the reduced-order model (79) exhibits exactly the transient oscillations of the cupula that we observed in figure 7.3 and 8.2. Furthermore, we use the reduced order model (79) to derive explicit relations for the onset-latency T_L, the time to peak T_P and the maximum cupula deflection $V_{\max}$.

Numerical simulations (e.g. figure 8.2) show that typical head maneuvers always lead to co-flow situations at $\tilde{t}=0$, i.e. , the endolymph and the particles move in the same direction. From figure 8.7(b), however, we know that we always end up in a counter-flow configuration as $\tilde{t}\to\infty$. Therefore, either the fluid flow or the the particle velocity must change direction at a certain time $\tilde{t}>0$. If $A_1>0$ the cupula relaxes faster than the particles fall and, therefore, the fluid velocity will change sign at $\tilde{t}=T_P$ (figure 8.9). If $A_1<0$ the particles fall faster than the cupula relaxes. In that case, the particle velocity changes sign and there is no nystagmus. Since we were never able to observe the case $A_1<0$ in our numerical simulations of the full nonlinear system, we concentrate here on the case where $A_1>0$.

It is straightforward to show that

$$A_1 = \frac{\tilde{x}^{(1)}_{p,0}}{-\sigma_s\hat{x}_{p,s}}\,\frac{\theta_0-\theta_c}{\theta_s-\theta_c}, \qquad A_2 = -\frac{\tilde{x}^{(1)}_{p,0}}{-\sigma_c\hat{x}_{p,c}}\,\frac{\theta_0-\theta_s}{\theta_s-\theta_c}, \tag{80}$$

where $\theta_0 = \bar{u}_0/\tilde{x}^{(1)}_{p,0}$ is the ratio between the initial fluid and particle velocities. The values θ_c and θ_s were discussed in § 3. From figure 8.9 and the expression for A_1 it becomes clear that we get a positional nystagmus if and only if $\theta_0<\theta_c$. The time of peak nystagmus T_P corresponds to the time where $\bar{u}$ changes sign (cf. figure 8.9(a)). From (79) we can compute it as

$$T_P = \frac{1}{\sigma_c-\sigma_s}\ln\left[\frac{\theta_c(\theta_0-\theta_s)}{\theta_s(\theta_0-\theta_c)}\right]. \tag{81}$$

Note that T_P goes to infinity as $\theta_0 \to \theta_c$. Similarly we can find an expression for T_L. And the magnitude of the maximum cupula displacement is

$$V_{\max} = A_c \int_{T_P}^{\infty} \bar{u}(\tilde{t})\,\mathrm{d}\tilde{t}, \tag{82}$$

which gives

$$V_{\max} = A_c \tilde{x}_{p,0}^{(1)} \left(\frac{1}{\sigma_s} - \frac{1}{\sigma_c}\right) \theta_s \frac{\theta_0 - \theta_c}{\theta_s - \theta_c} \left[\frac{\theta_c(\theta_0 - \theta_s)}{\theta_s(\theta_0 - \theta_c)}\right]^{-\sigma_s/(\sigma_c - \sigma_s)}. \tag{83}$$

We can simplify these expressions by using our results from § 2 and figures 8.7(b) and 8.8:

$$\text{For } St > 1: \quad St \approx \frac{\sigma_c}{\sigma_s},\ |\theta_c| \gg |\theta_0|,\ |\theta_c| \gg |\theta_s|,\ \theta_s \approx \theta_u; \tag{84}$$

$$\text{For } St < 1: \quad St \approx \frac{\sigma_s}{\sigma_c},\ |\theta_s| \gg |\theta_0|,\ |\theta_s| \gg |\theta_c|,\ \theta_c \approx \theta_u. \tag{85}$$

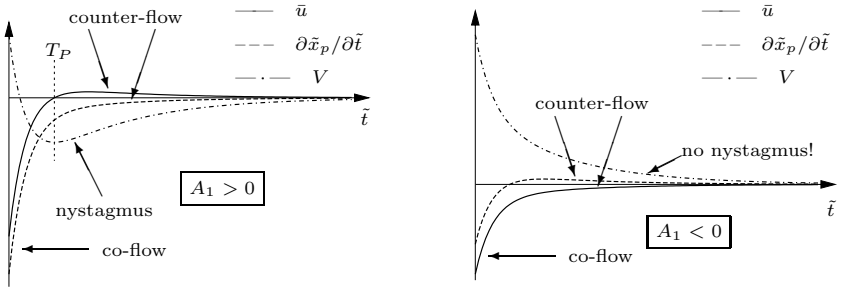

FIGURE 8.9. Two possible cases of transition from co-flow to counter-flow: (a) for $A_1 > 0$ the fluid velocity $\bar{u}$ changes sign at $\tilde{t} = T_p$ when the cupula displacement V reaches an extremum; (b) for $A_1 < 0$ the particle velocity $\partial\tilde{x}_p/\partial\tilde{t}$ changes sign, the fluid velocity and the cupula displacement decay monotonically.

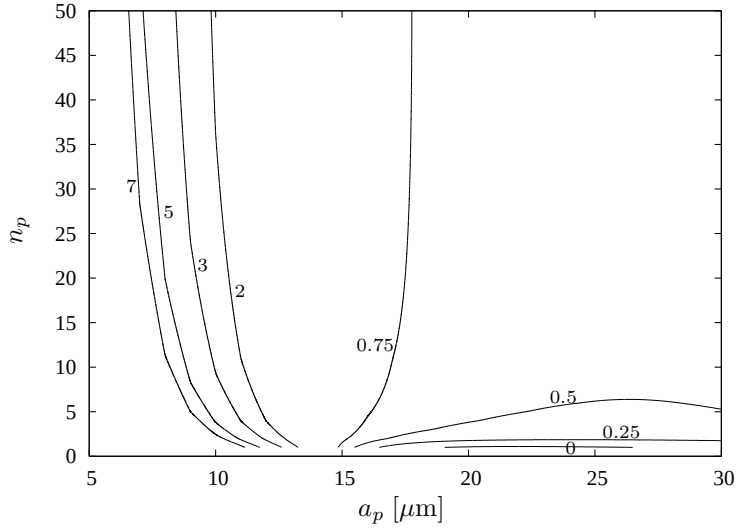

FIGURE 8.10. Value of $1 - \theta_0/\theta_u$ as a function of the particle size a_p and number n_p (values indicated at the contour lines).

This yields the following expressions for the onset-latency T_L, the time to peak T_P and the magnitude of the maximum cupula displacement $V_{\max}$

$$T_P = \frac{16}{\epsilon} \frac{St}{St-1} \ln\left(1 - \frac{\theta_0}{\theta_u}\right) \tag{86a}$$

$$T_P - T_L = \frac{16}{\epsilon} \frac{St}{St-1} \ln St \tag{86b}$$

$$V_{\max} = \frac{16}{\epsilon} \bar{u}_0 (St-1) \left(1 - \frac{\theta_0}{\theta_u}\right)^{-1/(St-1)} \tag{86c}$$

Typical values for $1 - \theta_0/\theta_u$ can be found in figure 8.10.

Although only approximately valid for the linearized equations, these explicit expressions give us a good idea of the relation between the physical and geometrical properties and the characteristic features of the positional nystagmus. For instance, we see that all characteristic values scale linearly with the cupula time constant $16/\epsilon$. We also find that the time from the onset of the nystagmus to its peak depends strongly on the Stokes number St, but that it is independent (in the spirit of a first approximation) of the head maneuver and the number of particles.

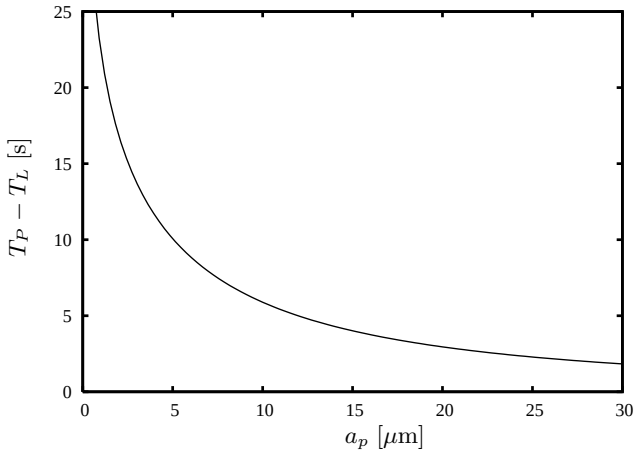

FIGURE 8.11. Estimate for the difference between time to peak T_P and onset-latency T_L as a function of the particle size according to the relation (86b) ($\epsilon = 0.09752$, $Fr^2 = 0.79052$).

The explicit expression for the time between the onset-latency and the peak nystagmus, Eq. (86b), stands out since it is relatively simple and might help to estimate the particle size directly from clinical data. It shows us that $T_P - T_L$ depends strongly on the Stokes number and that it is independent of the number of particles (keep in mind here that this relation is only an approximation). We have used this relation to plot $T_P - T_L$ as a function of the particle size (figure 8.11). A comparison of estimates from (86b) with numerical solutions of the full nonlinear governing equations (67) shows that figure 8.11 slightly underestimates the particle size. Nevertheless, it can serve as a valuable tool for diagnosing the particle size. The patient in figure 7.3, for example, exhibits a difference between T_P and T_L of approximately 8 s. With the help of figure 8.11 we can now estimate a particle size of 6 μm. We need to keep in mind, however, that it is not possible to determine the particle size and number conclusively from our model. This model does not consider, for example, non-spherical particles or even multiple particles of different sizes. At the current stage of abstraction and idealization our model is capable of revealing only the fundamental mechanisms and the basic relations between particle size and number and the positional nystagmus.

5. Non-normality of top-shelf vertigo

We have seen in this chapter that the dynamics of canalithiasis can be understood as the interplay of the first two eigenmodes of the linearized analytical model of canalithiasis. The cupula mode and the slow particle mode interact with

each other in a way that the potential energy of the elevated particles is exchanged with the deformation energy stored in the elastic cupula. This process leads to an apparent oscillation of the cupula even though the involved eigenvalues are purely real and do not predict any oscillating behaviour.

An energy analysis of the top-shelf vertigo dynamics shows that the kinetic energy in the system, i.e. the kinetic energy of the particles plus the kinetic energy of the fluid, has a local minimum approximately at the end of the head maneuver. After this minimum the kinetic energy increases transiently before it decays exponentially fast according to the asymptotic decay rates predicted by the eigenvalues.

This transient energy growth in a damped system can be related to the non-normality of the underlying dynamical system. This is a well known phenomenon from viscous shear flows which can occur whenever the eigenfunctions of the perturbed base flow are not orthogonal with respect to an appropriate energy metric (Trefethen *et al.*, 1993). For canalithiasis the non-orthogonality of the first two eigenmodes is obvious from their velocity profiles which are both nearly parabolic and can cancel each other (at $t = T_P$) such that the kinetic energy of the fluid is temporarily almost zero. In that sense, the symptoms of top-shelf vertigo can be understood as an expression of non-normality in biomechanics.

CHAPTER 9

In vitro model of an SCC with canalithiasis

Here, we present the design of a properly scaled experimental model[1] the validation of this model and we demonstrate its use for the study of SCC with canalithiasis. For simplicity, our SCC model is limited to the membranous duct of a single SCC and the utricle. The two other SCC, the saccule and the bony labyrinth are omitted.

1. Scaling of the experiment

To facilitate the handling of the experiment and to enable an accurate measurement of the cupula deflection and the particle trajectories, we scale the SCC by the factor $f > 1$ to a size of several centimeters. To maintain the subtle balance between the different physical processes in a SCC with canalithiasis, this geometrical scaling requires us to modify the other physical parameters as well. Because BPPV is a transient process it is sensible to keep the most relevant time scales of a SCC with canalithiasis constant: the viscous time scale T_v, the cupula time constant T_c and the particle settling time T_p. These values are discussed in the following and derived in more detail in Obrist & Hegemann (2008).

We have learned in Chapter 4 that there are two characteristic time scales which determine the dynamics in a healthy SCC: the viscous time scale and the cupula time constant. In a SCC with canalithiasis, there are two additional time scales which describe the dynamics of the particles: the particle relaxation time and the particle settling time. These two time scale correspond to the fast and the slow particle mode that we have found in Chapter 8. All time scales correspond to the inverse of the temporal eigenvalues of the SCC (cf. figure 8.7(a)).

The viscous time scale describes how fast viscous effects are able to relax a perturbed flow field in the slender duct of the SCC to an equilibrium state. It is given by

$$T_v = \frac{a^2}{\nu}, \tag{87}$$

where a is the radius of the slender duct of the SCC and ν is the kinematic viscosity of the endolymph. If we scale the geometry by a factor f, i.e. $a^+ =$

[1]This chapter is based on the article by Obrist *et al.* (2010) in the Journal of Biomechanics.

fa (where the superscript $^+$ indicates model parameters) we have to scale the kinematic viscosity ν by a factor of f^2 ($\nu^+ = f^2\nu$) to maintain T_v constant.

The particle settling time T_p describes a typical time scale for the settling of a canalith in a SCC under the influence of gravity. It corresponds to the inverse of the eigenvalue of the slow particle mode σ_s, Eq. (74), and is given by

$$T_p = \frac{9a^2R}{2ga_p^2(\rho_p/\rho - 1)T_v}, \tag{88}$$

where R is the major radius of the SCC, g is the gravitational acceleration, a_p is the canalith radius and ρ and ρ_p are the densities of the endolymph and the canaliths, respectively. After inserting the scaled values for $a^+ = fa$, $a_p^+ = fa_p$ and $R^+ = fR$ we find that the following relation must hold,

$$\frac{\rho_p^+}{\rho^+} = 1 + f\left(\frac{\rho_p}{\rho} - 1\right). \tag{89}$$

Finally, the cupula time constant describes how fast a deflected cupula relaxes in a SCC at rest. It is given by T_v/σ_c, cf. Eq. (27), which results in

$$T_c = \frac{8\rho\beta R}{\pi a^2 K T_v}, \tag{90}$$

where βR is the arc length of the slender duct and K describes the stiffness of the cupula. From this follows, that the scaled stiffness of the cupula K^+ should be

$$\frac{K^+}{K} = \frac{\rho^+}{f\rho}. \tag{91}$$

By this scaling, we ensure that the most relevant dynamical processes in the experiment run in real time. This means, for example, that a particle falls with an f times higher velocity through the model SCC (which is f times larger than a real SCC) such that it settles in the same time as canalith would settle in a real SCC.

This scaling maintains the dimensionless Reynolds and the Womersley numbers constant as well. The classical Stokes number $St_{\text{classical}}$, Eq. (75), as well as the Froude number Fr, Eq. (66), are different from a real SCC with canalithiasis. These dimensionless numbers have been sacrificed in favor of the geometric scaling because they are not of imminent relevance to BPPV. Their ratio $Fr^2/St_{\text{classical}}$, however, is maintained constant in our scaling because it relates directly to the particle settling time T_p.

Based on the available materials, we choose a scaling factor of $f = 4.4$. This allows us to use a multipurpose cutting oil for the endolymph with a specific density of $\rho^+ = 845\text{kg/m}^3$ and a kinematic viscosity of $\nu^+ = 19.5 \times 10^{-6}\text{m}^2/\text{s}$ (Ecocut 3010, Fuchs Petrolub AG, Mannheim, Germany). From Eq. (89) it follows that the model canaliths should have a density of $\rho_p^+ = 7200\text{kg/m}^3$. For the

TABLE 9.1. Parameters of the model SCC and an unscaled SCC.

description	symbol	model SCC	unscaled SCC
scaling factor	f	4.4	
major SCC radius	R	16mm	3.64mm
minor SCC radius	a	0.8mm	0.182mm
angle spanned by duct	β	250°	250° (6)
endolymph viscosity	ν	$19.5 \times 10^{-6}\mathrm{m}^2/\mathrm{s}$ (2)	$10^{-6}\mathrm{m}^2/\mathrm{s}$ (5)
endolymph density	ρ	$845\mathrm{kg}/\mathrm{m}^3$ (2)	$1000\mathrm{kg}/\mathrm{m}^3$ (5)
canalith radius	a_p	125μm (3)	28.4μm
canalith density	ρ_p	$7800\mathrm{kg}/\mathrm{m}^3$ (3)	$2700\mathrm{kg}/\mathrm{m}^3$ (5)
cupula stiffness	K	$1.7\mathrm{GPa}/\mathrm{m}^3$	$8.9\mathrm{GPa}/\mathrm{m}^3$
(achieved cupula stiffness (1))		$(4.0\mathrm{GPa}/\mathrm{m}^3)$ (4)	$(20.7\mathrm{GPa}/\mathrm{m}^3)$
viscous time scale	T_v	0.0328s	0.0331s
cupula time constant	T_c	4.24s	4.19s
(achieved cupula time constant (1))		(1.80s)	(1.80s)
particle settling time	T_p	1.11s	1.22s
particle relaxation time	T_r	1.64μs	0.48μs

(1) The cupula time constant achieved with the present experimental set-up is lower than the targeted time constant of 4.2s (Dai *et al.*, 1999).

(2) Ecocut 3010 at 24°C.

(3) steel micro-balls.

(4) Goodfellow elastomer film 50μm.

(5) Bronzino (1995).

(6) Van Buskirk *et al.* (1976)

present experiments, we use steel particles (micro-balls made of E52100 steel, MARTIN & C., Perosa Argentina, Italy) with a density of $\rho_p^+ = 7800\mathrm{kg}/\mathrm{m}^3$ and a radius of $a_p^+ = 125\mu$m which corresponds to canaliths with $a_p \approx 28\mu$m. We use a Silicone Elastomer Film with a thickness of 50μm by Goodfellow Cambridge Ltd. (Huntingdon, UK) for modeling the cupula. According to Eq. (91) the resulting cupula stiffness should be approximately $K^+ = 1.7\mathrm{GPa}/\mathrm{m}^3$. However, as we will report in § 3.1, the model cupula turns out to be stiffer such that the cupula time constant is lower than desired.

The scaled parameters are summarized in table 9.1 together with their unscaled values which compare reasonably well to human posterior SCC (Curthoys *et al.*, 1977*a*,*b*) and actual canaliths (Lim, 1984). The reduced particle and cupula time constants (due to the heavy particles and a stiff cupula) result in a model SCC which responds *faster* than a real SCC to symptomatic "head maneuvers".

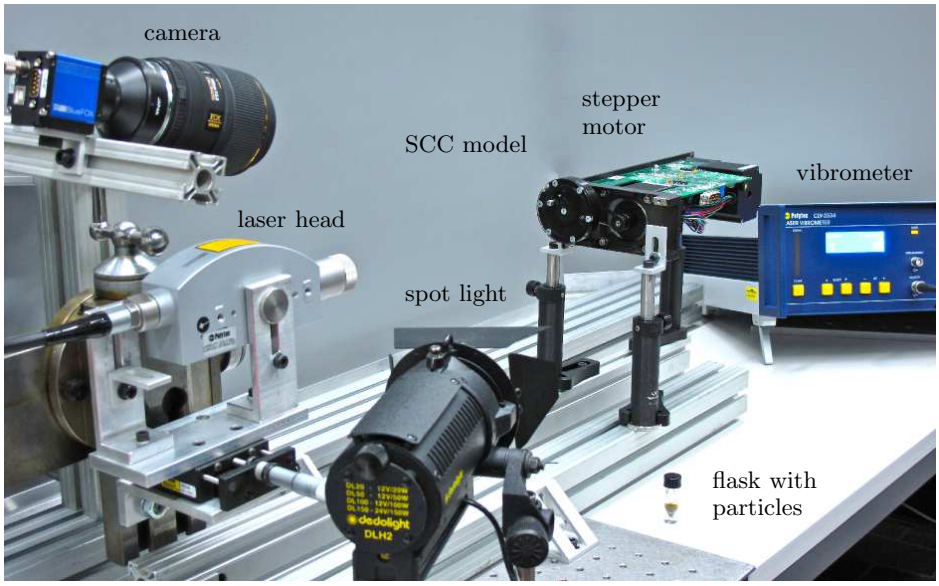

FIGURE 9.1. Complete experimental set-up.

2. Components of the experimental set-up

The complete experimental set-up (figure 9.1) consists of the scaled model of a single SCC, a stepper motor for rotating the SCC model, various measurement equipment and a personal computer for controlling the stepper motor, for data acquisition and for post-processing.

The centerpiece of our experiment is the scaled SCC (figure 9.2). It consists of an anodized aluminium base plate with a narrow circular groove of radius R^+ and a larger cavity. This cavity represents the utricle and the ampulla holding the cupula. The slender duct of the SCC is modeled by a transparent tube (inner radius a^+, length βR^+) which is inserted into the narrow groove. The thin elastic membrane which models the cupula is clamped between the two halves of a PVC insert fitting tightly in the cavity of the utricle (figure 9.2(b)). One side of this insert connects directly to the tube which represents the slender duct. The other side opens to the utricle. The cupula is rotated by 90° such that the deflection is normal to the plane of the SCC. This change in the geometry has a negligible effect on the dynamics of our model SCC because the inertial forces needed for the redirection of the endolymph by 90° are very small compared to the viscous

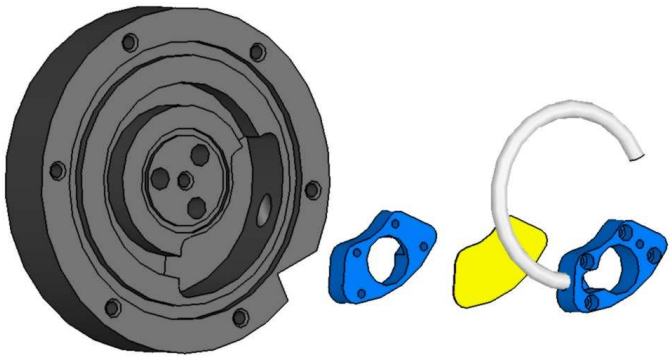

(a)

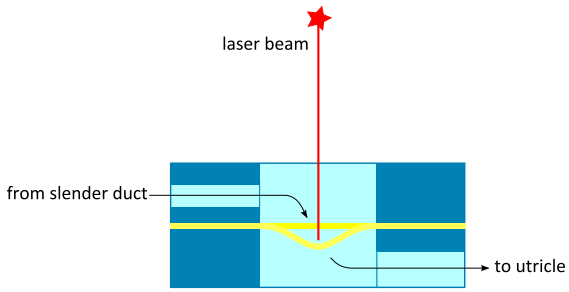

(b)

FIGURE 9.2. (a) CAD rendering of the complete SCC model and (b) a schematic cross-section of the cupula insert: aluminium base plate (black), latex tube (gray), insert (blue), cupula membrane (yellow). (Not shown: Plexiglas front plate, O-ring seal, venting hole, various bolts.)

forces in an SCC. The base plate is closed by a Plexiglas front plate with an O-ring seal. The system is filled with oil through a sealable hole in the utricle. A second sealable hole in the front plate is used for venting. The particles can be injected through the filling hole with a syringe.

The SCC model is mounted onto a computer-controlled stepper motor. The deflection y_c of the cupula (with respect to its relaxed position) is measured with a vibrometer (CLV-2534-4, Polytec GmbH, Waldbronn, Germany) which uses laser interferometry to measure the velocity $\mathrm{d}y_c/\mathrm{d}t$. The deflection y_c is obtained by numerical integration of the velocity signal. The laser beam is adjusted to the

center of the cupula membrane (at the end of the angular maneuver). To improve the reflection of the laser beam we have painted the center of the membrane with a silver glitter pen. During the rotation of the SCC the membrane deflection cannot be measured. Even if the laser beam followed the rotating SCC the vibrations of the system would be too large for an accurate measurement.

The experiments are captured with a video camera such that the canalith positions and velocities can be extracted from the video sequence with a particle tracking algorithm (Ohmi & Li, 2000; Marxen *et al.*, 2000). The light source which is required to get sufficient image quality for the particle tracking may heat the oil in the SCC and alter its viscosity. Therefore, the oil temperature has to be measured on a regular basis to adjust the results if necessary.

3. Experimental results

We use the SCC model for various experiments with and without particles where we mimic a typical head maneuver by rotating the SCC by 120° in T_M seconds. Unless noted otherwise, we use the maneuver define in Eq. (57) which lasts for $T_M = 3$s.

3.1. Calibration of the cupula time constant. Because the stiffness K^+ and the cupula time constant T_c cannot be determined exactly *a priori*, the SCC model (without particles) has to be calibrated to determine T_c. Ideally, T_c should not change between experiments. However, the cupula time constant is very sensitive to the clamping of the membrane in the insert (e.g. wrinkles and/or pre-straining) and we observe an aging effect (mechanical fatigue, creeping, diffusion of oil into the membrane, etc.) which tends to stiffen the cupula membrane. Therefore, the membrane has to be replaced regularly and T_c must be determined before every experiment.

The calibration test makes use of the well-known phenomenon (Grant & Van Buskirk, 1976; Highstein *et al.*, 2005) that a deflected cupula in a SCC at rest relaxes according to

$$y_c \sim e^{-t/T_c}. \tag{92}$$

This exponential decay can be observed, for instance, in figure 5.1(a) for $t > 0\,$s when the cupula returns from the overshoot to its relaxed position. The cupula time constant can be determined by fitting a curve with exponential decay to $y_c(t)$.

Figure 9.3 shows the results from several calibration tests. The initial deflection of the cupula was generated with standard rotational movements of the SCC. The curves follow Eq. (92) which indicates that the relation between the pressure across the cupula and its deflection is indeed linear. According to Dai *et al.* (1999) the cupula time constant for human posterior SCC is 4.2s. Recent results for oyster toadfish (Rabbitt *et al.*, 2009) suggest that the cupula time

constant may be as large as 13 to 104s (36s on average). Our model cupula leads to shorter time constants which are typically below 2s. The experiments shown in figure 9.3 and 10.1 had a time constant of $T_c \approx 1.8$s while the experiments in figure 9.4, 9.5 and 10.2 yielded $T_c \approx 0.75$s, 1.2s and 1.3s, respectively.

The difference in the cupula time constant between our experimental set-up and a real SCC is reflected in table 9.1 by the values in parentheses. The shorter time constant is the result of a stiffer cupula membrane. This difference could be eliminated by increasing the diameter of the model cupula. Despite the shorter time constant, we believe that the fundamental mechanisms of BPPV remain intact and that the differences are only of quantitative nature. Moreover, the present experimental set-up will allow us to quantify the effect of larger cupula time constants by increasing systematically the diameter of the model cupula.

3.2. Overshoot. During the acceleration of the head, the cupula is deflected by an amount approximately proportional to the angular velocity. In the deceleration phase, the cupula moves back by the same amount. But instead of returning exactly to its relaxed position, the cupula overshoots slightly the relaxed position (cf. figure 5.1a). This overshoot is related to the mechanical adaptation of the SCC which leads to a slow relaxation of the cupula already during the maneuver. This relaxation adds up with the deflection during the deceleration phase to an overshoot (we have used this overshoot to initialize the calibration tests). Note that this overshoot does not include the velocity storage mechanism (Raphan *et al.*, 1979; Squires *et al.*, 2004) which probably reduces the effect of the overshoot on the nystagmus.

Mathematically, the overshoot is described by the velocity error (53) in the analytical result for the cupula deflection. We compare this analytical prediction to our experiment in figure 9.4 where we used different maneuvers to trigger different cupula overshoots. These maneuvers complete the rotation of the SCC by 120° in $T_M = 0.5$s to 6s.

3.3. Canalithiasis. To study canalithiasis, we inject different numbers of particles (n_p) into the slender duct of the SCC. We let the particles settle to the lowest point in the system and then rotate the SCC according to Eq. (57). After the maneuver has ended, the particles fall through the SCC (or they slide and roll along its wall). They come to rest at the duct wall when the non-hydrodynamic forces between particles and wall (molecular forces as well as mechanical forces due to small geometrical imperfections and surface roughness) cancel the gravity force. During their settling the particles induce a flow in the direction of the falling particles which deflects the cupula in the direction of the head maneuver (leading to vertigo).

Figure 9.5 shows the deflection of the cupula for different numbers of particles. The curves for the cupula deflection have been averaged over several realizations

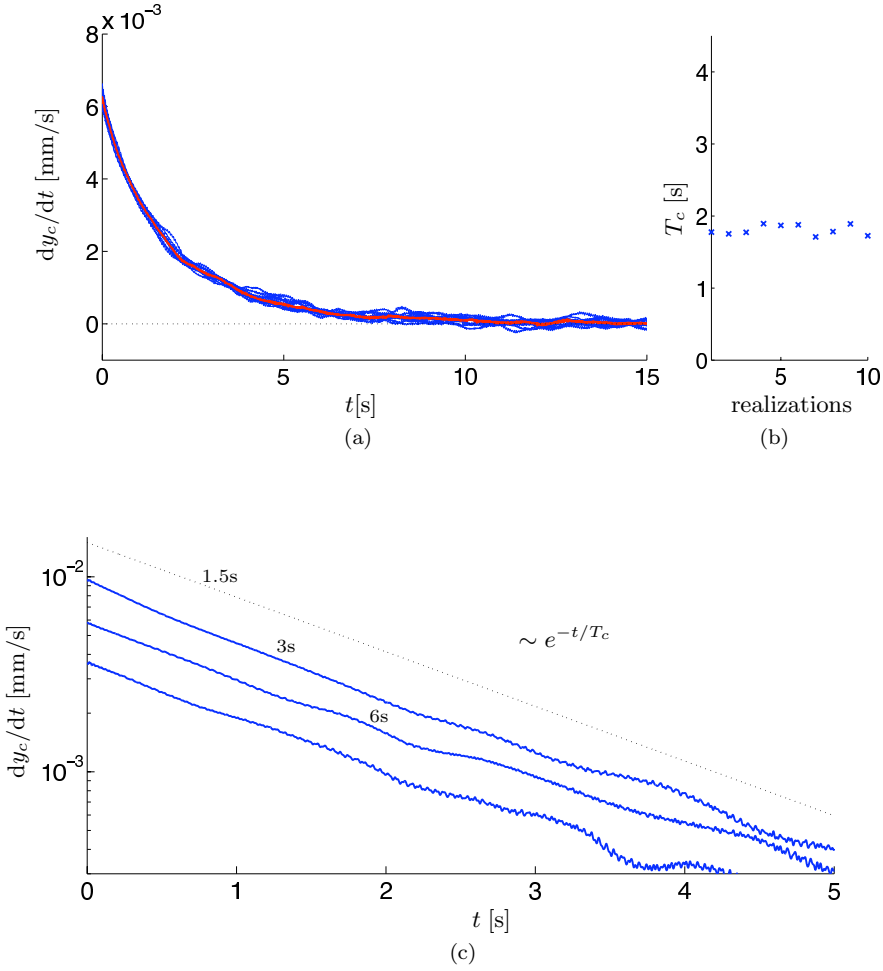

FIGURE 9.3. Calibration tests: (a) Cupula velocity for ten realizations (red curve: average value) of a calibration test initiated with the standard head maneuver Eq. (57). (b) Cupula time constants evaluated from the ten realizations. (c) Exponential decay of the cupula velocity ($T_c = 1.8$s) plotted on a logarithmic scale for maneuvers with $T_M = 1.5$s, 3s and 6s.

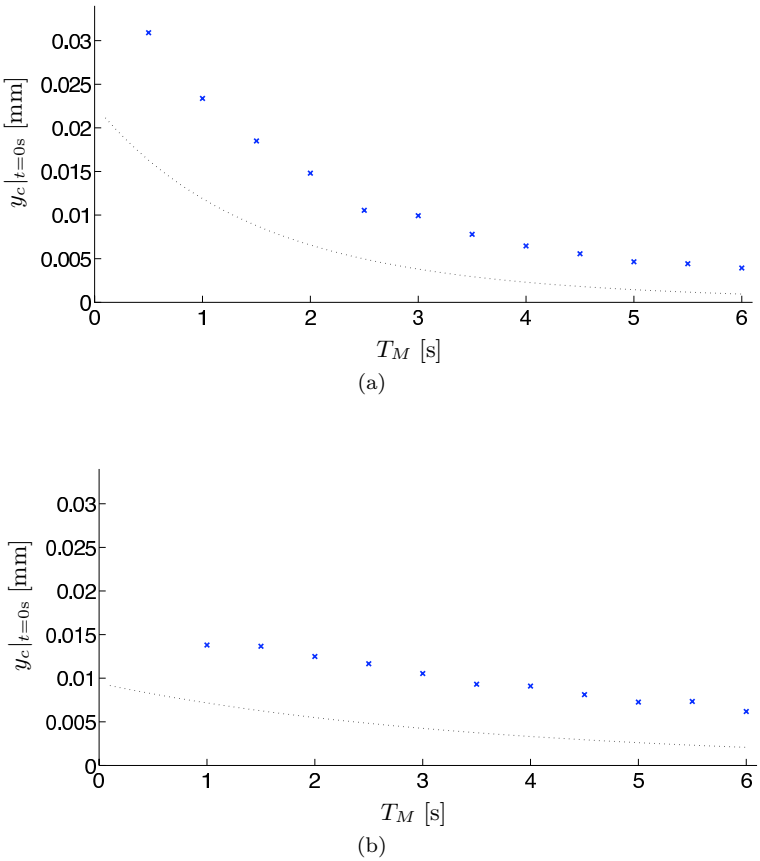

FIGURE 9.4. Overshoot at $t = 0$s for different maneuvers which complete the rotation by 120° in T_M seconds in a model SCC without particles with (a) $T_c \approx 0.75$s and (b) $T_c \approx 1.8$s. The dotted line indicates the theoretical predictions according to Eq. (53).

of the experiment. In particular, the experiments with large numbers of particles exhibit larger variations in $y_c(t)$ between different realizations (up to 20%). This is most likely related to irregular interactions between the falling particles. The effect of the particle interaction is emphasized by figure 9.3(b) which shows results where the particles were magnetized before the experiment such that they form

larger clusters while falling through the SCC. Apparently, this clustering leads to a stronger cupula deflection (see also Chapter 11 for a further discussion of this phenomenon).

In the sense of a 'null experiment', we have tested configurations in which all particles are located inside the utricle. This corresponds to a BPPV patient who has been treated with a specific head maneuver in order to move the canaliths out of the slender duct into the utricle. As expected, these experiments do not exhibit any pathological deflection of the cupula.

4. Discussion of the results

The experimental results presented in section 3 compare well with established results on the behavior of healthy SCC (Damiano & Rabbitt, 1996; Van Buskirk *et al.*, 1976; Obrist, 2008) and of SCC with canalithiasis (e.g. Aw *et al.*, 2005).

The experiments from sections 3.1 and 3.2 validate the experimental set-up. The results presented in figure 9.3 show that the cupula relaxation in our model SCC without particles adheres to an exponential decay. This phenomenon is directly related to the post-rotatory overshoots compared in figure 9.4. In accordance with our results, this data shows also a tendency toward smaller overshoots for larger cupula time constants.

The theoretical and experimental results in figure 9.4 show both the same general trends but differ quantitatively. Assuming that the membrane in the SCC model deflects like a circular clamped plate, the volumetric displacement V is proportional to the displacement y_c (because the displacements are small with respect to the membrane diameter). If, however, the deflected cupula is slightly corrugated and/or the vibrometer laser beam is not exactly centered, we can easily imagine that the proportionality factor between V and y_c changes substantially.

The canalithiasis experiments in § 3.3 confirm the fundamental mechanism of BPPV as described by various authors (House & Honrubia, 2003; Rajguru *et al.*, 2004; Obrist & Hegemann, 2008). We can see that the onset-latency, i.e. the time from the end of the maneuver to the onset of the positional nystagmus, is directly related to the cupular overshoot. In configurations with many particles, the flow induced by the settling particles can be so strong that there is no overshoot and, thus, no onset-latency. Such cases have also been found in clinical tests by Aw *et al.* (2005). Moreover, the landmarks of the cupula displacements in figure 9.5 (such as the onset-latency, the time to the peak deflection, etc.) show a remarkable agreement with clinical data by Aw *et al.* (2005) (especially for posterior SCC) if we factor in that our model reacts faster due to the short cupula time constant. The quantitative differences to the numerical results in Chapter 8 can be mainly attributed to the idealized particle description of the analytic model.

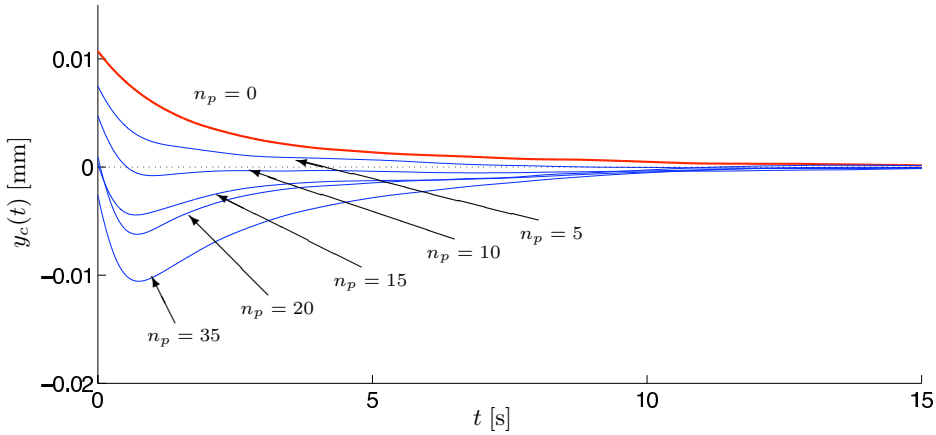

(a)

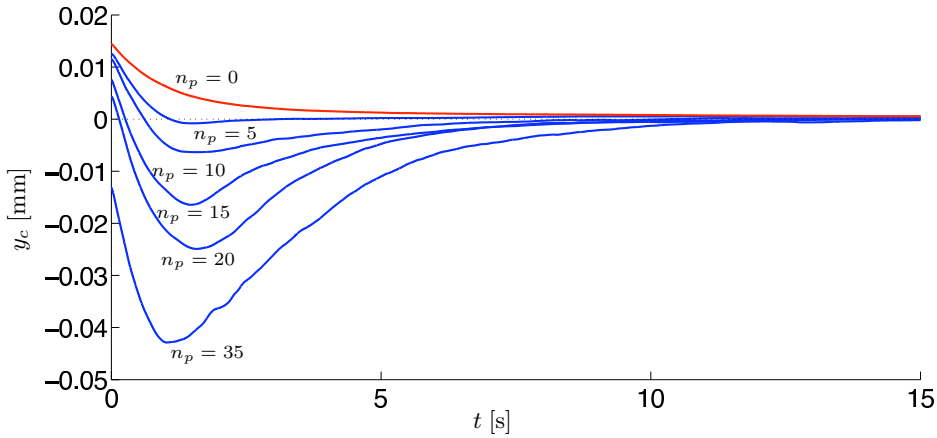

(b)

FIGURE 9.5. Cupula displacement y_c for canalithiasis experiments with different numbers n_p of particles and different cupula time constants: (a) $T_c \approx 1.8$s and (b) $T_c \approx 1.2$s. The curves are averages of multiple realizations of the experiments. The particles in (b) are slightly magnetized such that they form larger clusters of particles.

We will see in the following chapter (e.g. figure 10.2) that the multi-particle dynamics is more complex than the model used in Chapter 8. Furthermore, the reduced particle and cupula time constants lead to a faster "response" of our model, i.e. the beginning of the pathological cupula deflection and the time of the peak deflection occur earlier than in a real SCC. Nevertheless, the experimental results confirm that the pathological deflection of the cupula increases with the number of particles.

The present experimental set-up can also be used to study various phenomena such as the effect of polydisperse and/or non-spherical particles on the cupula deflection. It is expected that the nonlinear particle interaction leads to large variations in the cupula deflection patterns.

CHAPTER 10

Particle trajectories in SCC

We have seen in the previous chapters that the dynamics of the canaliths (particles within the SCC) is dominating the symptoms of top-shelf vertigo.

Depending on the initial position, number and size of the canaliths their trajectories within the slender duct of the SCC can differ substantially. Figure 10.1 shows different realizations of the in vitro experiment discussed in Chapter 9 for single particle trajectories whereas figure 10.2 gives an impression of the complex particle dynamics in a configuration with multiple particles.

We see that the canaliths can either remain at the outer wall of the SCC during the whole maneuver, detach from this wall for a short period, or even temporarily touch the inner wall of the SCC. These particle trajectories have a direct impact on the cupula displacement (Obrist *et al.*, 2008). This phenomenon will be studied in the following section.

1. Two-dimensional particle model

In our analytical model of canalithiasis (Chapter 8), we have only used the one-dimensional particle model first proposed by House & Honrubia (2003). It is not clear a priori whether this is indeed an appropriate model, whether we might be missing some fundamental effects or, even worse, whether this model yields misleading results. Therefore, we compare our results to results obtained with the two-dimensional particle model by Squires *et al.*.

To this end, we add an equation for the radial particle motion to the governing equations (67). The drag forces in both particle equations are adjusted to reflect the influence of the pipe walls (Bungay & Brenner, 1973; Happel & Brenner, 1973; Squires *et al.*, 2004). We modify the pressure drop due to the moving particles according to Squires *et al.*. Details can be found in the appendix of Squires *et al.* (2004) and references therein. To be consistent with Squires *et al.*, we also introduce a lubrication gap of 1μm. In addition, we include a centrifugal force, $m_p R\dot{\alpha}^2$, to reflect the influence of the rotating reference frame. The resulting equations for the two-dimensional model are solved within the simulation framework described in Chapter 8.

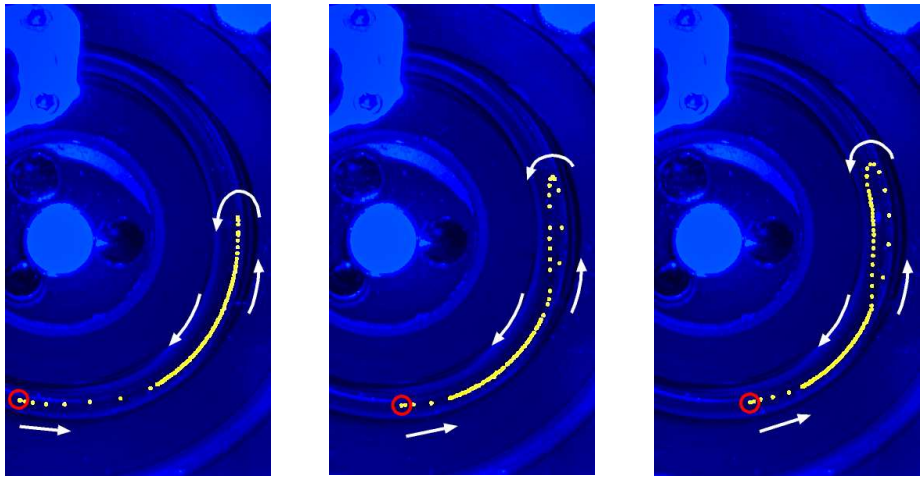

(a) (b) (c)

FIGURE 10.1. Particle trajectories for head movements with $n_p = 1$ (red circle indicates the starting position). (a) The particle slides along the outer wall (never detaches from the wall), (b) the particle falls through the SCC until it hits the outer wall, (c) the particle detaches from the outer wall, hits the inner SCC wall, detaches a second time, falls onto the outer SCC wall and slides toward the lowest point of the SCC ($T_c \approx 1.8$s). Reprinted from Obrist *et al.* (2010).

Figure 10.3 shows the particle trajectories obtained with the two-dimensional model during and after the head maneuver for different particle sizes. During most of the head maneuver the particles remain in contact (apart from the lubrication gap) with the outer wall. Smaller particles remain at the wall even beyond 90° due to the centrifugal forces. Only when the head maneuver comes to an end the particles start falling down in a more or less straight line until they hit either the inner or the outer wall of the SCC. The very small particles touch the inner wall first and detach a second time before they hit the outer wall. The situation is different for large particles. During the head maneuver they slide down along the wall so much that they never detach. The one-dimensional model neglects these effects.

Figure 10.4 compares the axial particle velocities for the three cases from figure 10.3. The rapid changes in the axial velocities in the two-dimensional model correspond to the instants when the particles either hit or detach from the wall. In

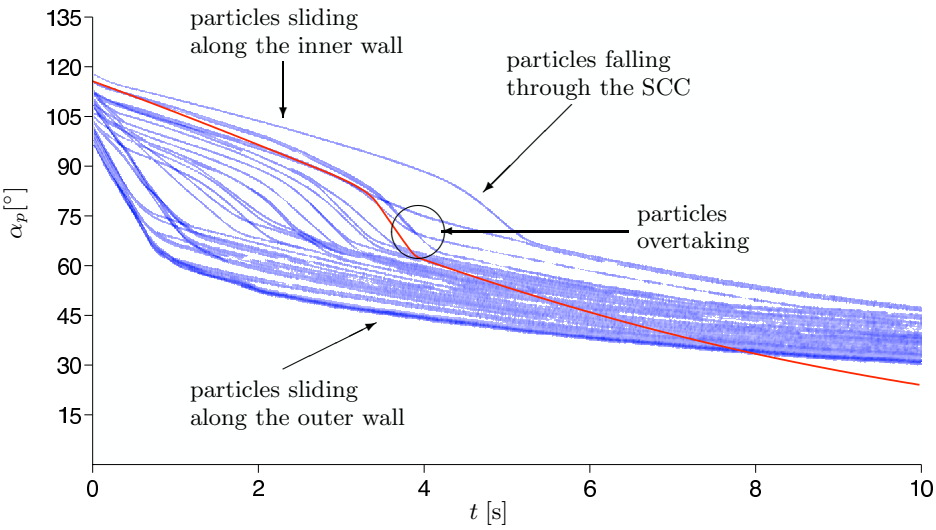

FIGURE 10.2. Particle trajectories for head movements with $n_p = 35$ (the azimuthal angle α_p of the particle positions as a function of time) in a model SCC with ($T_c \approx 1.3$s.). The particles follow different trajectories (some falling through the slender duct, some sliding first along the inner wall). Furthermore, some particles form clusters or fall at different velocities (indicated by the different slopes of the individual curves). The red line shows the predicted particle trajectory according to the analytical model by Obrist & Hegemann (2008). Reprinted from Obrist *et al.* (2010).

general, the axial particle velocity is smaller with the two-dimensional model. But although the two-dimensional model reveals more detail in the particle dynamics, the two models describe the same principal behaviour and give similar results.

2. Effect of particle trajectories on cupula displacement

Finally, we compare the cupula displacements, the key indicator for the perceived angular velocity (figure 10.5). Again, the results differ somewhat quantitatively for the two particle models, but the basic character of the results remains the same as for the one-dimensional particle model: a trend toward shorter onset-latency and stronger nystagmus for larger particles, no latency for very large particles, etc. . Apparently, we are not missing any basic feature of the positional

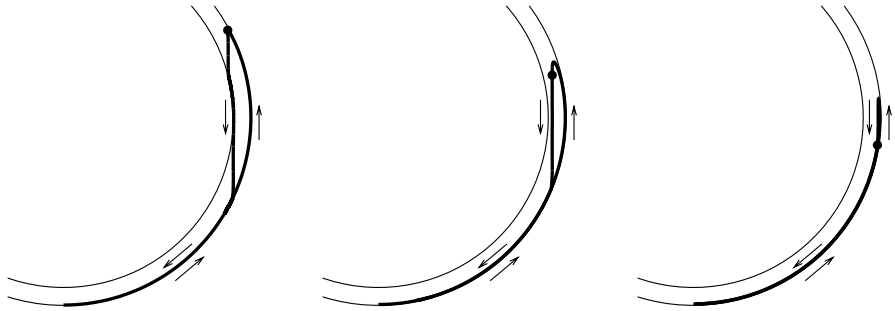

(a) (b) (c)

FIGURE 10.3. Particle trajectories for $n_p = 5$ and (a) $a_p = 5\mu$m, (b) 15μm, (c) 25μm (• indicates the location of the particles at the end of the head maneuver). Reprinted from Obrist & Hegemann (2008).

nystagmus if we use the one-dimensional model. We conclude that the two different particle models yield (in the spirit of a first approximation) equivalent results. The following observations can help explain this somewhat surprising fact:

(i) The smaller particles spend a certain amount of time close to the centerline of the canal. During this time (coincidental with the build-up of the positional nystagmus) the pressure drop in the two-dimensional model is larger than in the one-dimensional model. While the particles are closer to the wall the situation is reversed. On average, the two effects tend to cancel.
(ii) Because of their size (relative to the canal) the large particles induce a pressure drop which is large enough to cause a positional nystagmus even while they are only sliding along the wall. This is consistent with the experiment of Rajguru & Rabbitt (2007). It has to be noted, however, that our results are very sensitive to the choice of the lubrication gap. This point requires further investigation.
(iii) Mathematically speaking the cupula has the role of a temporal integrator which tends to smooth differences in the particle dynamics.

The two-dimensional particle model adds an additional level of detail to the results which is valuable for the study of the more intricate features of canalithiasis (e.g. fatigue of top-shelf vertigo, Chapter 11). Nevertheless, the one-dimensional

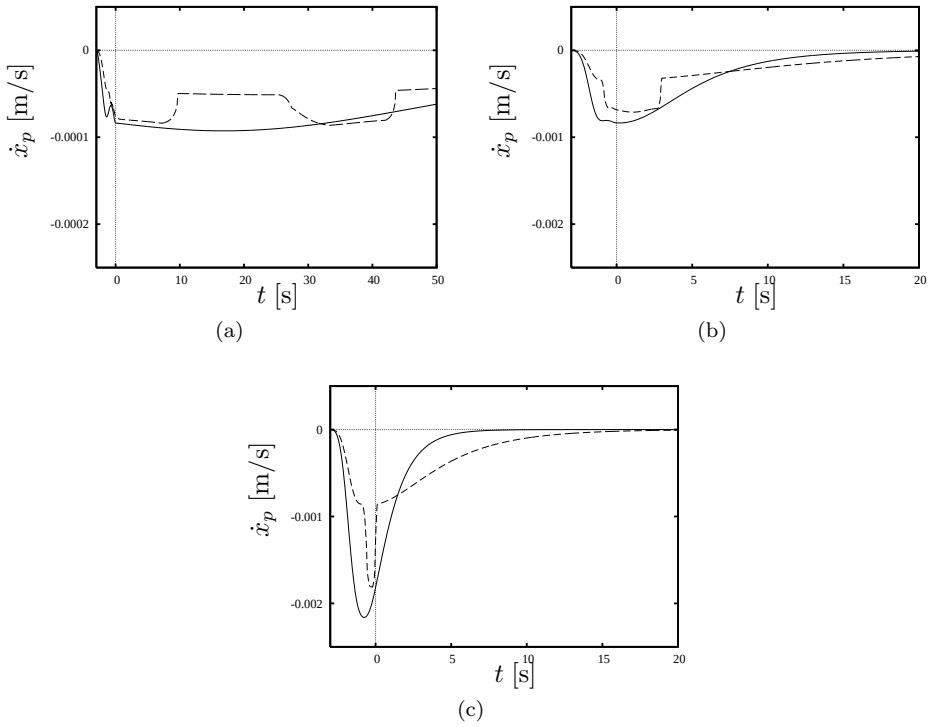

FIGURE 10.4. Axial particle velocity $\dot{x}_p(t)$ for $n_p = 5$ and (a) $a_p = 5\mu$m, (b) 15μm, (c) 25μm (—— one-dimensional particle model; – – – two-dimensional particle model; note the different ranges for (a)). Reprinted from Obrist & Hegemann (2008).

model appears to be sufficient for the study of the principal features of canalithiasis.

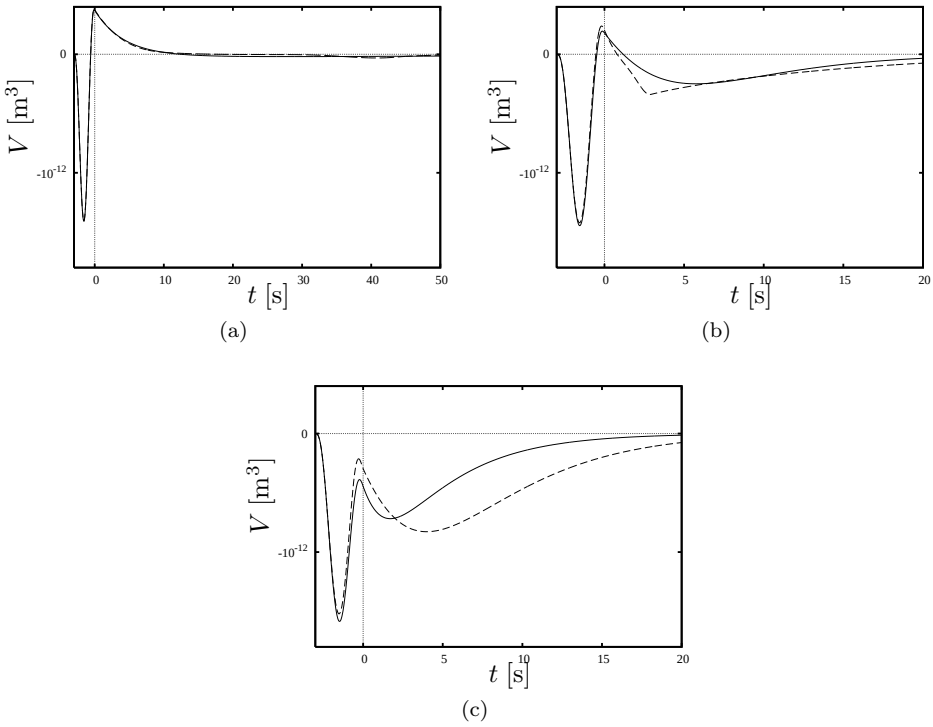

FIGURE 10.5. Cupula displacement $V(t)$ for $n_p = 5$ and (a) $a_p = 5\mu$m, (b) 15μm, (c) 25μm (—— one-dimensional particle model; – – – two-dimensional particle model). Reprinted from Obrist & Hegemann (2008).

CHAPTER 11

Fatigue of top-shelf vertigo

It has been observed in clinical testing that the top-shelf vertigo symptoms become weaker when the symptomatic maneuver is repeated. This fatigue of BPPV may be related to the clustering of canaliths, i.e. it is hypothesized (e.g. Welling *et al.*, 1997) that the canaliths are initially clustered (cf. figure 7.1a). During repeated maneuvers these clusters may fall apart leading to weaker induced flow fields and smaller cupula displacements. This hypothesis is not supported by state-of-the-art theoretical models (Rajguru *et al.*, 2004; Squires *et al.*, 2004; Obrist & Hegemann, 2008) which predict a weakened cupula displacement for clustered canaliths (cf. figure 8.6). In the following we will test this hypothesis on our in vitro model of an SCC (Chapter 9).

1. Experiments with clustered particles

We perform experiments with different numbers of canaliths. The measured cupula displacements are averaged over ten instances of the same experiment. The whole series of experiments is repeated with magnetized particles. This magnetization of the steel spheres leads to larger lumps of particles which simulates canalith clustering.

The resulting cupula displacements for the different experiments were already displayed in figure 9.5. Figure 11.1 summarizes these results and shows the maximum cupula displacements for separated and clustered canaliths as a function of the number of canaliths. The different nature of the trajectories for the clustered and separated particles is illustrated in figure 11.2 [1].

2. Potential causes for fatigue

These experimental results suggest that canalith clustering leads to a cupula displacement which is approximately four times larger than for SCC with separated canaliths. However, the cupula time constant in the clustered experiments is smaller ($T_c = 1.2$s) than the time constant for the separated experiments ($T_c = 1.8$s). Therefore, the presented results have to be taken with caution.

[1] pictures by Dominique Kronenberg, Master thesis FS 2009, Institute of Fluid Dynamics, ETH Zurich.

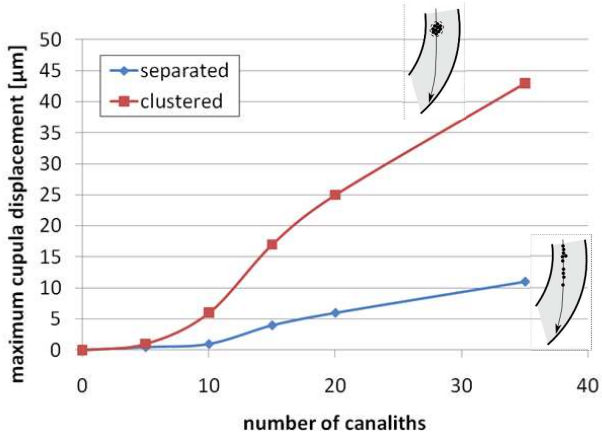

FIGURE 11.1. Maximum cupula displacements during the positional nystagmus for separated and clustered canaliths.

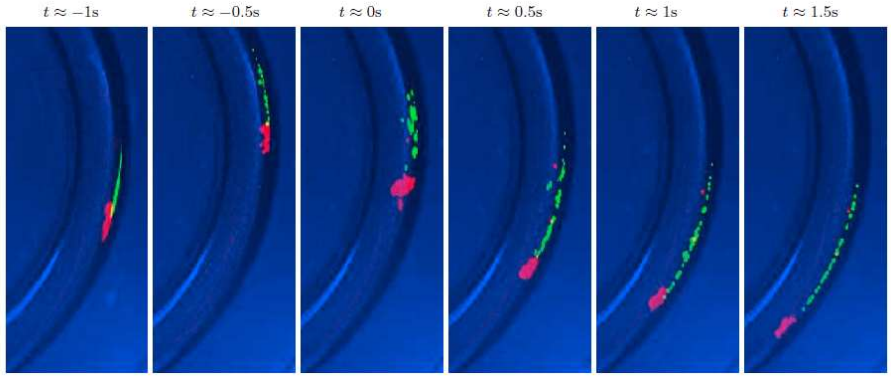

FIGURE 11.2. Snapshots of the particle positions in experiments with $n_p = 35$ particles (red: magnetized; green: non-magnetized) using the head maneuver defined in Eq. (57) running from $t = -3$ s to 0 s.

More recent studies[2] with matched cupula stiffness indicate that the effect of clustering is weaker than figure 11.1 suggests.

There are also strong indications that the initial position of the particles plays a role in the fatigue of BPPV. Figure 10.1, for instance, shows that even

[2]Aurelio Schmid, Master thesis FS 2011, Institute of Fluid Dynamics, ETH Zurich

slight perturbations of the initial position of the particles can lead to significantly different particle trajectories and thereby to stronger or weaker cupula deflections (Chapter 10). Furthermore, wall friction and/or geometrical imperfections can cause the particles to stop before they reach the lowest position in the canal. Therefore, the initial position of the particles for following maneuvers (in the opposite direction) corresponds to the case shown in figure 10.1(a) which leads to a weaker cupula deflection than in figure 10.1(b).

We conclude that both mechanisms—*canalith clustering* as well as the *initial canalith position*—can lead to a fatigue of BPPV symptoms. It is not unlikely that a combination of both mechanisms are involved in the clinically observed phenomenon of BPPV fatigue.

Part 2

The Cochlea

CHAPTER 12

Introduction to cochlear mechanics

Next to the semicircular canals and the otolith organs we find the cochlea which hosts the hearing sensorium. Although all systems share the same fluid spaces and exhibit some anatomical similarities, we will find that cochlear mechanics differs dramatically from the mechanics of the vestibular system.

The vibrations of the oval window lead to a pulsatile flow in the cochlea (figure 1.5). The generated flow field interacts with the compliant membranes inside the cochlea leading to traveling waves in the fluid and on the basilar membrane (BM) along the axis of the cochlea. The graded mechanical stiffness of the BM (stiffer at the base of the cochlea and more supple toward the apex) leads to localized peaks in the amplitudes of these traveling waves due to resonance phenomena. This basic mechanism of signal transport in the cochlea has already been discovered by Békésy almost a century ago (von Békésy, 1960). In principle, it is equivalent to the wave propagation mechanism in a fluid filled pipe with compliant walls.

The locations of the peaks of the traveling waves ('characteristic places') depend on the frequency of the acoustic signal. This resonance phenomenon relates each frequency of the acoustic signal to a specific axial location along the cochlea. This frequency mapping is known as the 'place principle'.

The displacement of the BM due to the traveling waves stimulates the organ of Corti (OC). The three rows of outer hair cells (OHC) in the OC (figure 1.7) are 'motors' which can amplify the BM displacements. This so-called 'active process' sharpens the tuning of the cochlea which is necessary because the passive resonance of the traveling wave yields an insufficiently distinct signal. The inner hair cells (IHC) are a fourth row of hair cells. They have no active motor function but are stimulated by the amplified oscillations of the BM and the other structures in the OC. The IHC excitation finally leads to afferent nerve signals and thereby to the perception of sound. (The acronyms are summarized in table 1.1.)

The exact role of the active processes and, in particular, their effect on the cochlear mechanics is not yet understood in its full complexity (Nobili *et al.*, 1998). It is clear, however, that the active processes are more than a simple second stage of filters after the traveling wave phenomenon. The active processes within the OC interact closely with the surrounding structures and fluids, i.e.

besides the traveling waves triggering the active processes within the OC, the micromechanics in the OC has an influence on the traveling waves as well.

Next to the nonlinear active processes in the OHC, the phenomenon of acoustic streaming (Lighthill, 1992) is suspected to be of relevance to cochlear mechanics. It describes a weakly nonlinear process which generates a steady streaming through the interaction of weak linear waves. Acoustic streaming in the cochlea will be discussed in Chapter 16.

Apart from the active OHC and acoustic streaming, there exists a third mechanism which is often perceived as nonlinear although it is linear by nature. This mechanism can lead to transient phenomena beyond the classical concept of resonance. It is related to the grading of the mechanical properties along the axis of the cochlea which results in non-normal differential operators for the cochlear dynamics, This phenomenon will be touched in Chapter 13.

The crux in cochlear mechanics is the large range of scales and physical phenomena which operate simultaneously and interactively. The tight interaction between the different components of the cochlea is illustrated schematically in figure 12.1. It should become clear from this figure that fluids in the cochlea (in blue) play the role of a mediator between the different scales and components of the cochlea. Hydrodynamic phenomena are able to transmit information between large distances and/or to translate it between different physical sub-systems. The nature of these transmissions is different at different places in the cochlea: ranging from a wave guide mediating between the oval window and the basilar membrane, all the way to (suspected) acoustic streaming phenomena in the microscale space within the OC.

It is clear that the mechanisms governing our hearing organ can only be understood if we study it as a complete system reflecting this tight interaction between the different scales, rather than just studying the different functional units separately.

1. Open questions in cochlear mechanics

Although the basic principles of cochlear mechanics are understood, there are many phenomena and mechanisms which remain unknown or only poorly understood. In the following, we list some pertinent open questions which are strongly related to the hydrodynamics within the cochlea.

(i) **How are the IHC stimulated within the OC?**
The intricate dynamics within the OC are suspected to be much more complex than it might appear at first glance. The exact mechanism of excitation of the IHC, for instance, is not known. Next to the anatomical uncertainty whether the IHCs are connected to the TM (e.g. Lim, 1980), it is also unclear whether the flow in the subtectorial space (fluid filled space beneath the TM) is purely oscillatory or whether this

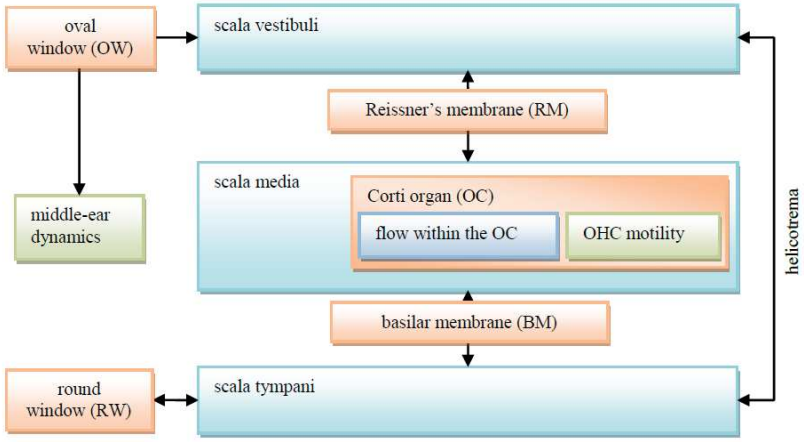

FIGURE 12.1. Schematic of the interaction between different components and processes in the cochlea (fluid flows in blue; structures in amber; other processes in green).

flow has a non-zero average (due to acoustic streaming as suspected by Lighthill, 1992) which would tilt the IHC stereocilia (hair bundles at the end of the hair cells) predominantly in one direction during the stimulation.

(ii) **How is the acoustic signal transmitted along the axis of the cochlea?**
The classical theory of traveling waves remains quite popular in cochlear modeling. It is an inviscid one-dimensional long-wave theory. Its weaknesses have been known for a long time and some improvements have been proposed (e.g. the two-dimensional inviscid theory by Lesser & Berkley (1972). Nevertheless, the traveling-wave theory remains sketchy especially because the viscosity is still neglected. The traveling wave models have to be questioned even more since the discovery of the active processes in the cochlea, because the OHC motility leads to sharp axial gradients in the BM displacement which will render the flow fields much more complex than assumed so far. Moreover, there exist so-called 'reverse traveling waves' which are responsible for a phenomenon known as otoacoustic emissions (OAE; He *et al.*, 2008). In the context of signal transmission in the cochlea, De Boer & Nuttall (2009) speak also of 'hidden waves' which indicates that there exist other signaling mechanisms beyond the (forward) traveling waves in

the perilymphatic spaces. Some of these alternative signaling mechanisms can be explained by anatomical details (e.g. OHC tilting; Lim & Steele, 2002), others might simply be 'hidden' in the fluid-structure interaction of the cochlea.

(iii) **How are vibrations at the oval window (or alternative actuators) transduced into a perilymphatic flow?**
At the oval window, it is not clear how displacements of the membrane translate into a flow of the perilymph and subsequently into a BM stimulation, e.g. for cochlear stimulation due to a rocking motion of the stapes (Sim *et al.*, 2010). Recent studies by Pozrikidis (2007) and the author's group (Edom *et al.*, 2010*a*) used detailed flow simulations to study this issue at least in a local context. A conclusive discussion, however, would require a global model of the complete cochlea. The interest in the transduction of oval window displacement into traveling waves has become more prominent recently with the advent of new generations of hearing aids which stimulate the cochlea mechanically with a small piston at the oval window (DACS devices; Mojallal *et al.*, 2007) or with micro-actuators directly immersed into the perilymph. Most current models of cochlear fluid dynamics are far from being able to answer these questions.

(iv) **What is the effect of a local flow inside the OC on global cochlear mechanics?**
Lim & Li (2007) pointed out the complexity of the viscous flow inside the OC. Most global cochlear models available today are of insufficient detail for studying the subtle interactions between the flow within the OC and the large-scale dynamics of the surrounding lymph. The oscillatory flow in the tunnel of Corti in the vicinity of the characteristic place observed by Karavitaki & Mountain (2007), for instance, is a good example demonstrating this need for a detailed global cochlear model. This oscillatory flow might be a result of the OHC motility and will alter the local mechanical properties of the BM. Obviously, this would have a direct impact on the global traveling waves which again will influence the BM stimulation at the characteristic place. Such subtle interactions between local and global mechanisms can only be understood with the help of a global cochlear model which includes a wide range of scales and phenomena.

In order to be able to answer these open questions, several challenges in cochlear modeling have to be overcome. One of the principal problems is the lack of a good access to a living cochlea. In vivo studies are extremely difficult because of (a) the fact that the cochlea is a hidden cavity carved in solid bone (temporal bone), (b) the small size of the cochlea, and (c) the even smaller scales of the

oscillatory displacements of the sensory membranes. It is almost impossible to measure membrane displacements or flow fields within the organ of Corti without disturbing the dynamics in the cochlea.

2. State-of-the-art in global cochlear modeling

2.1. Passive cochlear models. Early global models described passive cochlear mechanics (because the OHC motility was not yet discovered) and were mostly limited to one- or two-dimensional idealized geometries ('box model'). Out of the many cochlear models (see Inselberg, 1978 and, more recently, De Boer, 1996 for an overview) the so-called *transmission-line model* stands out as a simple yet illustrative model. This one-dimensional inviscid linear description of cochlear mechanics is usually attributed to Peterson & Bogert (1950) (actually, their model also considered acoustic waves within the perilymph itself). Although it has been shown many times that the transmission-line model fails to describe the more subtle aspects of cochlear dynamics correctly, it remains in use to this day because it reproduces basic phenomena quite well (e.g. the traveling waves) and is amenable to analytical study (e.g. Xin, 2004; Obrist & Schmid, 2008).

Apart from the passive and linear description of the BM, the main deficiency of the transmission-line model is the restriction to one-dimensional flow and long wave lengths as well as the lack of viscosity in the fluid. Lesser & Berkley (1972) showed that the cochlear flow is (at least) two-dimensional. They described the flow field as a potential flow which is free of the restriction to long wave lengths. However, their description satisfies only slip boundary conditions at the walls and still neglects viscosity. Another two-dimensional model based on a finite-difference discretization of the flow field was proposed a few years later by Allen (1978). Viscous effects were included in an extension of the transmission-line model by Leveque *et al.* (1988). This extended model remains (technically) one-dimensional but includes the effect of the Stokes boundary layers which lead to local viscous dissipation that is out of phase with the bulk flow. Beyer (1992) presented probably the first two-dimensional transient simulation of the viscous flow in the cochlea. The multi-compartment model by Chadwick *et al.* (1996) introduces more geometrical detail by including some functional components of the OC. Two- and three-dimensional flow in the cochlea was discussed from the theoretical point of view in several papers by Lighthill (e.g. Lighthill, 1981*b*,*a*). In a later paper, he put the main focus on *acoustic streaming* in the cochlea. Acoustic streaming describes a mean flow generated by nonlinear interactions between linear waves (Lighthill, 1978). Its possible relevance to cochlear dynamics has been pointed out by several authors (e.g. Kern, 2003). To our best knowledge, such nonlinear effects in the cochlea (*nonlinear* refers here to fluid motions and not to the description of the BM) have not been studied further.

Several studies suggest that the flow in the cochlea is three-dimensional (e.g. Taber & Steele, 1979; Olson, 1998; Parthasarathi *et al.*, 2000; White & Grosh, 2005; Cheng *et al.*, 2008). Figure 5 in White & Grosh (2005), for instance, indicates that there are transversal variations in the BM deflection which is inherently tied to three-dimensional flow structures. Most models of the cochlea neglect the coiling of the cochlea because it is commonly believed that the coiling of the cochlea does not have a significant effect on cochlear mechanics. Only recently, a study by Manoussaki & Chadwick (2000) (and also by Cai *et al.*, 2005; Manoussaki *et al.*, 2006, 2008) indicated that the coiling may lead to an amplification of low-frequency signals.

Although there exist by now several simulations of the full three-dimensional flow field (van Hengel, 1996; van Hengel *et al.*, 1996; Böhnke & Arnold, 1999; Parthasarathi *et al.*, 2000; Givelberg & Bunn, 2003; Cheng *et al.*, 2008), most studies either fail to describe the full physics of the fluid flow and/or they include just a passive BM. Böhnke & Arnold (1999), for instance, presented a finite-element model of the cochlea which describes an inviscid and compressible fluid flow and a passive description of the cochlear partition. Böhnke extended this model in a later work to study the perception of bone-conducted sound (Böhnke & Arnold, 2006) and the effect of a cochlear implant electrode on the cochlear mechanics (Kiefer *et al.*, 2006). Parthasarathi *et al.* (2000) neglected viscous effects in their three-dimensional simulation. Pozrikidis (2008) used boundary-integral methods to describe the interaction between the viscous perilymph and a passive BM in two dimensions. The recent model by Cheng *et al.* (2008) describes the interaction between a viscous fluid flow and a passive basilar membrane with a finite-element approach in a simplified three-dimensional geometry. The same geometry was used earlier in a laboratory experiment by White & Grosh (2005).

In addition to theoretical and numerical cochlear models, some physical models of the cochlea were developed. The life-sized models by Zhou *et al.* (1993), White & Grosh (2005) and Wittbrodt *et al.* (2006) allow detailed experimental studies of BM dynamics and can be used for the validation of theoretical and numerical results (at least for passive models).

2.2. Active cochlear models. The introduction of nonlinear active models for the BM had a major impact on cochlear modeling (see Manley *et al.*, 2008, for a recent and comprehensive discussion of active processes in the cochlea). Passive models typically describe the BM as a set of linear damped oscillators with varying mechanical properties along the cochlear axis. Active models account for the observation that a dead cochlea exhibits a response to acoustic stimulation which is different from in vivo experiments. The dynamics of a 'living' cochlea is found to be highly nonlinear and non-local (e.g. Robles & Ruggero, 2001). It is commonly believed that these phenomena are directly related to the electromotility of the outer hair cells. This electromotility leads to an expansion and

contraction of the OHC under the influence of an oscillating electric field (similar to the piezo effect). Electromotility together with the so-called hair cell gating (Steele, 1992) leads to a nonlinear amplification of the fluid pressure signal. Nowadays, it is widely accepted that these active nonlinear processes are responsible for the sharp tuning of the cochlea observed in in vivo experiments.

Prominent nonlinear active models for the cochlea are due to Steele and coworkers (e.g. Steele *et al.*, 2009; Lim & Steele, 2002). They formulate their models in a global context together with detailed local micromechanical models. To be able to work with these global models, i.e. to render these models computationally treatable, the original model is boiled down to a pseudo-local problem by a WKBJ method (Bender & Orszag, 1978). This asymptotic method is used to reduce the complexity of a model while retaining the most relevant global effects. Their multi-scale model of the organ of Corti (Steele *et al.*, 2009) embeds a detailed local description of the Corti organ into a global context by the WKBJ approximation. While this is arguably one of the most sophisticated models of global cochlear dynamics, it remains limited by the asymptotic approximation to the global signal transmission mechanisms.

There is yet another class of global cochlear models which have no ambition to describe every functional unit of the cochlea on the basis of first principles of the underlying physics. Rather, they seek to provide a compact and efficient model which reproduces the transduction of acoustic waves to nerve signals as accurately as possible. The model of Kern (2003) describes the central nonlinear mechanism by a Hopf-type amplifier. While Lim & Steele (2002) approximate the flow field by a vector-potential for the fluid displacement, Kern (2003) bases his description of the flow field on an analogy with surface water waves. The model of Kern (2003) has also been realized as an analog circuit (Martignoli *et al.*, 2007).

It has been shown that the models based on the work by Lim & Steele (2002) and Kern (2003) are able to reproduce several nonlinear phenomena commonly observed in clinical experiments such as: response compression, harmonic distortion, two-tone suppression, and distortion products (see, e.g. Lim & Steele, 2003; Kern & Stoop, 2003; Stoop & Kern, 2004; Stoop *et al.*, 2005; Yoon *et al.*, 2007; Stoop *et al.*, 2007; Kern *et al.*, 2008). Nevertheless, neither model is able to describe in detail the flow processes at work in cochlea.

This brief review of earlier work on global cochlear modeling should give a good overview on the current state-of-the-art. It points out the inherent problem in global cochlear modeling: no global model is able to describe all physical phenomena in the cochlea at an equal level of detail. In order to get a utilizable global model, concessions are made on the morphology, the active processes, the micromechanics in the OC, the fluid flow, or sometimes even on the numerical fidelity.

CHAPTER 13

One-dimensional passive cochlea model and pseudo-resonance

Since the work of von Békésy (1960) it is well accepted that an acoustic stimulation of the cochlea at the oval window leads to traveling waves on the basilar membrane (BM). These waves form a standing wave packet whose location depends on the frequency of the stimulation. Such wave packets do not quite satisfy homogeneous boundary conditions. The BM deflection at the oval window is non-zero due to the acoustic stimulation. As first suggested by Trefethen & Embree (2005) this relates cochlear dynamics directly to the concept of wave packet pseudomodes which are nearly exact eigenfunctions that violate the homogeneous boundary conditions only by an asymptotically small parameter ϵ. The theory of wave packet pseudomodes has been used successfully to study the hydrodynamic stability of various shear flows (Obrist & Schmid, 2011, 2010; Mao & Sherwin, 2011). In the following, we will derive approximations to wave packet pseudomodes in the cochlea on the basis of a linear one-dimensional model (Peterson & Bogert, 1950) and we will discuss these results with respect to resonance phenomena in the cochlea.

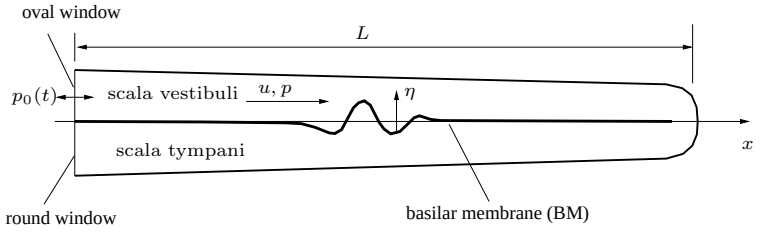

FIGURE 13.1. Schematic view of the uncoiled cochlea.

1. The transmission-line model

Arguably the simplest model which is able to reproduce the principal mechanisms of cochlear mechanics is known as the *transmission-line model*. It is due to

Peterson & Bogert (1950) who went through a careful analysis of cochlear fluid mechanics. Along this way, they were able to eliminate a large number of from the governing equations (e.g. acoustic waves in the perilymph) such that they finally arrived at a quite simple set of equations.

Although the transmission-line model is known to be flawed, it is still widely in use—primarily because of its simplicity. It is instructive to walk through the derivation of this model. As we will see in the following, the transmission-line model is closely related to the pulse propagation in a compliant fluid filled tube as it can be found in the arterial system.

For the transmission-line model, we assume one-dimensional inviscid flow in the scala vestibuli (the flow field in the scala tympani is assumed to be anti-symmetric). The axial velocity u, the pressure p and the deflection η of the BM are functions of the axial coordinate x (figure 13.1). The governing equations consist of two fluid equations for momentum and mass conservation, and an equation for the forced oscillation of the BM,

$$\rho \dot{u} = -p', \tag{93a}$$

$$u' = d\dot{\eta}, \tag{93b}$$

$$m\ddot{\eta} + r\dot{\eta} + k\eta = -2p. \tag{93c}$$

The function $d(x)$ is the ratio of the width of the BM to the cross-section $A(x)$ of the scala vestibuli, ρ is the fluid density, and $m(x)$, $r(x)$, and $k(x)$ determine the mechanical properties of the BM along the cochlea. The superscripts $\dot{}$ and $'$ stand for the partial derivatives with respect to t and x, respectively.

The equation for mass conservation, Eq. (93b), relates the gradient of the flow velocity to the velocity of the BM which increases or decreases the lumen of the scala vestibuli. This equation is the result of a simple mass balance in an infinitesimally short axial section of the scala vestibuli. It includes implicitly the assumption of long waves on the BM. This long-wave assumptions is one of the major weaknesses of the transmission-line model. If this assumption was dropped, the mass balance equation would obtain additional nonlinear terms. For a discussion of such a wave propagation model (in the context of arterial pulse waves) see Pedley (1980).

Note that the forcing with $-2p$ of the BM in Eq. (93c) is due to the pressure difference across the BM. If the pressure in the scala vestibuli is p then the pressure in the scala tympani is $-p$ (due to symmetry) such that the pressure difference is $-2p$.

For a harmonic stimulation at the oval window the equations can be transformed to the frequency domain and two of the three dependent variables can be eliminated to obtain an ordinary differential equation in x for the third dependent variable. We arrive at this equation by transforming the dependent variables to

the frequency domain,

$$(u(x,t), p(x,t), \eta(x,t)) = (\hat{u}(x), \hat{p}(x), \hat{\eta}(x))e^{-\mathrm{i}\omega t} \tag{94}$$

where $\omega \in \mathbb{R}$ is the stimulation frequency. The governing equations then read

$$\rho \mathrm{i}\omega \hat{u} = -\hat{p}', \tag{95a}$$

$$\hat{u}' = -d\mathrm{i}\omega\hat{\eta}, \tag{95b}$$

$$\underbrace{(-\omega^2 m - \mathrm{i}\omega r + k)}_{=Z(\omega)}\hat{\eta} = -2\hat{p}. \tag{95c}$$

such that $\hat{\eta}$ can be replaced by $-2\hat{p}/Z$,

$$\rho \mathrm{i}\omega \hat{u} = -\hat{p}', \tag{96a}$$

$$\hat{u}' = 2d\mathrm{i}\omega\hat{p}/Z. \tag{96b}$$

Finally, we can eliminate $\hat{u}$ by taking the derivative of Eq. (96a), such that we obtain

$$\hat{p}'' - \frac{2d\rho\omega^2}{Z(\omega, x)}\hat{p} = 0. \tag{97}$$

This equation defines a pressure wave with a varying phase speed. It becomes singular wherever the dispersion relation of the BM, $Z(\omega, x)$, has a root. The effective wave speed at these roots tends to zero and the amplitude of the response has a local maximum. This resonance phenomenon relates every frequency ω to a characteristic place $x(\omega)$ which defines the so-called 'tonotopic map' of the cochlea.

Because of the (weak) damping r of the BM, all roots ω of $Z(\omega, x \in \mathbb{R})$ are complex. Therefore, the steady-state solutions for harmonic stimulations exhibit a finite amplitude at the characteristic place. Increased damping further mollifies the solutions and reduces the sharpness of the tuning.

A mathematically rigorous discussion of the traveling wave phenomena in the cochlea can be found in Lighthill (1981*b*).

2. Traveling wave solutions

Typical traveling wave solutions of (93) are shown in figure 13.2. The BM amplitude increases slowly as we move from the oval window toward the apex. The amplitude peaks at a frequency-dependent location and then decays rapidly to zero for the remainder of the cochlea. Although the results look like the BM acts as a continuous mechanical structure, we have to keep in mind that the third equation (93c) has to be understood as a zero-dimensional equation for a set of independent mechanical oscillators which are forced by the local fluid pressure. The fluid pressure, of course, is a global variable governing the dynamics of the fluid in the whole cochlea. Therefore, the continuous structure of the BM is not

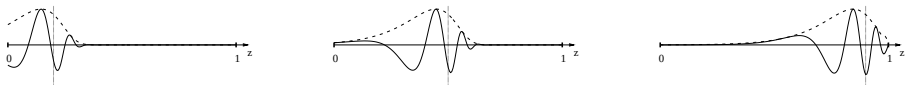

(a) (b) (c)

FIGURE 13.2. Typical solutions of the transmission line model for (a) low , (b) medium and (c) high frequency stimulation. The x-axis ranges from 0 (oval window) to 1 (apex). The solid line shows the BM deflection at a specific time and the dashed line is the BM amplitude. The vertical broken lines indicate the value of x_* for the corresponding frequency.

the result of a mechanical coupling within the BM. It is due to the tight interplay between the dynamics of the perilymph and the BM.

The transmission line model features many characteristics of the real cochlea. However, some of the basic assumptions underlying this model are clearly violated in a real cochlea. Foremost, it is the assumption of a (nearly) one-dimensional flow field which bears problems. One-dimensional flow is a reasonable idealization for long wave lengths on the BM. For high wave numbers (as we see them, for instance, in figure 13.2) the continuity equation shows us that flow velocities perpendicular to the BM cannot be neglected. Furthermore, the transmission line model fails to match the sharp tuning of the real cochlea (as observed in clinical experiments).

3. Wave packet pseudomodes of the cochlea

For a further study[1] of the solutions of the transmission line model, we make the independent variables t and x and the parameters m, r, k, and d dimensionless:

$$x = L\tilde{x}, \quad t = \omega_0^{-1}\tilde{t}, \quad m = m_0\tilde{m}, \quad r = r_0\tilde{r}, \quad k = k_0\tilde{k}, \quad d = d_0\tilde{d}. \tag{98}$$

The base frequency ω_0 is defined as $\sqrt{k_0/m_0}$. We eliminate w and p from (93) and write the resulting equation in phase space with $\boldsymbol{\eta} = (\eta, \dot{\eta})^T$,

$$\mathcal{L}\dot{\boldsymbol{\eta}} = \mathcal{R}\boldsymbol{\eta} + \mathbf{f}(x,t) \tag{99a}$$

$$\mathcal{L} = \begin{pmatrix} 1 & 0 \\ 0 & d - \epsilon^2(m'' + 2m'\frac{\partial}{\partial x} + m\frac{\partial^2}{\partial x^2}) \end{pmatrix} \tag{99b}$$

$$\mathcal{R} = \begin{pmatrix} 0 & 1 \\ \epsilon^2(k'' + 2k'\frac{\partial}{\partial x} + k\frac{\partial^2}{\partial x^2}) & \epsilon^2\nu(r'' + 2r'\frac{\partial}{\partial x} + r\frac{\partial^2}{\partial x^2}) \end{pmatrix} \tag{99c}$$

[1]This section is based on the conference paper by Obrist & Schmid (2008).

where we dropped all $\tilde{}$ for the ease of writing and $\dot{}$ and $'$ are now derivatives with respect to the dimensionless variables. This equation contains two dimensionless coefficients (damping coefficient ν, slenderness coefficient ϵ)

$$\nu = \frac{\omega_0 r_0}{k_0}, \qquad \epsilon^2 = \frac{m_0}{2\rho d_0 L^2} \sim \frac{A}{L^2} \ll 1. \tag{100}$$

We assume zero pressure boundary conditions at both ends of the cochlea. The acoustic stimulation at the oval window enters the governing equation (99) as a forcing term $\mathbf{f}(x,t) = (0, 2\delta''(x)p_0(t))^T$ where $\delta(x)$ is Dirac's delta function.

The steady-state response of the BM due to a harmonic stimulation $\mathbf{f}(x,t) = \mathbf{f}_0(x)e^{-\mathrm{i}\omega t}$ is given by

$$\boldsymbol{\eta} = -[\mathcal{R} + \mathrm{i}\omega\mathcal{L}]^{-1}\mathbf{f}_0 e^{-\mathrm{i}\omega t}. \tag{101}$$

As we have seen in figure 13.2, such resonance solutions of (99) have the shape of wave packets. They correspond to wave packet pseudomodes which are asymptotically good approximations to eigenfunctions (Trefethen & Embree, 2005). We characterize a wave packet pseudomode centered at $x = x_*$ by its local wave number α_*/ϵ and its (pseudo-)eigenvalue λ.

In the theory of wave packet pseudomodes the parameters x_* and α_* are related to λ by the operator symbol. (The symbol of an operator corresponds to the eikonal equation of its WKBJ expansion.) The implicit form of the symbol of (99) is

$$-\mathrm{i}\lambda\mathbf{L}\hat{\boldsymbol{\eta}} = \mathbf{R}\hat{\boldsymbol{\eta}} \tag{102a}$$

$$\mathbf{L} = \begin{pmatrix} 1 & 0 \\ 0 & d - \epsilon^2 m'' - 2\epsilon\mathrm{i}\alpha_* m' + {\alpha_*}^2 m \end{pmatrix} \tag{102b}$$

$$\mathbf{R} = \begin{pmatrix} 0 & 1 \\ \epsilon^2 k'' + 2\epsilon\mathrm{i}\alpha_* k' - {\alpha_*}^2 k & \nu(\epsilon^2 r'' + 2\epsilon\mathrm{i}\alpha_* r' - {\alpha_*}^2 r) \end{pmatrix} \tag{102c}$$

with $\hat{\boldsymbol{\eta}} = (\hat{\eta}, \lambda\hat{\eta})^T$. The functions d, m, k, r, and their derivatives are evaluated at x_*. However, a wave packet pseudomode exists only if the twist condition is satisfied (Trefethen & Embree, 2005). The generalized twist condition for symbols in matrix form is

$$\mathrm{Im}\left\{ \frac{\partial \det(\mathbf{F})}{\partial x_*} \Big/ \frac{\partial \det(\mathbf{F})}{\partial \alpha_*} \right\} < 0 \tag{103}$$

where $\mathbf{F} = \mathbf{R} + \mathrm{i}\lambda\mathbf{L}$. Figure 13.3 shows the symbol curves $\lambda = \lambda(x_*, \alpha_* = -\infty \ldots \infty)$ for which (102) and (103) are satisfied.

We obtain asymptotically good approximations for the location (and the local wave number) of the wave packet in the steady-state solution, if we choose x_* and α_* such that $\lambda(x_*, \alpha_*) = \omega \in \mathbb{R}$ (i.e. where the symbol curve cuts the real axis). The vertical broken lines in figure 13.2 indicate the value of x_* which correspond to the respective frequency. Apparently, x_* (and also α_*) predicts the location and local wave number of the wave packet reasonably well.

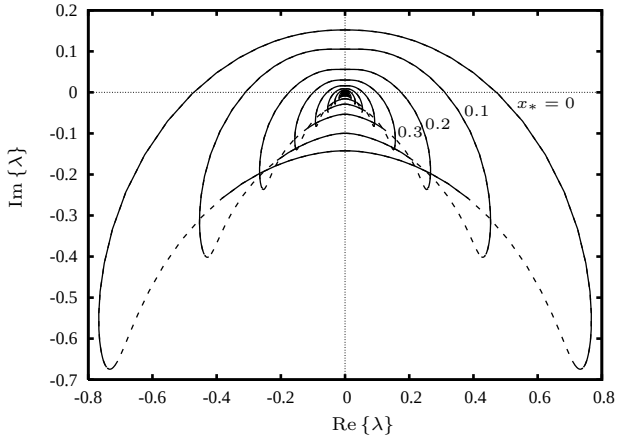

FIGURE 13.3. Symbol curves $\lambda(x_*, \alpha_*)$ for $x_* = 0, 0.1, \ldots, 1$ and $\alpha_* \in \mathbb{R}$. The dashed lines indicate the sections of the symbol curves for which the twist condition is not satisfied.

The theory of wave packet pseudomodes provides elegant analytical tools for predicting resonance phenomena in the cochlea. The symbol curves in figure 13.3 give immediate insight into the dynamics of the cochlea. They hold more information than the eigenvalues of (99). Apart from the results shown here, the theory of wave packet pseudomodes can help us to learn more about the transient dynamics of the cochlea. It has been observed, for instance, that cochlear pseudomodes located on the upper half-plane of figure 13.3 exhibit transient growth (with respect to a metric based on potential and kinetic energy of the BM). Furthermore, Obrist & Schmid (2010) have shown how the symbol curves can be used to predict the group velocity of localized disturbances.

CHAPTER 14

Two-dimensional inviscid passive cochlea model

In this chapter, we present a re-formulation in the time domain of an established two-dimensional inviscid model for a passive cochlea[1] which was originally formulated in the frequency domain by Lesser & Berkley (1972). First, this model is an illustration for a robust numerical solution of this tightly coupled fluid-structure problem in the time domain. And second, the model provides a simple numerical tool for studying basic transient flow processes in the cochlea.

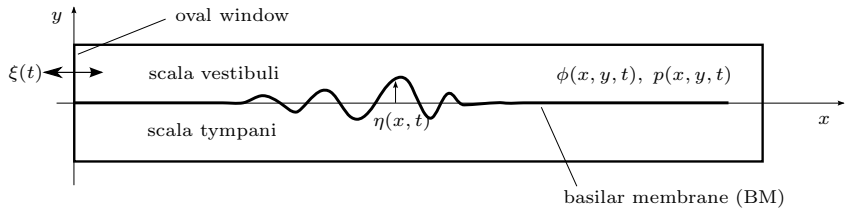

FIGURE 14.1. Two-dimensional model of the cochlea as a slender box partitioned by a flexible basilar membrane.

For our purpose, we simplify the cochlea to a slender rectangular box (figure 14.1) which is split into two fluid-filled separate ducts (scalae vestibuli and tympani) by an elastic partition (basilar membrane, BM). The system is stimulated through a flexible membrane (oval window) with a velocity $\xi(t)$.For simplicity, we assume that the velocity profile at the oval window is rectangular. The BM can be displaced only by a small amount η in the transversal direction. The dynamics of the BM is described by a set of damped linear oscillators which have no direct mechanical connection to their neighbors such that axial coupling along the BM is only possible via the fluid motion. The fluid motion itself is described as a potential flow with slip boundary conditions at the walls for which the BM motion yields the normal velocity boundary conditions. Symmetry allows us to reduce the problem to the scala vestibuli and the BM. Although this description

[1]This chapter is based on the proceedings article by D. Obrist, Proc. Appl. Math. Mech. **9**, 2009.

neglects several important effects such as unsteady boundary layers, it has its merits for high frequency stimulations. The governing equations are

$$\nabla^2\phi = 0 \tag{104a}$$

$$\rho\dot{\phi} + p = 0 \tag{104b}$$

$$m\ddot{\eta} + r\dot{\eta} + k\eta = -2p\,|_{y=0} \tag{104c}$$

$$\partial\phi/\partial y|_{y=0} = \dot{\eta} \tag{104d}$$

where ρ is the fluid density and ϕ is the flow potential which is driven by the pressure p in the linearized momentum equation (104b). The forced oscillation of the BM is described by (104c) where $m(x)$, $r(x)$, and $k(x)$ are the mass, damping and stiffness parameters of the BM (values taken from Lesser & Berkley, 1972). Finally, the compatibility condition (104d) couples the BM to the flow field.

1. Numerical modeling

To solve the governing equations, we eliminate the pressure p and recast the equations as a system first-order differential equations in time,

$$\begin{pmatrix} \gamma\partial/\partial y(\cdot)|_{y=0} & 0 & -\gamma \\ 0 & 1 & 0 \\ -2(\cdot)|_{y=0} & 0 & m/\rho \end{pmatrix} \begin{pmatrix} \dot{\phi} \\ \dot{\eta} \\ \ddot{\eta} \end{pmatrix} = \begin{pmatrix} \partial/\partial y(\cdot)|_{y=0} & 0 & -1 \\ 0 & 0 & 1 \\ 0 & -k/\rho & -r/\rho \end{pmatrix} \begin{pmatrix} \phi \\ \eta \\ \dot{\eta} \end{pmatrix} \tag{105}$$

which has to be integrated in times under the condition that $\nabla^2\phi = 0$ remains satisfied. The parameter $\gamma \neq 0$ has been introduced (a) to render the matrix on the left-hand side non-singular, and (b) to allow us to set the eigenvalues associated with the compatibility equation (104d) to γ^{-1}, i.e. we avoid numerical instabilities by setting $\gamma < 0$.

To discretize (105) in space, the BM displacement η and velocity $\dot{\eta}$ are discretized on a grid of N equidistant points x_j along the BM. For the flow potential ϕ, we make the spectral ansatz

$$\phi(x,y,t) = \xi(t)\,[\hat{x}(1-\hat{x}/2) - \hat{y}(\sigma - \hat{y}/2)] + \sum_{k=0}^{N-1} a_k(t)\frac{\cosh k\pi(\sigma-\hat{y})}{\cosh k\pi\sigma}\cos k\pi\hat{x} \tag{106}$$

which is a generalization of the ansatz used by Lesser & Berkley (1972) (the coordinates $\hat{x}$ and $\hat{y}$ have been non-dimensionalized with the length of the cochlea and $\sigma \ll 1$ is the aspect ratio of the scala vestibuli). This ansatz satisfies the Laplace equation (104a) and the boundary conditions at the oval window and at the solid walls. The coefficients a_k, the BM displacement $\eta(x_j)$ and velocity $\dot{\eta}(x_j)$ can now be determined by integrating the system (105) in time with a generalized Crank-Nicolson scheme. We choose this implicit time integration scheme over an explicit scheme to prevent any numerical instabilities related to the fluid-structure interaction (e.g. Causin *et al.*, 2005).

In this modeling framework the helicotrema can be easily integrated by eliminating the fluid-structure interaction at the apex of the 'numerical BM', i.e. we set the mechanical properties of the BM at this location such that it behaves like a passive tracer which has no influence on the fluid.

2. Transient stimulations

In figure 14.2 we show the results for an impulsively started harmonic stimulation with 5kHz (zero initial conditions, $N = 200$). The steady-state response (wave packet centered at $x \approx 7.5$mm) is quickly established while a decaying wave packet travels slowly toward the apex. This wave packet is a transient phenomenon which is eventually washed out. It is likely that this phenomenon is much weaker in a real cochlea because of the fluid viscosity which is neglected here. Furthermore, it is observed (not shown here) that the helicotrema (located at $35\,\text{mm} < x < 37\,\text{mm}$) helps to reduce the amplitude of the transient wave packet more quickly.

The wiggles in the wave packet at $x \approx 7.5\,\text{mm}$ in figure 14.2(c) illustrate the phase speed of the traveling wave. We see that it is continuously reduced toward the characteristic place. The trace of the transient wave packet traveling toward the apex of the cochlea indicates the group velocity which tends toward zero at the apex.

Figure 14.3 shows results for a click stimulation with an approximate duration of 10^{-4}s. The stimulation amplitude is chosen such that the maximum displacement of the oval window is 1μm. The results show a traveling wave packet which moves from the oval window toward the apex with decreasing group velocity. The potential energy density of the BM peaks at $x \approx 12.6$mm and $t \approx 0.001$s. This peak shifts toward the apex and to later times for longer clicks.

This simulation is an impressive illustration of the transient nature of cochlear mechanics. Cochlear models formulated in the frequency domain suggest that a click must lead to a broadbanded stimulation of the BM (due to the broad frequency content of clicks). Figure 14.3(c) shows that this is indeed the case. However, this broadbanded stimulation occurs sequentially over the course of several milliseconds (from high toward low frequencies) which certainly leads to a different sound perception as if all hair cells were stimulated simultaneously.

The presented simulation is a robust and versatile numerical tool. It can be used to study a variety of effects related to non-harmonic stimulations of the cochlea (e.g. speech, music). Furthermore, we can simulate initial value problems to study the non-modal dynamics of the cochlea (Obrist & Schmid, 2008). In the following chapter, we will present a concept for including the active processes of the OHC into this model.

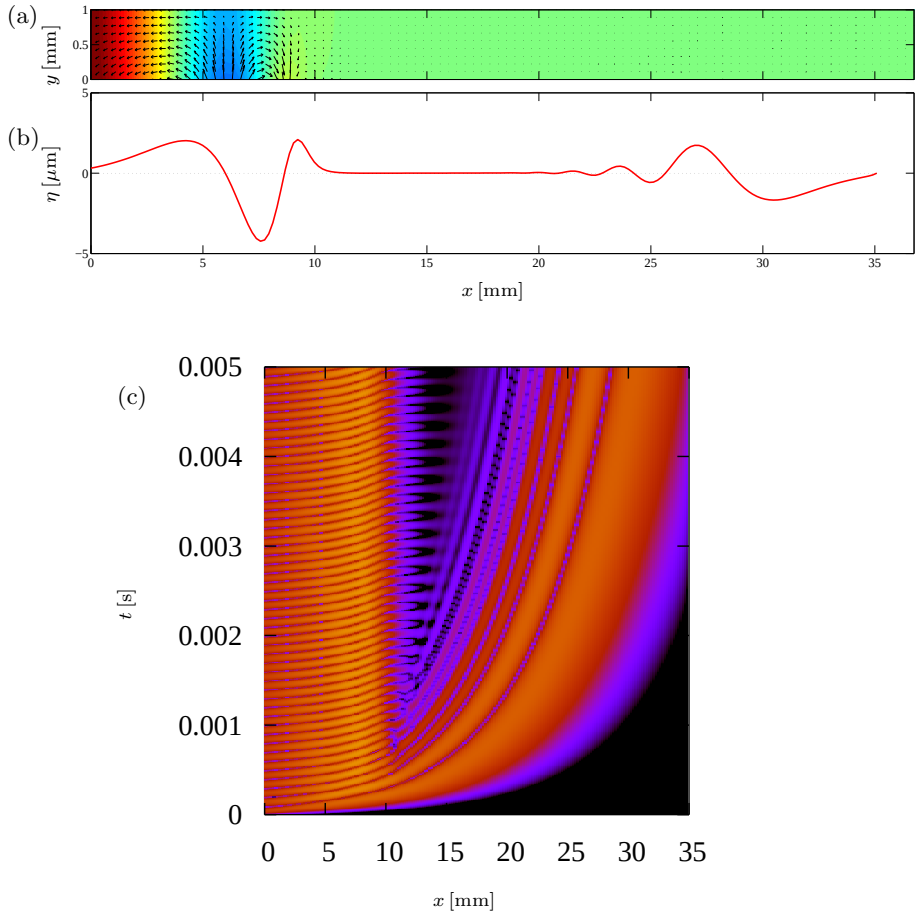

FIGURE 14.2. Impulsively started stimulation at 5 kHz: (a) snapshot of the flow field at $t = 0.005$s (arrows: velocity vectors, colors: pressure field); (b) snapshot of the BM displacement at $t = 0.005$s; (c) x-t-diagram for the potential energy density $k\eta^2/2$ along the BM (bright colors indicate high energy).

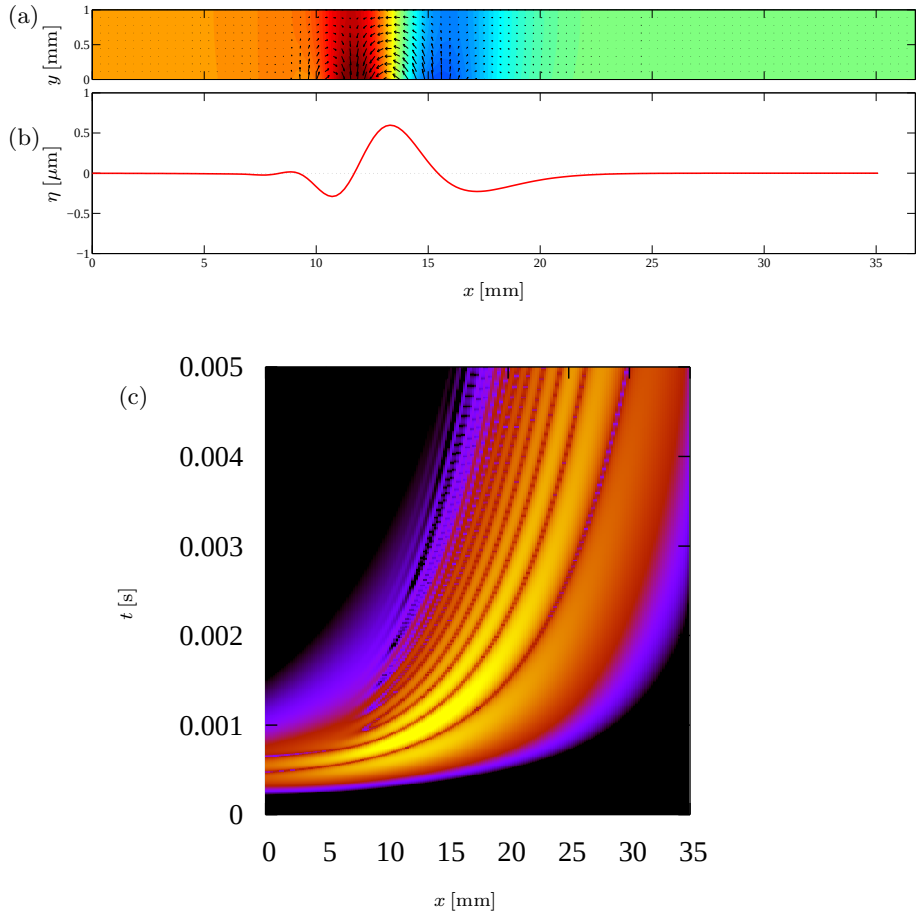

FIGURE 14.3. Click stimulation (duration 10^{-4} s): (a) snapshot of the flow field at $t = 0.001$s (arrows: velocity vectors, colors: pressure field); (b) snapshot of the BM displacement at $t = 0.001$s; (c) x-t-diagrams for the potential energy density $k\eta^2/2$ along the BM (bright colors indicate high energy).

CHAPTER 15

Modeling of the active processes

In this chapter[1], we will present a concept for including the active processes in a global cochlear model. A detailed discussion of the active processes in the cochlea from a biomedical point of view is given in the book of Manley *et al.* (2008).

Similar to a passive model (e.g. Chapter 13), the passive basilar membrane is modeled by a set of linear oscillators,

$$m(\eta)\ddot{\eta} + r(\eta)\dot{\eta} + k(\eta)\eta = \Delta p + b\zeta. \tag{107}$$

where η denotes the normal displacement of the basilar membrane, $m(\eta)$ the mass of the oscillators, $r(\eta)$ the damping, $k(\eta)$ the stiffness, and Δp the pressure difference across the membrane. The last term $b\zeta$ describes an additional forcing by active amplification.

The active amplification of the basilar membrane motion is modeled by nonlinear oscillators which feature a Hopf bifurcation (Kern & Stoop, 2003; Duke & Jülicher, 2007). The dynamical behavior of such a system is governed by the equation

$$\dot{\zeta} = (\mu + \mathrm{i}\omega)\zeta - |\zeta|^2\zeta + \gamma\dot{\eta} \tag{108}$$

with the complex amplitude ζ , the bifurcation parameter μ, the Hopf neutral frequency ω and a complex multiplier γ of the forcing term which couples the nonlinear oscillator to the velocity $\dot{\eta}$ of the basilar membrane.

Such an active amplification has been investigated and implemented[2] into the two-dimensional inviscid global cochlear model which was described in Chapter 14. With an appropriate tuning of the parameters ω, μ, γ and b of the active model we can reproduce typical results for active processes in the cochlea. Figure 15.1 shows the effect of the nonlinear amplification, tuning and response compression. These results compare well qualitatively to the experimental data for chinchilla by Robles & Ruggero (2001).

[1]This chapter is based on the proceedings article 'Simulation of fluid flow and basilar membrane motion in a two-dimensional box model of the cochlea' by E. Edom, D. Obrist, L. Kleiser which was presented at the 11th Int. Mechanics of Hearing Workshop, Williamstown, Massachusetts, July 16-22, 2011

[2]Andreas Müller, semester thesis FS 2009, Institute of Fluid Dynamics, ETH Zurich

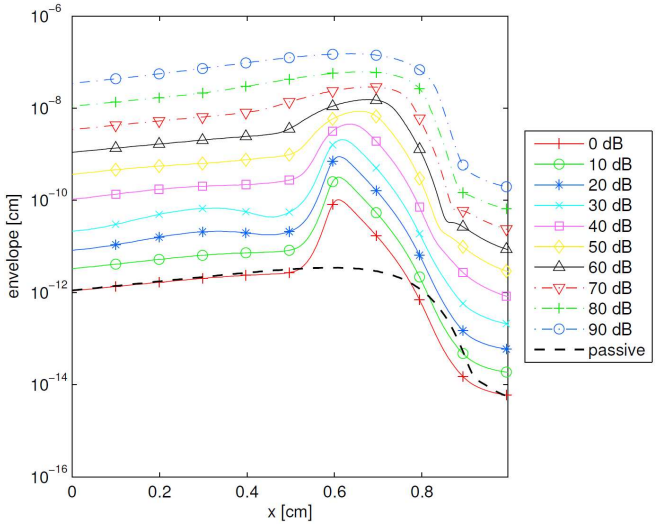

FIGURE 15.1. Wave envelopes of the BM displacement for a 5000 Hz stimulation at different intensities. The curves illustrate the amplification, tuning and response compression due to the active processes in the Corti organ. (Courtesy of A. Müller, Institute of Fluid Dynamics, ETH Zurich.)

Figure 15.2 shows a phenomenon known as *distortion product* which is observed when an (active) cochlea is stimulated by two neighboring harmonic tones[3] (here: $f_1 = 10\,\text{kHz}$, $f_2 = 12\,\text{kHz}$). The nonlinear active process creates other harmonics, i.e. distortion products, which result in displacements of the basilar membrane at other locations. The most prominent distortion products are generated for the frequencies $2f_1 - f_2 = 8\,\text{kHz}$ and $3f_1 - 2f_2 = 6\,\text{kHz}$. They are a direct result of the cubic term in Eq. (108). These two distortion products appear as traces on the x-t-diagram at $x \approx 0.4\,\text{cm}$ and $x \approx 0.5\,\text{cm}$ (note that these traces are relatively close to the base of the cochlea because BM has not been properly tuned for this experiment).

The pitch diagram in figure 15.2(b) shows that there exist also other distortion products at $f = 2\,\text{kHz}, 4\,\text{kHz}, 6\,\text{kHz}$. Furthermore it can be seen that these distortion products are not only present at their respective characteristic places but also all the way toward the oval window. This is a clear indication of so-called 'reverse traveling waves'.

[3] C.-F. Benner, Bachelor thesis 2011, Institute of Fluid Dynamics, ETH Zurich.

The locations of the local maxima on the pitch diagram run along a curve from the top left toward the bottom right. This is an indirect representation of the tonotopic map of the cochlea. It indicates the location of maximum resonance for a given frequency.

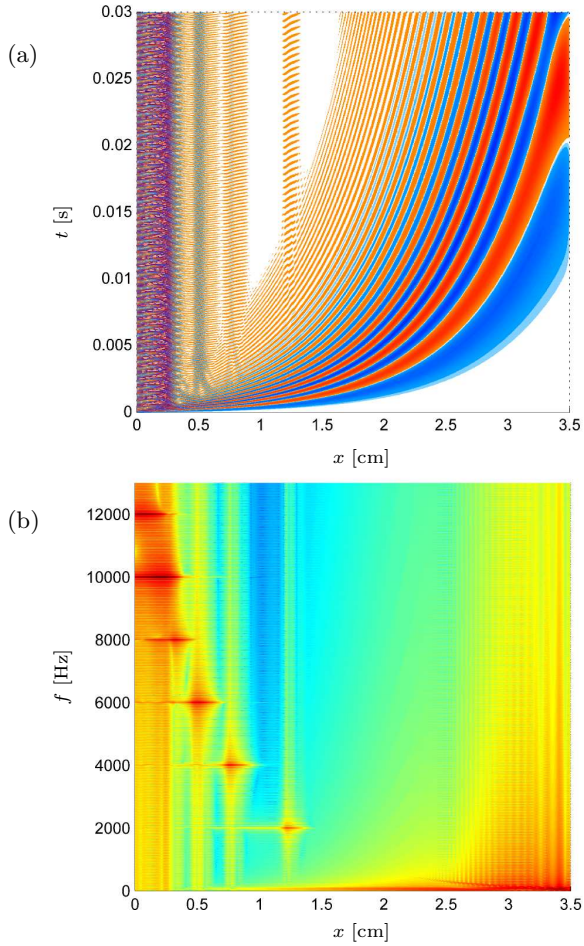

FIGURE 15.2. Distortion product for a two-tone stimulation with 10 and 12 kHz: (a) x-t-diagram showing the BM displacements (including the transient wave packet traveling toward the apex); (b) pitch diagram on the basis of a Fourier transform of the x-t-diagram between $t = 0.08$ and 0.1 s. The increased energy content at the bottom right of the pitch diagram is due to the transient wave packet. (Courtesy of C.-F. Benner, Institute of Fluid Dynamics, ETH Zurich.)

CHAPTER 16

Acoustic streaming in the cochlea

Acoustic streaming is a fascinating phenomenon in fluid mechanics where an oscillating component in a flow field (e.g. acoustic waves) generates a steady directed flow. Often the steady streaming component is much stronger than the primary oscillating flow. Probably the first to consider streaming phenomena was Rayleigh (1884). A contemporary review on acoustic streaming is given by Riley (2001).

The terms 'steady streaming' and 'acoustic streaming' are used interchangeably for this phenomenon, although the latter can be misleading because the streaming does not necessarily require acoustic waves. This is especially the case in the context of cochlear mechanics where the streaming phenomena are due to the traveling waves in the perilymph which is an incompressible flow phenomenon. Nevertheless, the term 'acoustic streaming' has found its way into the field of cochlear mechanics mainly due to the seminal contribution by Sir James Lighthill with his article on 'Acoustic streaming in the ear itself'. He studied the possibility for steady streaming within the cochlea on a theoretical basis (Lighthill, 1992). This work was based on the earlier articles by Lighthill on acoustic streaming (Lighthill, 1978) and on cochlear mechanics (Lighthill, 1981*b*,*a*).

In general, acoustic streaming is related to the Reynolds stresses generated by the primary oscillating flow field. The streaming phenomena can be classified in two principal mechanisms: the 'quartz wind' and 'Rayleigh streaming'. Whereas the former can be found in the main body of fluid, the latter is related to the boundary layers (Riley, 2001).

Apart from the theoretical work by Lighthill (1992) there is very little literature on streaming phenomena within the cochlea. A short discussion on streaming in the perilymph is given by Lesser & Berkley (1972) where they point out the relation to the so-called Békésy eddies (figure 4 in Lesser & Berkley, 1972). The short article by Böhnke & Scharff (2009) gives a framework for the study of acoustic streaming in the cochlea but does not provide any results. Streaming phenomena have also been investigated in other organs, e.g. in the eye by Repetto *et al.* (2008). Simulations of the perilymphatic flow by the author's group showed evidence for a weak streaming directly induced by the stapes vibrations. These

results were obtained in the simulation framework outlined in Chapter 17 which solves directly the Navier–Stokes equations.

1. Lighthill's study of acoustic streaming in the cochlea

Lighthill (1992) showed that the quartz wind in the cochlea is rather weak, whereas the Rayleigh streaming can lead to significant flow velocities. He also touched a third form of acoustic streaming which is related to the mean fluid particle motion in the direction of wave propagation for surface waves in deep water. This effect is known as Stokes drift and can lead to streaming velocities up to V^2/c where V is the velocity amplitude of the traveling wave and c its phase velocity. This term may become large at the characteristic place where V reaches its maximum while the phase velocity c tends to zero. However, Lighthill (1992) showed that the Stokes drift is exactly canceled outside the boundary layer by an opposing flow due to the Stokes boundary layer itself.

The velocities due to Rayleigh streaming at the edge of the boundary layer reach values up to

$$u_s = \frac{V^2}{4c} - \frac{3VV'}{4\omega} \tag{109}$$

where V' indicates the gradient of the velocity amplitude along the main axis of the cochlea. Lighthill (1992) points out that the fluid velocity amplitude V can also be taken as the velocity amplitude of the BM motion wherever the flow is two-dimensional.

The streaming velocity u_s can be understood as a slip velocity with which the bulk flow slips over the wall (excluding the thin boundary layer). It has been derived by Lighthill (1992) for the nearly two-dimensional flow in the vicinity of the characteristic place. The first term in (109) is due to the phase difference between the axial and the wall-normal velocity which leads to a 'shear-stress' component of the Reynolds stress. The second term in (109) is due to the variation of V in axial direction and is related to the 'normal-stress' component of the Reynolds stresses.

According to (109), the streaming velocity u_s can become significant (with respect to the BM velocity amplitude V) either if the phase velocity becomes small or if the gradient V' becomes large. This is the case in the vicinity of the characteristic place. Note that the second term contributes constructively to the first term for $V' < 0$, i.e. after the maximum BM displacement when the amplitude drops rapidly to zero.

2. Physiological relevance

Although Lighthill (1992) gives no quantitative results, he makes it clear that the even conservative estimates suggest significant streaming velocities in the cochlea. Nevertheless, the relevance of acoustic streaming in the cochlea is

not well established. There are, however, several places where acoustic streaming could play a role in the mechanics of hearing.

First and foremost, it is the mechanism for the stimulation of the inner hair cells (IHC). There appears to be a consensus that the stereocilia (hair bundles) of the IHC are not embedded in the tectorial membrane (unlike the stereocilia of the OHC; cf. figure 1.6). Therefore, the deflection of the IHC stereocilia must be related to a flow in the subtectorial gap (gap beneath the tectorial membrane). A purely oscillatory flow in this gap deflects the stereocilia in a way that the IHC are stimulated and inhibited in alternation. This is certainly a much less efficient way of stimulating the IHC than deflecting the stereocilia only to one side through a streaming flow within the subtectorial gap. Lighthill (1992) studied this possibility and showed that such a streaming is possible at least on a theoretical basis. Even though Lighthill did not include the active processes in the Corti organ directly in his considerations, his results remain relevant for IHC stimulation also because the active processes lead to sharper gradients in the flow field which can enhance streaming effects.

Second, acoustic streaming takes place in the perilymphatic fluid spaces. The Békésy eddies are in vitro evidence of a slow streaming flow which originates at the place of maximum BM displacement (i.e. the characteristic place). Most likely, the Békésy eddies can be related to the mechanisms of Rayleigh streaming where Reynolds stresses within the thin boundary layer lead to a steady Stokes flow in the whole field. Lesser & Berkley (1972) argue that these effects are weak because the gradients in their (passive) cochlear model are small. This brings us back to the point mentioned before, that acoustic streaming is most likely greatly enhanced in an active cochlea.

The Békésy eddies and all other streaming flows in the lymphatic ducts are churning the lymph. This could be of relevance of the slow but steady replacement of old lymph with new fluid. The mixing process due to streaming could enhance the transport of metabolites dissolved in the lymphatic fluids. A steady streaming of the endolymph within the scala media could support the metabolism of the active processes in the organ of Corti. This possibility (for which there is no evidence at this point) is even more intriguing if we consider that the vascularization of the Corti organ is very sparse and that the streaming is strongest at the place of maximum BM displacement, i.e. at the place with the highest metabolic demand.

Finally, it should be emphasized that the mechanisms of acoustic streaming within the cochlea must not be confused with the nonlinear effects which are classically related to an active cochlea. The nonlinear phenomena of acoustic streaming in the cochlea are quite weak and are unlikely to lead to nonlinear phenomena such as distortion products or two-tone suppression. Such phenomena

must be related to the nonlinear dynamics of the OHC which is discussed in Chapter 15.

CHAPTER 17

Transient viscous model of an active cochlea

In the present chapter, we outline a global cochlear model as it is developed and used by the author's group. The state-of-the-art in global cochlear modeling has already been laid out in Chapter 12. In contrast to other global models (e.g. Böhnke & Arnold, 1999, 2006), the present model has a strong focus on the perilymphatic flow field while the solid mechanics of the cochlea is described by lumped parameter models. Furthermore, it does not model the endolymphatic flow within the scala media and idealizes the cochlear geometry to a simple box model. It does, however, include the active processes in the OHC and solves the full Navier–Stokes equations such that viscous effects as well as weak nonlinear flow phenomena are captured. Unlike global models which were formulated in the frequency domain (e.g. Lim & Steele, 2002) this model is formulated in the time domain which allows the study of transient phenomena in the cochlea.

1. Rationale for the transient, nonlinear, viscous, active model

While the quality of cochlear models has enormously improved over the past years with respect to the BM dynamics, the modeling of the fluid dynamics in the cochlea has not kept pace. Relatively few studies with a focus on the flow system exist today and many of them are flawed by disrespecting relevant physical phenomena. Several effects which are currently attributed to other functional units in the cochlea (e.g. strong mechanical damping in the BM) might in reality be related to hydrodynamic effects. At the same time, some flow phenomena assumed implicitly (e.g. irrotational flow) by current models may not exist in reality. In contrast to these observation, the cochlear model by Givelberg & Bunn (2003) features an accurate representation of the flow field. Unfortunately, they used only a passive BM model and the authors indicate at the end of their paper that the representation of the BM needs to be improved. Exactly along this line of thought, we combine here an established nonlinear active model for the dynamics of the BM with a high-fidelity flow simulation.

To our knowledge, none of the currently available global cochlear models is able to describe *all* of the following flow phenomena:

(i) **Acoustic streaming** — this phenomenon can only be studied if the Navier–Stokes equations are *not* linearized.
(ii) **Unsteady boundary layers** — cochlear models based on potential flow solutions neglect the presence of unsteady boundary layers whose thickness depends on the frequency of the stimulation.
(iii) **Reverse traveling waves** — a representation of reverse traveling waves requires a correct description of the boundary conditions at the base and the apex of the cochlea (i.e. , oval window and helicotrema).
(iv) **Flow at the basal end of the cochlea** — the motion of the stapes which does not necessarily move like a piston (Huber *et al.*, 2001; Sim *et al.*, 2010)) and the position of the oval window which is located rather at the side than at the front end of the scala vestibuli may lead to complex flow structures at the basal end of the cochlea.
(v) **High shear close to the characteristic place** — active BM amplification leads to steep axial gradients in the flow field close to the characteristic place which may trigger strong viscous effects.

Here, we present a global cochlear model which is able to confirm or dismiss the relevance of these phenomena.

1.1. Transient dynamics. The model is formulated *in the time domain* which allows us to perform transient simulations. Many previous studies of cochlear dynamics are limited to harmonic stimulations (pure tones). In that case, the governing equations can be studied *in the frequency domain* (at least for linear models). The BM response is then a steady-state response oscillating with the stimulation frequency. However, these results give no indication about the transient process that leads to this steady-state solution. Neither do we know how long it takes to reach the steady-state, nor can we find out which parts of the cochlea are stimulated during the transient phase. However, this and other information about the transient phase is important for a comprehensive understanding of cochlear dynamics, since the cochlea hardly ever has to respond to steady-state (or even pure tone) stimulation. Music, speech and environmental noise have a very transient nature. Moreover, many clinical experiments use clicks as acoustic stimulant.

A simple example for the relevance of the transient processes in the cochlea is the effect of the helicotrema in a transmission-line model of the cochlea (Chapter 13). If we solve this model in the frequency domain for steady-state solutions we obtain (nearly) the same solutions whether we do or do not include the helicotrema. Only if we solve this model in the time domain as a forced initial value problem, we observe an influence of the helicotrema and find that the steady-state solution is reached more rapidly if the helicotrema is considered (see also Xin (2004) for a discussion of related effects).

Furthermore, transient simulations might shed some light on the dynamics of waves traveling toward the basal end of the cochlea: a phenomenon which is relevant for the understanding of otoacoustic emissions (OAE) (He *et al.*, 2008) and has been touched in the past by several authors (e.g. Lighthill, 1992).

1.2. Flow phenomena in the cochlea. As we will point out in the following, a careful study of the fluid dynamics in the cochlea calls for a numerical solution of the full Navier–Stokes equations. The character of the flow in the cochlea is uncommon to typical problems in fluid dynamics: On the one hand, the small size of the cochlea and the small flow velocities lead to small Reynolds numbers which indicate a flow dominated by viscosity. On the other hand, the high frequencies lead to strong unsteady effects. The low Mach number and the long length of acoustic waves in perilymph indicates that compressibility effects are negligible (although Lighthill, 1981*b* provides some arguments that compressibility could have an effect anyway). And finally, the compliance of the BM leads to wave propagation (similar to pulse waves in the arterial system). In addition, these waves are strongly influenced by nonlinear amplification in the BM. Technically speaking, the flow in the scala vestibuli is a highly unsteady creeping flow through a compliant pipe with nonlinear amplification.

Because of the small Reynolds number in the cochlea ($Re < 1$) one might be tempted to describe the flow only by the (unsteady) Stokes equations rather than by the full Navier–Stokes equations. This, however, would neglect (even weak) nonlinear effects which might be relevant to cochlear dynamics (for instance, acoustic streaming in the cochlea as discussed in Chapter 16). Other considerations might also lead one to believe that viscosity can be neglected. Lesser & Berkley (1972), for instance, argued that the boundary layers in the cochlea are very thin and, therefore, negligible. While it is true that these Stokes boundary layers are very thin for high stimulation frequencies (their thickness scales like the inverse of the square root of the stimulation frequency) they must not be neglected for lower frequencies. Figure 17.1 illustrates this fact by plotting velocity profiles for a pulsating flow in a pipe (Womersley, 1955) with the approximate dimensions of the scala vestibuli. For low frequencies (figure 17.1b) the flow profile deviates dramatically from a nearly rectangular flow profile that we obtain for high frequencies (figure 17.1a). In addition, there is a frequency-dependent phase shift between the bulk flow rate and the pressure gradient (which will also lead to a phase shift in the BM response). We can see this shift by comparing the flow profiles at the phase 0° (maximum pressure gradient) for the two different frequencies: at this instant there is almost no flow for the high frequencies, but there is a net flow to the right for the low frequency case while the fluid in the core is still flowing to the left. These unsteady boundary layers introduce a considerable amount of viscous dissipation and shear at the BM which may be out of phase with the bulk flow. Cochlear models which are based on a potential flow

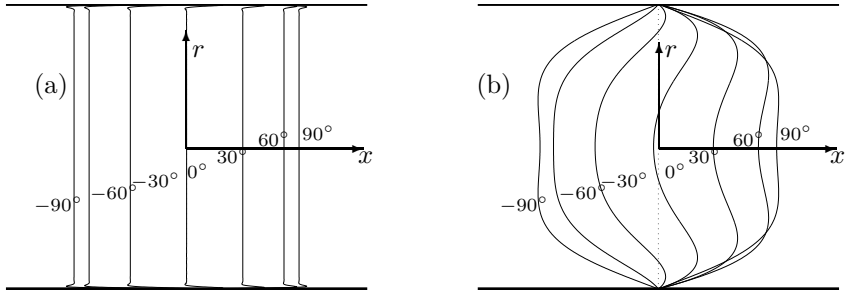

FIGURE 17.1. Velocity profiles for pulsating flow in a circular pipe for (a) 20kHz and (b) 20Hz. The values next to the curves indicate the phase of the pulsation: at 0° the pressure gradient reaches its maximum value and at ±90° it is zero. (pipe diameter 1mm; kinematic viscosity $10^{-6}\mathrm{m}^2/\mathrm{s}$)

solution implicitly assume the situation shown in figure 17.1a which appears to be appropriate only for high frequencies. The missing viscous damping in these models is usually included in the mechanical damping of the BM as in Eq. (93c).

1.3. Numerical aspects of cochlear fluid dynamics. Lesser & Berkley (1972) used a spectral method for the spatial discretization of the flow inside a box model of the cochlea. Despite the high numerical quality of this method, it is not suitable for the present model because spectral methods are relatively inflexible with respect to more involved boundary conditions. A detailed description of the boundaries of the scala vestibuli requires the formulation of dynamic boundary conditions with spatial variations (e.g. deflection of the oval window, changing material properties of the BM and an in-/outflow at the helicotrema). Therefore, we use finite-difference schemes for the spatial discretization. They allow a high convergence order, variable grid spacing, and a straightforward implementation of complex boundary conditions. Furthermore, we require a numerical time integration scheme with stability properties that allow a sufficiently large time step size even though the cochlea is a stiff dynamical system.

2. Definition of the computational model

2.1. Cochlear geometry. Rather than using a coiled geometry, we use an idealized uncoiled geometry ("box model") which consists of a single rectangular duct with constant cross section (figure 17.2). This duct represents the scala

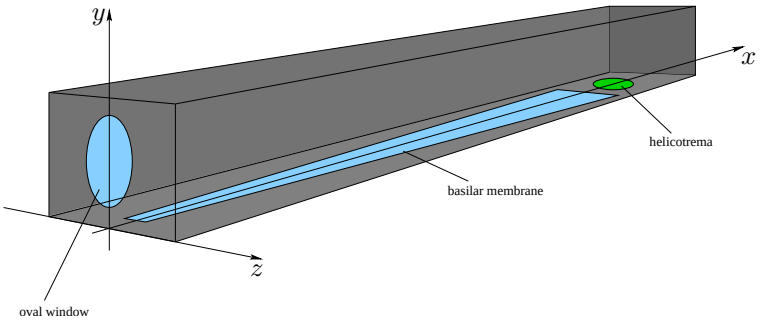

FIGURE 17.2. Computational domain with the boundary conditions (gray: no-slip; blue: Dirichlet in-/outflow; green: (anti-)symmetry.

vestibuli. The whole cochlear partition is collapsed to a flat plane which forms the bottom wall of the duct. The flow in the scala tympani is assumed to be anti-symmetric to the flow in the scala vestibuli and is not included explicitly in the computational domain.

2.2. Governing equations. We model the flow field of the perilymph by the Navier–Stokes equations,

$$\frac{\partial \mathbf{u}}{\partial t} + (\mathbf{u} \cdot \nabla)\mathbf{u} = -\nabla p + \frac{1}{Re}\nabla^2 \mathbf{u}, \tag{110a}$$

$$\nabla \cdot \boldsymbol{u} = 0, \tag{110b}$$

where $\boldsymbol{u}$ denotes the velocity vector, t the time, and p the pressure. The Reynolds number Re is based on the maximum velocity U_s of the stapes motion, the length L_s of the stapes footplate (approximately 3 mm), and the kinematic viscosity ν^* of the perilymph.

The Navier–Stokes equations are solved numerically on a Cartesian coordinate system with grid stretching toward the walls such that the Stokes boundary layers can be resolved. The simulations are carried out with a high-order Navier–Stokes solver (Henniger *et al.*, 2010) which uses finite-differences for discretizing the spatial derivatives and a three-step third-order Runge–Kutta scheme for the time integration.

2.3. Boundary conditions. The displacement of the BM (on the order of micro- to nanometers) is very small compared to the height of the scala vestibuli (on the order of a millimeter). Therefore, we assume that the flow domain maintains its shape during the whole simulation. The motion of the BM leads to Dirichlet boundary conditions for the normal velocity on the BM. It can be shown by a Taylor expansion that the velocity error due to this formulation of the BM

motion is of order $\eta^2/2$ where η is the displacement of the BM normal to the wall.

Similar to the BM motion, the stimulation at the oval window is represented by Dirichlet boundary conditions as well. The helicotrema is modeled by symmetry boundary conditions and at the remaining walls we impose no-slip boundary conditions.

2.4. Computational mesh. Because of unsteady viscous effects, we obtain boundary layers in the scala vestibuli whose thickness is proportional to the inverse of the square root of the frequency. Therefore, these unsteady boundary layers are thin for high frequencies and relatively thick for low frequencies. For a transient simulation which includes a larger range of frequencies we need therefore a fine spatial resolution close to the walls.

2.5. Time integration. From the point of view of numerical stability for the fluid-structure coupling between the perilymph and the BM, it is critical to include the equation for the BM properly into the time integration scheme of the fluid simulation. The allowable time step size is dominated by the time scales of the stimulation at the oval window and by the local eigenfrequencies of the BM.

2.6. Modeling of the BM dynamics. The formulation of the dynamics of the basilar membrane is an integral part of any global cochlear model. Here, we adapt the active BM model by Kern (2003) to our formulation, as it was already outlined in Chapter 15. In its original formulation, Kern's model uses a potential flow approximation for the fluid dynamics which is augmented by an energy dissipation term drawn from a surface wave analogy. Such an additional dissipation mechanism is not necessary for the present model because the whole viscous dissipation is already included in the flow simulation.

The details of the formulation are given in Chapter 15 whereas the mass term in (107) may be neglected because the inertia is already included in the Navier–Stokes equations (assuming that the BM has approximately the same density as the perilymph). It is also debatable whether the damping term can be excluded from (107) because this mechanical damping is probably much smaller than the viscous contribution from the Stokes boundary layers.

For the present three-dimensional model, the one-dimensional elastic force $k\eta$ has to be replaced by an equation for plate bending, such that we get

$$\frac{\partial^2}{\partial x^2}\left(D_{xx}\frac{\partial^2\eta}{\partial x^2}\right)+2\frac{\partial^2}{\partial x\partial z}\left(D_{xz}\frac{\partial^2\eta}{\partial x\partial z}\right)+\frac{\partial^2}{\partial z^2}\left(D_{zz}\frac{\partial^2\eta}{\partial z^2}\right)=-2p(x,0,z)+b\zeta. \tag{111}$$

It is common to assume that the bending stiffness of the BM is negligible in the axial direction, i.e. that $D_{xx} \ll D_{zz}$ and $D_{xz} \ll D_{zz}$. The dominant transversal stiffness of the BM is due to the microstructure of the BM which

contains stiff fibers embedded in a soft tissue matrix. All fibers are oriented in the z-direction. Based on Young's modulus for the fibers E_f and the fiber ratio f, we can estimate the transversal bending stiffness D_{zz} as

$$D_{zz} = \frac{f E_f I}{1 - \nu^2} \tag{112}$$

where $\nu = 0.3$ is Poisson's ratio and I is the area moment of inertia (Dr. J. H. Sim, personal communication).

At every time step, we have to solve the fourth-order differential equation

$$\frac{\partial^2 \eta}{\partial z^2} \left(D_{zz} \frac{\partial^2 \eta}{\partial z^2} \right) = -2p(x, 0, z) + b\zeta. \tag{113}$$

independently for each axial location x. This equation is effectively an ordinary differential equation which can be solved efficiently with a simple finite-difference discretization.

With respect to the flow simulation, the implementation of an active model corresponds to a modification of the boundary condition at the BM. The whole complexity of the nonlinear active BM model is therefore contained in a dynamic formulation of the boundary condition.

Alternatively, one could consider using the nonlinear feed-forward model by Lim & Steele (2002). This BM model uses a WKBJ approximation to the flow field based on a vector-potential formulation for the fluid displacement. It yields a pressure distribution along the BM which is used as an input for their description of the BM. In the present cochlear model, the pressure distribution along the BM comes directly from the fluid simulation.

In the nonlinear feed-forward model the force by the OHCs on the BM F_{BM}^C is assumed to be a feedback to the total force on the BM F_{BM},

$$F_{BM}^C(x + \Delta, t) = \alpha F_{BM}(x, t) = \alpha[2F_{BM}^f(x, t) + F_{BM}^C(x, t)], \tag{114}$$

where Δ determines the axial shift in the feed-forward mechanism, F_{BM}^f is the force exerted by the fluid on the BM and α is the feed-forward gain factor.

A simple implementation of this mechanism assumes that the feedback force by the OHCs is linearly proportional to the total BM force, i.e. that α is only a function of the location and independent of the amplitude and frequency of the excitation. However, in reality there exists saturation in the OHC force and α should not be treated as a constant.

In the nonlinear-feedback mechanism, the coefficient α is a function of the BM displacement as suggested in figure 17.3. Given that the time step size is small enough, it should be sufficient for our time domain simulation to use F_{BM} from the previous time step for approximating α for the new time step. This renders the discretized form of the nonlinear model linear.

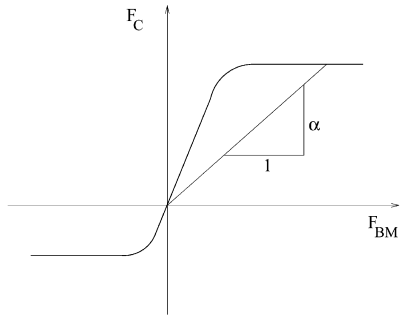

FIGURE 17.3. Relation of the OHC force F_C to the BM force F_{BM} and the definition of the amplification factor. Reprinted from Lim & Steele (2002) with permission from the publisher.

3. Possible improvements to the model

In order to improve the morphological representation of the cochlea, it is possible to modify the fluid domain with constant cross-sectional area to a domain with varying cross section either by the immersed boundary method (Beyer, 1992; Peskin, 2002; Givelberg & Bunn, 2003) or by using a grid with curvilinear coordinates. More realistic geometrical data of the fluid chambers can be obtained from μCT imaging of human temporal bones.

Similarly, the fluid-structure interaction between the flow and the basilar membrane can be implemented via the immersed boundary method. In the present formulation, the boundary conditions impose the BM velocity onto the fluid which responds with a pressure on the BM. In the immersed boundary method, the perilymph flow determines the displacement velocity of the BM. The right-hand side of the equation for the BM dynamics, e.g. Eq. (104c), yields a pressure jump. This pressure jump is translated into a field force which acts on the fluid such that the loop is closed.

These improvements for the present global cochlear model are the basis for Chapter 19 where we present a blueprint for the design of a virtual cochlea.

CHAPTER 18

Flow in the cochlea due to a rocking stapes

The common believe that the stapes stimulates the cochlear fluids in a piston-like transversal motion is inherent to several models of cochlear mechanics (e.g. Chapter 13 & 14). Recently, it has been found (e.g. Hato *et al.*, 2003) that the stapes motion contains also rotational components, i.e. tilting or rocking motions. Rocking motions have been observed about the long as well as the short axis of the stapes.

The relevance of these rocking motions are under debate. While a piston-like motion creates a net fluid displacement which has to be compensated by a displacement of the round window, the rocking motion does not necessarily lead to a flow throughout the cochlea. Therefore, it is suspected by some authors (e.g. Voss *et al.*, 1996; Decraemer *et al.*, 2007) that the rocking motions are unable to stimulate the BM significantly and that they are not relevant for the hearing process. Hato *et al.* (2003) and Decraemer *et al.* (2007), for instance, argue that the rocking of the stapes causes a forth and back movement of the fluid only in a small volume beneath the stapes footplate and that the generated pressure field does not propagate any further into the cochlea. However, there exists some experimental evidence that rocking motions of the stapes can create cochlear responses. Huber *et al.* (2008) measured compound action potentials (CAP) in guinea pigs for a prescribed rocking stapes motion and report that their CAP measurements suggest cochlear activity.

1. Numerical simulations of a rocking stapes motion

Edom *et al.* (2010*a*) performed numerical simulations to study the effect of rocking stapes motions[1]. For simplicity, a two-dimensional box model with a rigid basilar membrane was used (figure 18.1). The spatial extent of the box was varied to asses the influence of the cochlear geometry.

We consider the stapes to be sitting sideways on the scala vestibuli (cf. figure 1.5) such that the basal end of the basilar membrane is located at the wall

[1]Parts of this chapter have been taken from the conference paper by Edom *et al.* (2010*a*) and the associated poster.

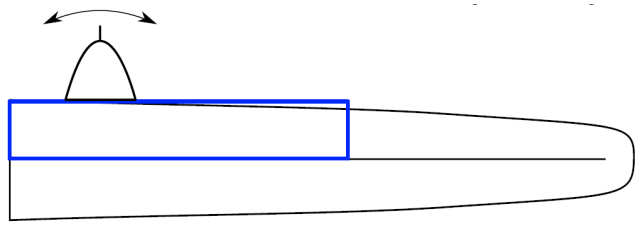

FIGURE 18.1. Configuration of the computational domain with the stapes location. Reprinted from Edom *et al.* (2010*b*).

opposite to the stapes. This configuration is different from many classical cochlear models which assume an axial position of the stapes (e.g. figure 14.1). It is closer to reality and, as we will show in the following, it is relevant to the rocking stapes motion.

It will be shown that the fluid flow induced by rocking movements of the stapes exhibits non-negligible velocity and pressure magnitudes throughout the computational domain. The flow field consists of thin viscous boundary layers and of a potential flow region. In these regions the velocity and pressure magnitudes exhibit different frequency dependence which can be explained with the classical theory of fluid flows. Furthermore, we will find that the geometry of the cochlea can promote higher velocity and pressure magnitudes in the vicinity of the basilar membrane. Possible consequences of the rotational stapes movement component on the hearing will be discussed at the end of this paper.

As outlined in section 17, we model the flow field of the perilymph by the Navier–Stokes equations. Because we assume a rigid BM, we impose zero velocity boundary conditions at the walls except at the location of the stapes. The stapes motion is modeled as an inflow which is imposed by Dirichlet boundary conditions for the velocity normal to the wall, i.e. we set

$$u_w(y) = \begin{cases} 2y/L_s \cdot \sin 2\pi f t & \text{for } |y| \le L/2, \\ 0 \quad \text{otherwise.} \end{cases} \tag{115}$$

As we have already explained in Chapter 17, it is not necessary to move the walls because the actual displacements are small. The error due to this formulation of the stapes motion is of order $(U_s/2\pi f)^2$ where f is the stimulation frequency with which the velocity amplitude oscillates harmonically between -1 and 1.

2. Flow field behind a rocking stapes

Figure 18.2 shows an instantaneous flow field which is generated by the rocking stapes with $U_s = 1.05 \times 10^{-4}$m/s and $L_s = 3$ mm. This velocity amplitude was reported by Sim *et al.* (2010) for a sound pressure level of 94dB (in the middle

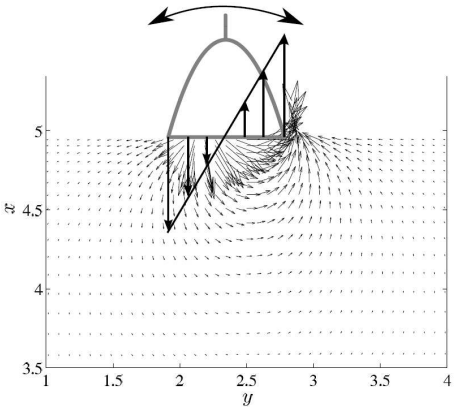

FIGURE 18.2. Snapshot of the velocity field in the vicinity of the rocking stapes. Reprinted from Edom *et al.* (2010*b*).

ear). The amplitudes of the velocity vectors in figure 18.2 oscillate simultaneously with the stapes.

A closer look at the velocity field shows that Stokes boundary layers form close to the walls. According to the theory for Stokes layers, their thickness scales with the viscous length scale $\sqrt{\nu/2\pi f}$. Outside these boundary layers the velocity field is nearly independent of the frequency. The velocity amplitudes decay approximately quadratically with increasing distance from the stapes (figure 18.3).

The Reynolds number based on the stapes length and velocity amounts to 0.35 such that we can safely neglect the influence of the nonlinear advective terms for the present analysis (which neglects the weakly nonlinear phenomena discussed in Chapter 16). Therefore, the vorticity $\zeta = \partial v/\partial x - \partial u/\partial y$ is governed by

$$\frac{\partial \zeta}{\partial t} - \frac{1}{Re}\nabla^2 \zeta = 0. \tag{116}$$

This is the Stokes equation formulated for the vorticity in the flow field. It is identical to a diffusion equation in which $1/Re$ plays the role of a diffusion coefficient. The rocking stapes has the role of a vorticity source which is introduced to the flow through the boundary condition

$$\zeta_w = -\frac{\partial u_w}{\partial y}. \tag{117}$$

We find that the stapes introduces a vorticity amplitude of $2/L_s$ along its footplate. At the edges of the footplate where the stapes velocity u_w drops rapidly to zero, the gradient $\partial u_w/\partial y$ is much higher and of opposite sign.

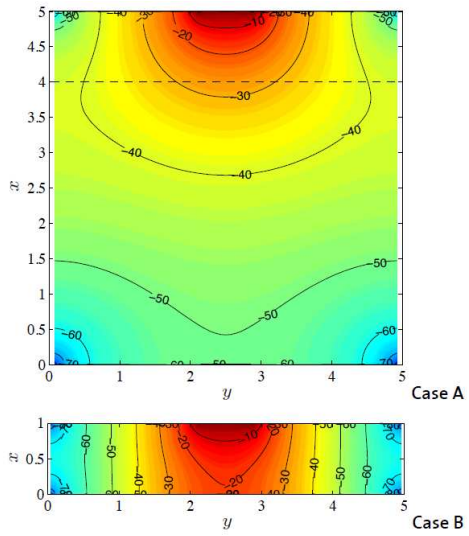

FIGURE 18.3. Magnitude of the velocity amplitudes (given in dB) for two different box geometries. Reprinted from Edom *et al.* (2010*b*).

The vorticity introduced by the rocking stapes penetrates into the flow field according to (116) such that the vorticity decays rapidly to zero with the dimensionless length scale $\sqrt{\nu/2\pi f}/L_s$. This length scale corresponds to the inverse of the Womersley number, Eq. (30), and shows that the vorticity boundary layer at the stapes corresponds to a Stokes boundary layer.

Outside the Stokes boundary layer the vorticity is exponentially small, such that we can assume an irrotational flow. Therefore, the bulk flow is governed by $\nabla^2\phi = 0$ where ϕ is the velocity potential. The time or the stimulation frequency do not appear explicitly in this equation. This explains why the velocity amplitudes in the bulk flow do not depend on the stimulation frequency. At the same time, the observation that the amplitudes decay quadratically with increasing distance indicates that the rocking stapes acts like a dipole source.

In the Stokes regime, the curves of constant pressure are perpendicular to the streamlines and coincident with the curves for $\phi = \text{const.}$. The pressure amplitudes are plotted in figure 18.4 where the centre of the stapes has been taken as a reference point with zero pressure. This distribution confirms that the rocking stapes has the character of a dipole source.

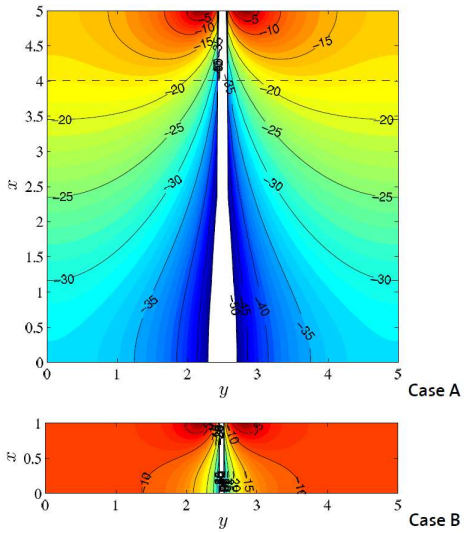

FIGURE 18.4. Magnitude of the pressure amplitudes (given in dB) for two different box geometries. The centre of the stapes footplate is used as the reference point with zero pressure. Reprinted from Edom *et al.* (2010*b*).

3. Relevance of the rocking stapes for the BM stimulation

Unfortunately, the pressure distribution shown is somewhat misleading for the interpretation of the results with respect to the stimulation of the basilar membrane. In order to estimate the BM stimulation, we have to consider the pressure difference across the BM. To this end, it is sensible to consider the pressure at the round window as reference pressure (which is close to atmospheric pressure). If we follow the scala tympani from the round window toward the helicotrema, the pressure remains nearly constant because the rocking stapes does create hardly any flow in these regions of the cochlea. This situation persists until we come close to the rocking stapes. Therefore, we obtain a better impression of the pressure difference acting on the BM, if we assume that the pressure at the right boundary of figure 18.4 is held constant and that the pressure field oscillates about this reference value.

The resulting pressure difference across the BM (using the results for geometry B) is highest at the base of the cochlea (about 0.3 Pa for a stimulus with 94 dB SPL at 1000 Hz). It remains approximately constant until the stapes footplate. Then it decays rapidly with about 20dB per stapes length. We conclude that significant signals from the rocking stapes can reach the basal end of the BM but

not any other parts of the BM. Thus, rocking stapes motion may be relevant for high frequency hearing which is consistent with the finding that rocking motions are most prominent at high frequencies (Voss *et al.*, 2000).

If we compare these results to pressure measurements for a piston-like stapes motion (Nakajima *et al.*, 2009) at the same sound pressure level in the middle ear, we find that the pressure signal at the BM from the rocking stapes is about 30dB weaker than for the piston-like motion.

It should also be noted that the presented results can be of relevance for a condition known as round window atresia which indicated that the round window is rigid such that no net fluid motions are possible. Excluding secondary phenomena which allow a leakage of perilymph (leading to so-called 'cochlear compressibility'), the round window atresia does not allow any stapes movement other than rocking. The findings of Linder *et al.* (2003) indicate that round window atresia does not lead to a total conductive hearing loss. The results presented in this chapter may be an explanation for this observation.

Finally, we would like to emphasize the relevance of the position of the stapes. We have seen that a rocking stapes acts in the far field like a dipole. Comparisons between the cochlear flow due to a monopole and a dipole source have been performed by Pozrikidis (2008). Unlike a monopole source (e.g. a piston-like motion) which is point symmetric, a dipole has a principal axis. In our case, the stapes sits sideways on the scala vestibuli (cf. figure 1.5) such that the dipole principal axis is oriented along the main axis of the cochlea. The results would be different, i.e. the signal on the BM would be weaker, if the stapes was located at the basal end of the cochlea as it is done in most cochlear models.

CHAPTER 19

Blueprint of a virtual cochlea

In this chapter, we propose the design of a *virtual cochlea*, i.e. a comprehensive three-dimensional model including several simulation modules describing the functional units (e.g. flow simulation, structural simulation, model for OHC motility) in a global context. This chapter has to be understood as a blueprint of a cochlear model that has yet to be realized in practice.

The virtual cochlea shall enable the study of the tight interplay between various local components and phenomena. From the point of view of the researcher in mechanics of hearing, the distinctive features of the virtual cochlea are:

- simulation in the time domain (transient acoustic stimulations)
- high morphological fidelity for the whole cochlea (including a detailed representation of the Corti organ)
- modeling of the OHC motility (active processes)
- inclusion of a wide range of physical flow phenomena (e.g. acoustic streaming) by solving the full Navier-Stokes equations
- modular software approach to allow easy comparison of different models for sub-systems

Wherever possible, the simulation modules solve governing equations which are based on first principles (e.g. Navier–Stokes equations for the fluid simulation). The governing equations are solved in the time domain to allow the simulations of transient phenomena.

The virtual cochlea is designed for next-generation Petascale-supercomputers which require extreme levels of computational parallelism. The parallelization strategy for the virtual cochlea puts the primary focus on the homogeneity of the numerical algorithm rather than on the reduction of floating point operations. This strategy is unconventional and addresses current developments in supercomputing architectures which go toward larger and larger numbers of parallel processing units.

Cochlear mechanics has to be understood as a multi-scale and multi-physics problem. Typical length scales of different physical systems involved in cochlear mechanics are illustrated in figure 19.1. The involved physical sub-systems are treated in separate simulation modules which are tightly coupled according to

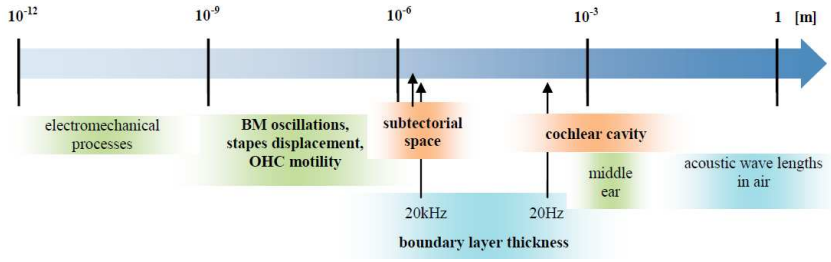

FIGURE 19.1. Range of spatial scales in the mechanics of hearing.

figure 12.1. In the following, we will explain the multi-physics and multi-scale aspects in detail and will explain which methods will be used to realize the virtual cochlea.

1. Multi-physics simulation framework

There will be three primary simulation modules: (a) flow simulation, (b) structural simulation, and (c) a simulation of the active processes. The flow fields and the structural dynamics will be spatially and temporally resolved. The mechanisms leading to OHC motility are at a cellular scale which will not be spatially resolved. Therefore, the OHC motility will be modeled as a zero-dimensional lumped-parameter model, i.e. the nonlinear dynamics of the OHCs will be described as a set of ordinary differential equations which are integrated in time.

These three simulation modules are coupled though the immersed boundary (IB) method (Peskin, 2002) which results in field forces for the flow simulation and OHC model and in boundary- or interface conditions for the structural simulation. The immersed boundary method (IB) has been shown to be suited very well for modeling fluid-structure interactions (FSI), in particular, in a biomedical context (e.g. De Tullio *et al.*, 2009). IB has even been used before to simulate the perilymphatic flow within the cochlea (Beyer, 1992; Givelberg & Bunn, 2003).

2. Multi-scale approach

The resolution requirements for the flow simulation are dominated by (a) the size of the smallest flow structures and (b) the smallest morphological scales of the flow domain. The pulsating flow in the cochlea develops viscous boundary layers which are similar to Stokes boundary layers. Their thickness scales with the inverse square root of the frequency. From this we can estimate that the smallest flow structures have a typical size of 100 to 1μm for stimulation frequencies between 20 and 20 000Hz. The smallest morphological scales in the cochlear fluid spaces can be found in the Corti organ (OC) where the narrow gap beneath the

tectorial membrane (cf. figure 1.6) has a width of only a few micrometers. To resolve the flow in this gap, we need at least a few grid points. Therefore, we require a grid spacing of less than 1μm in the Corti organ, but in the rest of the cochlea we can use a larger grid spacing. Instead of using a very fine submicrometer mesh throughout the whole cochlea, we split the flow problem into two domains: a large-scale domain and a small-scale domain.

The large-scale flow simulation computes the flow field in the scalae vestibuli, tympani and media except for the flow within the Corti organ. It includes also the interaction of the fluids with the oval and round windows, with the tectorial membrane, the basilar membrane and Reissner's membrane (cf. figure 1.6). The small-scale simulation models the flow in the whole organ of Corti.

Based on our current understanding of the anatomy there is no direct interface between the fluid within the Corti organ and the endolymph in the scala media. We are aware though that such a connection might exist through a thin gap at the edge of the tectorial membrane which is called 'marginal zone' in Lim (1980). In that case, we can couple the two domains via a penalization method which leads to an embedded grid approach. The penalization method is directly related to IB and fits in nicely with the algorithms used for the FSI.

3. Cochlear morphology - computational model

The virtual cochlea requires a detailed description of the cochlear morphology. In the flow simulation, the morphology defines the location of the field forces used in the IB method. In the structural simulation, it defines the shape of the simulated components.

The overall cochlear shape is given by the bony cavity of the cochlea in the temporal bone. Such data is available, for instance, in the form of μCT data of a human temporal bone (cf. picture on the title page). The internal structures (membranes, Corti organ, etc.) can be taken from data in the literature (e.g. Dallos *et al.*, 1996) and histological sections (e.g. using the morphological model from the Eaton-Peabody Laboratory of Auditory Physiology, 2008).

First, the morphology is to be defined on the basis of cochlear cross-sections from the basal end to the apex. In each of these cross-sections the relevant structures (e.g. membranes) are parametrized through manual segmentation. Thereby, each cross-section is split into a structural part, a large-scale flow domain and a small-scale flow domain. This process is illustrated in figure 19.2. The segmented partial cross-sections are then connected to the neighboring cross-sections to yield three-dimensional morphological definitions of the separate simulation domains.

The definition of the mechanical properties for the fluids is straightforward as they are well established in the literature (e.g. Bronzino, 1995). The mechanical properties of the tissue are not so clear. Here, we can use mechanical properties

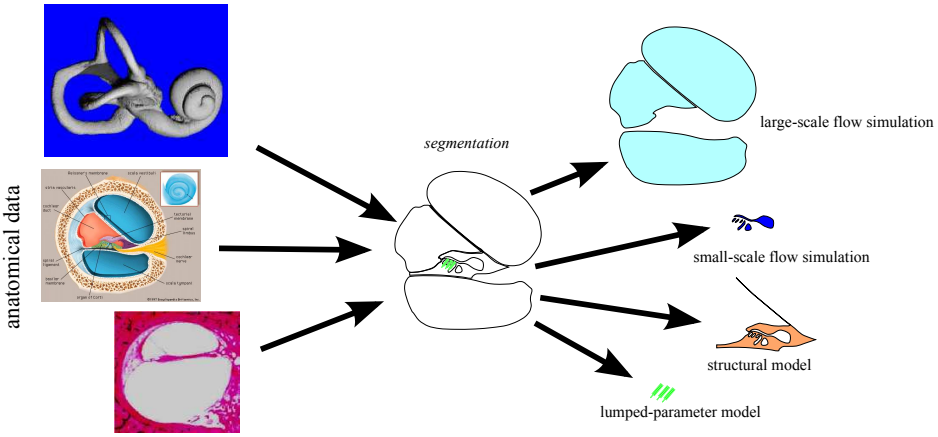

FIGURE 19.2. Generation of the computational model(s) by segmenting anatomical data.

used in other established models (e.g. Baumgart *et al.*, 2009; Steele *et al.*, 2009) although most of these have been designed for animal cochleae.

4. Flow simulation

The flow simulation carries the main burden of the computational work. As noted above, the fluid simulation is split in two: a large- and a small-scale flow simulation. These two simulations do not have a common interface but are tightly coupled through force fields to the structural simulation to reflect the FSI.

4.1. Numerical method for the flow simulation. Although the large- and small-scale flow simulations address systems with different principal roles in cochlear mechanics and different length scales, we can use the same numerical approach for both simulations. As we will explain further below, a detailed and accurate simulation of the hydrodynamics within the cochlea is computationally very expensive. As of today, it cannot be carried out with generally available flow solvers. Therefore, we should use high-order Navier-Stokes solvers such as the code IMPACT (Henniger *et al.*, 2010) which is optimized for massively-parallel supercomputers and is arguably currently the fastest simulation code of its kind. IMPACT uses high-order finite differences on a staggered grid for the spatial discretization of the Navier-Stokes equations and semi-implicit or high-order explicit time integration schemes. The Poisson equation for the pressure is solved with a multigrid method. The work is distributed to different processing units by a domain decomposition of the Cartesian grid in all three directions. Performance tests have shown that problems with more than 100 billion grid points can be

solved efficiently with this code on computers with 22 000 processing units (Cray XT5 at the Swiss Supercomputing Centre CSCS) without any problems.

4.2. Structured mesh for flow simulation. The two flow domains are immersed into two three-dimensional rectangular boxes with uniformly spaced Cartesian grids. The grid spacing for the large-scale simulation is dominated by the viscous length scale $\sqrt{\nu/2\pi f}$ which yields a typical length scale for the thickness of the Stokes boundary layers in the cochlea based on the kinematic viscosity ν and the frequency f. For stimulation frequencies of a few kilohertz, we will need a grid spacing between 1 and 2μm. The box for the large-scale simulation has the dimensions of approximately 1mm $\times$ 1mm $\times$ 35mm leading to about 10 billion grid points. The resolution for the small-scale simulation which contains the OC is mainly determined by the scales of the structures themselves. The narrow gap beneath the TM has a width of only a few micrometers. Therefore, we need a resolution of about 0.5μm. This will lead to another 10 billion uniformly spaced grid points in the small-scale simulation used to resolve a box of 0.3mm $\times$ 0.1mm $\times$ 35mm enclosing the whole OC. We immerse the segmented cochlear cross-sections into these meshes such that the cross-sections are parallel to each other. This conforms to the Cartesian grid of the underlying flow simulation, but neglects the coiling of the cochlea. We believe that an uncoiled morphology will be sufficient to study the most relevant physics of cochlear mechanics. Nevertheless, we maintain the option of modeling a coiled cochlea by slightly tilting the cross-sections against each other. This process results in a curvilinear orthogonal grid for which we can use the same simulation code if we add some metric terms at relatively little cost.

4.3. Fluid-structure interaction through the immersed boundary method. The immersion of the flow domains into the structured Cartesian grids of the Navier-Stokes solver is realized according to the IB method via field forces (Peskin, 2002), i.e. we choose the field forces $\mathbf{f}(x, y, z, t)$ in the Navier–Stokes equations,

$$\frac{\partial \mathbf{u}}{\partial t} + (\mathbf{u} \cdot \nabla)\mathbf{u} = -\nabla p + \frac{1}{Re}\nabla^2 \mathbf{u} + \mathbf{f}, \tag{118}$$

such that the flow velocity vector $\mathbf{u}(x, y, z, t)$ takes the desired values at the walls (e.g. zero velocity at rigid walls). The appropriate choice of these field forces is best explained in the context of a fluid-structure coupling. Here, we can choose the field force $\mathbf{f}$ to be equal to the force exerted by the structure onto the fluid. If we model a compliant wall by a spring, for example, we can apply the spring force $F = kx$ to the flow. Because the wall or the interface to the structural component lies, in general, not exactly on a grid line of the structured flow grid, we have to distribute the force F to the grid points in the immediate neighborhood of the wall, i.e. the force field $\mathbf{f}$ will be mostly zero except in the vicinity of the walls.

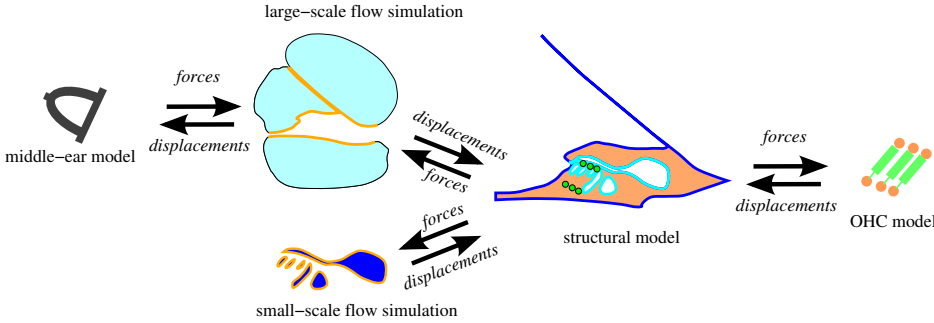

FIGURE 19.3. Implementation of multi-physics concept by coupling the simulation modules through forces and displacements: fluid (blue), structures (amber), OHC motility (green).

Figure 19.3 illustrates this coupling concept and shows that the forces F for the two flow simulations will come from the structural simulation. Whereas the small-scale simulation is completely enclosed by the structural model, the domain of the large-scale flow simulation is also bounded by bony walls and softer tissue behind the stria vascularis (cf. figure 1.6). The forces for these outer walls of the cochlea come from lumped-parameter models.

5. Structural Simulation

The membranous structures within the cochlea (Reissner's membrane, basilar membrane, round window) can be modeled with finite shell elements. For the other structural components, we propose to follow the finite-element approach used by Steele *et al.* (2009) in their multi-scale model of the OC.

This approach to structural modeling integrates well with the IB method for the fluid-structure coupling. The computational effort required for the structural simulation is small compared to the fluid simulation because (a) most structures are thin and can be modeled by two-dimensional shell elements leading to much fewer degrees of freedom than in the flow field (approximately 10 million elements), and (b) the governing equations are integrated in time with an explicit scheme such that no systems of equations have to be solved. The fluid simulation and the lumped-parameter models for the OHCs will yield the displacements and velocities at the interfaces to the fluid and to the OHCs, respectively. The structural simulation returns the forces at the fluid-structure interfaces to the fluid via IB to complete the coupling loop (figure 19.3).

The finite-element model defines equations of the form

$$\mathbf{M}\ddot{\mathbf{x}} + \mathbf{R}\dot{\mathbf{x}} + \mathbf{K}\mathbf{x} = \mathbf{F}$$

where $\mathbf{M}$, $\mathbf{R}$, and $\mathbf{K}$ are the mass, damping and stiffness matrices, respectively. The vector $\mathbf{x}$ contains the displacement of all structural nodes. It can be split into a vector of boundary or interface nodes $\mathbf{x}_b$ (interfaces to the fluid or OHCs) and a vector of the 'inner' nodes $\tilde{\mathbf{x}}$. The displacements of the boundary or interface nodes $\mathbf{x}_b$ come directly from the flow simulation and the OHC model (cf. figure 19.3). The reduced equation for the inner nodes can be advanced explicitly by one time step. This yields the new forces at the boundary nodes which are then returned to the flow simulation.

6. Lumped-parameter models

The virtual cochlea requires lumped-parameter models for: (a) the active processes in the OC, i.e. OHC motility; (b) the middle-ear mechanics which yields the displacements for the oval window, i.e. the acoustic input for the virtual cochlea; (c) the outer bounds of the cochlea, i.e. the bony walls of the cochlear ducts and the supple walls at the stria vascularis (cf. figure 1.6).

The lumped-parameter models are given as ordinary differential equations which are integrated in time together with the other simulation modules. These equations are not directly coupled to each other, i.e. there is a separate model at each location (e.g. at each OHC).

6.1. OHC motility. The active processes in the OC are highly relevant to a properly working cochlea. We follow the concept of Kern & Stoop and model the dynamics of the outer hair cells as a nonlinear oscillator which exhibits a Hopf bifurcation (e.g. Stoop & Kern, 2004; Kern, 2003; Kern & Stoop, 2003). Each OHC is modeled by a separate differential equation. These equations are coupled to the simulation framework trough the forces acting on the OHCs (from the structural simulation). The resulting displacements are handed back to the structural simulation. We have outlined the details of this modeling approach in Chapter 15 and have tested it successfully in the context of a transient inviscid model of the perilymphatic flow by reproducing established nonlinear phenomena such as distortion products (e.g. figure 15.2).

6.2. Middle-ear mechanics. The middle-ear mechanics is modeled because we need a dynamic description for the stapes displacement at the oval window. We propose to use a straightforward model which describes the basic characteristics of this dynamical system (e.g. Kringlebotn, 1988). The input to this model is the acoustic stimulation of the virtual cochlea and the output yields the displacement of the oval window.

6.3. Outer bounds of the cochlea. We model the outer bounds of the cochlea (large-scale model) by local (visco-)elastic models of the form $F = kx + rv$ where x is the displacement of the wall, v is the displacement velocity (equal to

the fluid velocity at this location) and k and r are spring and damping constants, respectively. These constants have to be chosen such that these boundaries of the large-scale flow simulation behave like 'walls'. For the bony walls, we have to choose a relatively large spring constant k to make them stiff (at least an order of magnitude stiffer than the stiffest part of the BM). For the stria vascularis, we can use a large damping coefficient r and a moderate stiffness k.

7. Time integration

The computational cost for the virtual cochlea depends not only on the spatial discretization (i.e. the grid size) but also on the time step size. There are two inherent limits for the time step size: the first and most natural limit is the temporal scale of the acoustic signals, i.e. each oscillation has to be resolved by at least a few time intervals. Stimulation frequencies of 10 kHz, for instance, require a time step size on the order of 10^{-5} **s**. The second limit is determined by numerical stability. A rough estimation of the Courant-Friedrichs-Levy criterion indicates that the necessary time step for a stable simulation on the intended grids is larger than the limit imposed by the acoustic signal. The stability limit due to the viscous term in the flow simulation imposes a limit of about 10^{-7} **s**. A further limitation comes from the FSI through IB where stiff structures (e.g. rigid walls) limit the time step. Givelberg & Bunn (2003) report a time step size of 10^{-8} **s** due to the rigid walls of their cochlear ducts. Such limitations can be mitigated by accepting 'softer' bony walls which should still give acceptable results as long as the bone stiffness is sufficiently larger than the stiffness of the BM. On the numerical side, we have the possibility of implementing the most rigid structures with a direct velocity forcing method proposed by Fadlun *et al.* (2000) or an immersed interface method (Leveque & Li, 1994). Furthermore, we can increase the time step limit by using a semi-implicit time stepping. Detailed performance studies (Henniger *et al.*, 2010), however, have shown that, in many cases, purely explicit time integration is more efficient overall. Whether this is the case for the virtual cochlea will have to be investigated. From the current point of view, we expect to be able to use an explicit time stepping scheme (e.g. third-order Runge-Kutta) with a time step of approximately 10^{-8} **s**.

8. High-performance computing

The computational efficiency of the proposed numerical approach is inherently tied to the homogeneity of the structured grid for the flow simulation. This homogeneity is maintained by representing the cochlear morphology with the IB method. The major drawback of IB is the waste of grid points in those regions of the computational domain which are 'behind the walls'. Similarly, we may have over-resolved regions in the flow field (e.g. in the core region of the scalae

vestibuli and tympani) where we will spend more effort than necessary for resolving the local flow structures. These two problems could of course be overcome by using an unstructured grid which places the grid points only where needed leading to one to two orders of magnitudes fewer grid points. Nevertheless, we still opt for a structured Cartesian grid for the following reason: the intended scale of the simulations will be so large that the use of supercomputers is imperative regardless whether we use a structured or a body-fitted grid. To be able to use such computing platforms efficiently, the problem has to be distributed to many different processors while maintaining an equal load on all processors (load balancing). This is facilitated by structured grids for which a homogeneous data distribution is natural and the communication remains mostly local between neighboring domains. Furthermore, the performance per processor is higher for structured meshes because of its cache-friendly data structure. In summary, we estimate that the apparent advantage of body-fitted grids is easily offset by the high computational efficiency of structured grids with IB.

With the current trends in supercomputing it will become increasingly important to use straightforward and homogeneous numerical methods which can be easily parallelized, rather than intricate schemes which may reduce the computational expense locally but prevent the parallelization at a global scale. Or in more practical terms: we should always accept a few more grid points if we obtain a homogeneous numerical method in return, because there will be enough aggregate computational power to pay for the additional grid points if (and only if) we are able to parallelize the method.

Based on the expected development of supercomputing, the virtual cochlea is expected to be able to use on the order of 200 000 parallel threads which results roughly in 100 000 grid points per thread for the flow simulation and 10 000 elements per thread for the structural model. Such a parallelization scheme should result in a simulation turn-around of a few days or less even for large transient simulations. To make early simulations more efficient, coarser meshes can be used which will also allow larger time steps. This can be achieved by limiting the maximum stimulation frequency.

9. How can the virtual cochlea be used?

The virtual cochlea is a test bench for confirming or dismissing hypotheses on physical processes in the cochlea as they are listed in Chapter 12. We can run virtual experiments and measure different quantities resolved in space and time. This is typically impossible in vivo because of the poor accessibility of the cochlea.

For example, we can use the virtual cochlea to test Lighthill's hypothesis on IHC stimulation (Lighthill, 1992). Such an in silico experiment is quite straightforward: we stimulate the virtual cochlea with a harmonic acoustic signal and

then inspect the resulting flow field for a steady streaming around the IHC. These results can be put in context with existing studies for the local flow about hair bundles (e.g. Kozlov *et al.*, 2011). This analysis will be done first for a continued harmonic stimulation. Second, we can use the virtual cochlea to investigate the involved mechanisms also for transient stimulations (e.g. clicks) for which it will be especially interesting to see how the nonlinear active processes in the cochlea support our transient hearing. We expect to observe phenomena which cannot be studied with state-of-the-art models operating in the frequency domain, because the transient dynamics in an active cochlea must not be modeled as a superposition of results for harmonic stimulations. These in silico experiments shall help us to get a detailed understanding of the mechanisms involved in the transduction of transient acoustic signals toward stimulated IHC.

Furthermore, the multi-scale character of the virtual cochlea will allow us to study the different kinds of 'hidden waves' (De Boer & Nuttall, 2009) which are likely to be present simultaneously at different scales within the cochlea. This will also help us to investigate the process leading to 'reverse traveling waves' which are responsible for transmitting otoacoustic emissions toward the oval window.

Last but not least, the virtual cochlea will yield detailed pressure fields in the cochlear ducts. Such pressure fields can be studied with respect to the mode of stimulation, i.e. whether we stimulate the cochlea through different stapes movements, through bone conducted waves, or through artificial intracochlear actuators. The measurement of intracochlear pressure fields is also the subject of several experimental campaigns (e.g. Nakajima *et al.*, 2009) such that in vivo reference data is available. In the long run, a deeper understanding of the pressure distribution in the cochlea is of interest for the development of new generations of hearing aids.

Part 3

Coupled phenomena

CHAPTER 20

Scale separation in the inner ear

So far, we have treated the different sensors of the inner ear separately. This is also the typical approach used in most other studies: Investigations on the hearing sense concentrate on the cochlea and neglect the vestibular side of the inner ear, whereas the SCCs are studied without considering the cochlear cavity. Likewise, the otolithic organs are typically treated as an isolated organ although the utricular maculae is immersed in the endolymphatic fluid space of the SCCs.

There are several good reasons (that we shall discuss in the following) which justify the separate treatment of the different organs. At the same time, some important effects are then lost and it is not possible to study interactions between the sensors. Such interactions can be regarded as *sensory crosstalk* which indicates that the organs may be sensitive to primary stimulations of the neighboring organ, e.g. stimulation of the SCCs by sound (Tullio's phenomenon). Such crosstalk between the sensors of the inner ear are well documented and are discussed in the overview article by Halmagyi *et al.* (2005).

Before we look at two examples for sensory crosstalk in chapters 21 & 22, we discuss here the reasons why a separate treatment of the sensors of the inner ear can be successful anyway (as long as one is not specifically interested in crosstalk phenomena). The first and most obvious reason is the spatial separation of the cochlea and the balance sense. This separation goes along with the different primary fluid spaces of the organs: whereas the basic physiology of the SCCs can be explained with an endolymph flow alone, the simpler cochlear models only consider the flow in the perilymph. For the otoliths, the presence of fluids is typically neglected at all.

At a closer look, it becomes clear that these two reasons (spatial separation; different fluid spaces) fall short of fully explaining the separation of the basic functionality of the different organs. Even though the organs might be separated into endolymphatic and perilymphatic flow in different parts of the inner ear, the fluid spaces of the different sensory organs are mechanically connected through the thin membranes surrounding the endolymphatic fluid space. In general, this membrane is so supple that it can move freely with the fluid in the normal direction. It has no effect on the fluids other than imposing a no-slip boundary condition. Therefore, the distribution of the tangential shear stress across

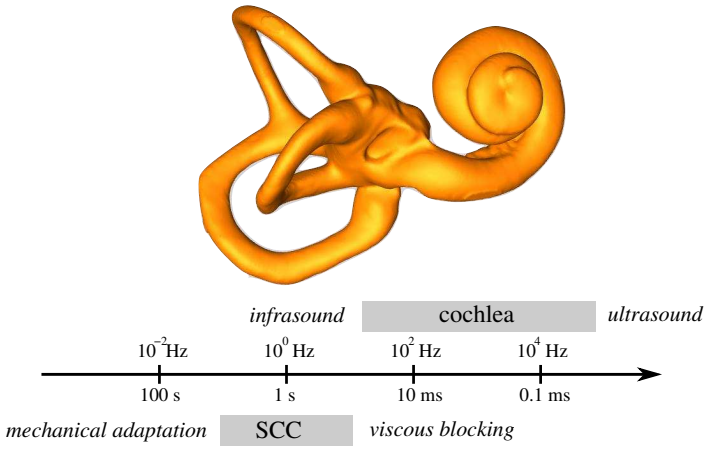

FIGURE 20.1. Temporal scale separation between the cochlea and the SCCs.

the membrane does not have to be continuous. The fluid pressure, however, is transmitted across the membrane and therefore has to be continuous across the membrane. The latter property is somewhat more complicated across the basilar membrane whose stiffness is not negligible such that there is a pressure jump across the (deflected) basilar membrane.

We see that the two fluid spaces are tightly coupled because the membranous labyrinth is a supple structure. Moreover, the argument of the spatial separation of the SCCs and the cochlea is rendered moot if we consider that the stapes is located in the middle between these two organs and one might even conjecture that a vibrating stapes has a direct effect on the utricular macula since the utricle is located just as close to the stapes as the base of the basilar membrane.

These considerations leave us now with the question why it is possible at all to study the organs separately. The answer to this question can be found in the dominant time scales of the organs. As we have discussed in chapter 2, the operative range of SCCs is limited by the viscous time scale $T_v = O(10^{-1}\text{s})$ and the cupula time scale $T_c = O(1 \ldots 10^{1}\text{s})$. These time scales are large with respect to the time scales of the cochlea which operates at frequencies from 20 to 20 000Hz. At these acoustic frequencies, the endolymph flow in the slender SCCs is strongly damped as we can see from the higher duct modes in figure 4.1. Vice versa, the cochlea is insensitive to slow stimulations.

We conclude that there exists a clear temporal scale separation between the balance sense and the hearing (figure 20.1). The vestibular system operates on the slower time scales, whereas the dynamics of the cochlea is governed by fast processes.

CHAPTER 21

Tullio's phenomenon and superior canal dehiscence

There exist certain conditions under which the vestibular system responds to acoustic stimulations (Halmagyi *et al.*, 2005). Here, we will discuss a specific form of this sensory crosstalk which leads to a sensation of angular motion when a sound is heard. Sound-induced vertigo has been known since the experiments of Tullio (1929) on pigeons. Therefore, this phenomenon is commonly known as *Tullio's phenomenon*. Tullio's phenomenon has been connected to a specific anatomical defect which is known as superior canal dehiscence (SCD). The SCD denotes a hole in the bony wall of the inner ear which connects the vestibular system to the cranial cavity.

The sensation of angular motion in Tullio's phenomenon is related to a stimulation of the superior semicircular canal. This stimulation implies that there exists a net fluid flow in the superior canal which deflects the cupula and excites the hair cells. This brings us to the intriguing question of how a purely oscillatory acoustic stimulation can generate a directed flow. At first glance, such a phenomenon is completely unexpected because the flows in the inner ear are usually assumed to be governed by the linear Stokes equations (Chapter 6). From a mathematical point of view, a transfer of acoustic energy into a directed flow is only possible through a nonlinear process. In the context of the acoustic stimulation, the nonlinear phenomenon of acoustic streaming (Chapter 16) is a natural candidate for such a process. Because the inner ear contains compliant walls which separate the fluid spaces, there exist also intricate fluid-structure interactions which could be responsible for Tullio's phenomenon.

In the following, we will outline a mechanical model for Tullio's phenomenon. Without being able to provide any conclusive results, this chapter provides a guideline for the research on the mechanisms of Tullio's phenomenon.

We begin our investigation with a brief review on the superior canal dehiscence (§ 1) which is apparently a relevant factor in Tullio's phenomenon. In the following, we will study the characters of the endolymphatic and perilymphatic flow fields (§ 2). We will find that the two flows are fundamentally different even though both flows are in a low-Reynolds-number regime. Therefore, our model

of Tullio's phenomenon will consist of different formulations for the endolymph and the perilymph. At the same time, these two separate formulations have to remain tightly coupled to represent the mechanical interaction across the walls of the membranous labyrinth. In section 3, we discuss different nonlinear mechanisms which may be involved in Tullio's phenomenon. This will lead us in § 4 to a hypothesis for a mechanism which involves traveling waves in the SCC. We conclude this chapter by outlining in section 5 the design of a numerical model for studying the proposed hypothesis.

1. Superior canal dehiscence

Many vestibular responses to sound are related to the condition of superior canal dehiscence. The dehiscence of the superior semicircular canal is an anatomical defect of the bony labyrinth (prevalence of about 1%; Carey *et al.*, 2000). It is a hole in the bone surrounding the superior semicircular canal which opens to the cranial cavity (cf. figure 1.3). This hole is covered by the dura mater (tissue layer enclosing the central nervous system). From a mechanical point of view, this hole is similar to the round window of the cochlea (cf. figure 1.2). Therefore, it is often called 'third window' of the inner ear.

Minor *et al.* (1998) was the first to relate this dehiscence to sound- and or pressure-induced vertigo. Carey *et al.* (2004) presented a detailed study of acoustic responses of vestibular afferents for chinchilla with SCD. Since Minor's publication in 1998, the superior semicircular canal dehiscence (SCD) enjoys a lot of attention from the scientific community and several other effects have been related to SCD. Songer & Rosowski (2010), to name just one of the most recent publications, investigated effects of SCD on the hearing: they reported a hypersensitivity to bone-conducted sound and a decreased sensitivity to air-conducted sound (increased air-bone gap) in chinchilla with SCD. Moreover, they were able to revert this effect by re-patching the dehiscence. This supports the common understanding that these phenomena are directly related to the presence of a hole in the bony labyrinth. Hypersensitivity due to SCD is not only known for bone-conducted hearing but also for the otolithic function (e.g. Manzari *et al.*, 2011).

SCD is a good example for the complex systemic nature of the inner ear. This complexity is probably also the reason why mechanical models and/or explanations for the clinically observed phenomena are relatively sparse (e.g. Songer & Rosowski, 2007). In particular, our understanding of the underlying mechanical processes which are responsible for transducing an acoustic signal to a vestibular signal (Tullio's phenomenon) remains very vague. Only a few basic mechanisms related to SCD are illustrated, for instance, in Minor *et al.* (1998).

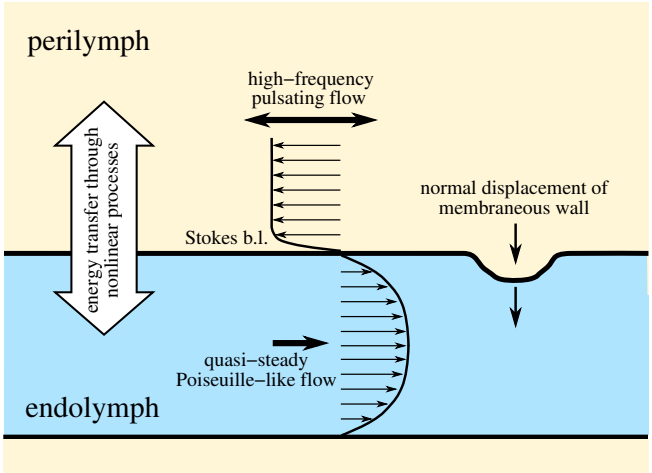

FIGURE 21.1. Sketch of the endolymphatic and perilymphatic flow regimes and their interaction through the wall of the membranous labyrinth.

2. Properties of the lymphatic flow fields

The medium between the oscillating stapes and the endolymph of the SCCs is the perilymph. It is separated from the endolymph by the compliant walls of the membranous labyrinth. Therefore, any sensible mechanical model of the coupling between sound stimulation and vestibular responses must not only include a representation of the endolymphatic flow field but also of the perilymphatic flow and the membranous labyrinth.

We have seen in Chapter 20 that the cochlea and the SCC are separated by their dominant time scales (cf. figure 20.1). This time scale separation is reflected in the character of the endolymphatic and the perilymphatic flow fields: In the slender ducts of the endolymphatic fluid space we find Poiseuille-like flow profiles which are characteristic for slow processes, i.e. for small Womersley numbers. The velocity profile of the perilymph in the scalae vestibuli and tympani features thin Stokes boundary layers typical of high Womersley numbers. With the SCD acting as a third window, there is also a perilymphatic flow in the bony labyrinth. It is to be expected that this pulsating flow exhibits the same Stokes boundary layers as in the cochlea.

Figure 21.1 illustrates these properties of the two lymphatic flows. It also suggests that the two flows can communicate through displacements of the membranous wall.

3. Nonlinear mechanisms

The inability of linear systems to transfer energy between the slow processes in the SCC and the fast dynamics of the cochlea (and vice versa) tells us that Tullio's phenomenon involves nonlinear mechanisms. Acoustic streaming is a prominent example of such a nonlinear mechanism (Chapter 16). It translates small oscillatory ('acoustic') fluid motions into a steady directed flow ('streaming'). Mathematically, this is only possible if we consider the full Navier–Stokes equations which contain nonlinear terms.

A further candidate for the nonlinear mechanics can be found in impedance pumps (e.g. Thomann, 1978; Avrahami & Gharib, 2008). It is known that a directed net flow can be generated inside a torus by periodic squeezing at one location. This effect is possible if the wall compliance is varied along the torus axis and if the squeezing location is asymmetric with respect to the compliance distribution. The necessary variation in the compliance of the SCC is given by structures like the cupula or the utricular macula and by variations in the cross-section (ampulla, utricular cavity). Furthermore, the third window of the SCD creates an strong impedance variation which could promote an impedance pump mechanism in the SCC. It should be noted, however, that the impedance pumps described in the literature typically operate a much higher Reynolds numbers than in our problem.

Of course, there are also other nonlinear phenomena present in the inner ear which may transfer energy between different time scales. These are, for instance, the dynamics of the OHC in the Corti organ (Chapter 15) or nonlinear mechanical behaviour of the deformed tissue either due to a nonlinear constitutive law or due to large deformations. Whereas the former phenomenon is known to be very relevant in cochlear mechanics (e.g. distortion products in figure 15.2), it is unlikely to cause any measurable effect in the SCCs. The latter phenomena are expected to be weak as well because the deformations of the membranous walls are very small. Here, we will focus primarily on fluid mechanical effects and on nonlinearities introduced through the fluid-structure coupling.

4. Traveling wave hypothesis

The nonlinear mechanisms listed above invariably involve displacements of the membranous walls. This leads use to the following hypothesis for the coupling mechanism between the vibrating stapes and an endolymph streaming: First, we assume that the stapes stimulates a rapidly pulsating perilymph flow. Because of the SCD ('third window') this perilymph flow does not only exist within the cochlea but also in the SCC. By a mechanism similar to the one in the cochlea, the perilymph will initiate traveling waves on the membranous wall inside the SCCs. These traveling waves are then expected to lead to a streaming endolymph flow,

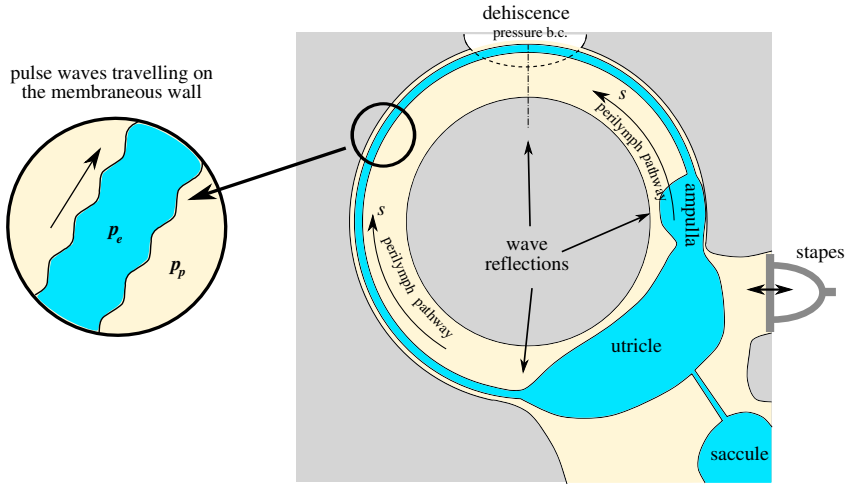

FIGURE 21.2. Schematic of the configuration of the numerical model with the fully-resolved endolymph flow (blue) and the perilymph (yellow) which is directly stimulated by the stapes. The inset on the left shows traveling pulse waves on the membranous walls due to differences between the perilymph pressure p_p and the endolymph pressure p_e.

e.g. by an impedance pump mechanism (Thomann, 1978; Avrahami & Gharib, 2008), through acoustic streaming (Lighthill, 1992) or even by straightforward peristalsis.

An important element in this hypothesis is the traveling wave in the SCC. These waves are the result of the interaction between the walls of the membranous labyrinth and the pulsating pipe flow. The configuration is quite similar to the situation in the cochlea except that the round window is replaced by the SCD and that the basilar membrane is replaced by the membranous duct (figure 21.2). In the following, we discuss the character and the modeling of these traveling waves.

4.1. Compliant walls for the membranous labyrinth. In order to obtain traveling waves, we have to allow small wall displacements due to an excess pressure in the endolymph. We use a very simple model for this displacement which is also used in the basic theory for the pulse propagation in arteries (Pedley, 1980). To this end, we introduce the distensibility D of the membranous duct. The distensibility D is defined as the relative change of the area A_e (e.g. the cross-section or lumen of the membranous duct) due to a pressure increase, $\mathrm{D} = A_e^{-1}(\mathrm{d}A_e/\mathrm{d}p_e)$.

The distensibility for the membranous labyrinth can be approximated on the basis of basic geometrical and physical properties of the membranous labyrinth. From the theory of thin-walled tubes we know that $\mathrm{D} = 2a/\bar{E}h$ where a is the radius of the SCC duct, h the wall thickness and $\bar{E}$ the average Young's modulus (Lighthill, 1975). If we assume Young's modulus to be on the order of its value for veins (10^5Pa; Pedley, 1980) we get a distensibility on the order of $10^{-4}\,\mathrm{Pa}^{-1}$. With the values estimated by Rabbitt *et al.* (1999), the distensibility is even as large as $10^{-2}\,\mathrm{Pa}^{-1}$. Further data on the mechanical properties of the membranous labyrinth can be found, for instance, in Wit *et al.* (2000).

From the distensibility, we can compute the local displacement of the walls as a function of the local fluid pressure. For typical acoustic pressures of less than 1 Pa this corresponds to wall displacements of less than 1% of the radius of the membraneous duct. For a linear inviscid pulse propagation, the wave speed is given as $c = \sqrt{1/\mathrm{D}\rho}$ where ρ is the density of the endolymph. We estimate it to be on the order of 1 m/s which corresponds to wave lengths of 1 mm for stimulation frequencies of 1 kHz.

4.2. One-dimensional model for the perilymph flow in the SCC. Instead of solving the full Navier–Stokes equations for the perilymph, we can reduce the physics for the perilymph to a one-dimensional inviscid model. This simplification is motivated by the transmission-line model for cochlear mechanics (Chapter 13) because the configuration of perilymph flow along the membranous duct in the SCC is similar to the configuration found in the cochlea. This popular model goes back to Peterson & Bogert (1950) and describes the perilymph flow in the cochlea and its interaction with the basilar membrane. The flow is modeled as inviscid because the high frequency of the pulsating flow leads to very thin Stokes boundary layers (cf. figure 21.1) whereas the bulk flow features nearly constant velocity profiles and behaves as if it was an inviscid flow.

Of course, one may ask if it is really appropriate to simplify the perilymph flow that much. Unfortunately, the answer to this question is not clear a priori. Nevertheless, there are some good reasons why it appears reasonable to proceed as described here: In contrast to the endolymph, the perilymph flow is just a means of transporting the acoustic stimulation from the stapes to the endolymph. Nonlinear phenomena which are probably also present in the perilymph flow (e.g. acoustic streaming) are likely to be much smaller in magnitude than the primary pulsating flow itself. In the endolymph, however, there is no principal pulsating bulk flow such that the weak nonlinear effects (if present) will dominate. For a more sophisticated model of the perilymph flow a two-dimensional model could be formulated following the two-dimensional cochlea model of Lesser & Berkley (1972) as it is described in Chapter 14.

Here, we outline the simplest possible model for the perilymph. Following the derivation of the transmission-line model for cochlear mechanics, we relate

the axial velocity of the perilymph u to the local perilymph pressure p_p by the momentum equation which reads

$$\rho \frac{\partial u}{\partial t} = -\frac{\partial p_p}{\partial s}$$

where ρ is the density of the perilymph and s is the arc length along the principal axis of the SCC. The continuity equation relates the velocity gradient to the change of the cross-section A_p of the perilymphatic space,

$$\frac{\partial u}{\partial s} = -\frac{1}{A_p} \frac{\partial A_p}{\partial t}.$$

The infinitesimal change $\mathrm{d}A_p$ of the perilymphatic lumen is of course equal to a negative change of the endolymphatic lumen $-\mathrm{d}A_e$. It is a function of the pressure difference $p_p - p_e$ across the wall of the membranous labyrinth.

The momentum and continuity equations define a system of partial differential equations in time t and space s for the velocity u and pressure p_p of the perilymph. These equations need to be solved along two pathways between the stapes and the third window (figure 21.2). The oscillating stapes imposes a velocity boundary condition at one end while the SCD acts as a pressure boundary condition at the other end.

It remains to be investigated whether the ampulla imposes another boundary condition to this system because the perilymphatic flow might be blocked by the membranous ampulla. In that case, we might have to impose homogeneous Dirichlet boundary conditions for the perilymph velocity at either end of the ampulla.

5. Numerical model for Tullio's phenomenon

The traveling wave model described in the previous section can be used in a numerical model for Tullio's phenomenon. To this end, the endolymphatic flow is simulated in the semicircular canals with a Navier–Stokes solver. The small wall displacements due to the traveling waves are introduced to the endolymph simulation via velocity boundary conditions at the walls.

The displacements at the walls will lead to a velocity and a pressure field in the endolymph. The pressure at the walls can be used as the endolymphatic pressure p_e in the traveling wave model. This allows us to compute the next time level in the traveling wave model by numerical integration which leads to new wall displacements for the endolymph simulation.

The fluid-structure coupling between the two fluids and the membranous wall results in a transient simulation of the endolymph flow in which the traveling wave model acts as a dynamic boundary condition.

The resulting endolymph flow is analyzed for its frequency content. Certainly, there will be a flow component at the acoustic stimulation frequency which is generated in the endolymph through a linear coupling with the pulsating perilymph. The physiologically relevant flow components, however, are those which generate a net flow (streaming) within the membranous labyrinth. These flow components do not necessarily have to be at zero frequency. It is sufficient that there exists a significant flow at a very low frequency such that the cupula can be deflected to one side for a few seconds.

Truly steady deflections of the cupula are not to be expected anyway, because the restoring force of the deflected cupula will eventually cancel or overcome the streaming of the endolymph.

In the case that we cannot find any significant streaming in the endolymph with the present model formulation, it is sensible to modify the model by adding new or different physical phenomena: for instance, a more complex perilymph model (e.g. Lesser & Berkley, 1972) and/or a more detailed representation of the mechanics of the membranous wall for modeling the endolymph/perilymph coupling. These modifications could address, for instance, the fact that the transmission-line model is based on a long-wave assumption which leads to a linear wave equation. As estimated earlier, we expect traveling waves of approximately 1 mm length which could violate the long-wave assumption and lead to nonlinear phenomena in the wave propagation (see e.g. Pedley, 1980 for a thorough discussion of such effects).

CHAPTER 22

Influence of angular motions on the otolith organs

Boselli *et al.* (2010*c*) presented new results on the endolymphatic flow fields in SCCs to a wider community at the 6th meeting of the Bárány society. The principal result of this numerical investigation was the existence of vortical flows in the utricle and ampulla during angular accelerations and decelerations of the vestibular system. The detailed nature of the endolymphatic flow field is discussed in Chapter 6. In the present chapter, we will study the influence of the utricular vortex on the otolith organs. This chapter is based on the results and discussion in Boselli *et al.* (2011).

Our typical understanding of the otolith organs does not include any active role for the endolymph. Typical models for the otolith organ (e.g. Jaeger *et al.*, 2002) implicitly assume the endolymph to be at rest (which is indeed the case for linear accelerations). Based on the smallest linear acceleration of approximately $2 \times 10^{-3} g$ (Peters, 1969) which can be sensed by the utricle, we can compute an equivalent shear stress acting on the macula of

$$\tau_{\min} \approx 2 \times 10^{-3} g \cdot (\rho_o - \rho_f) \cdot b \approx 2 \times 10^{-4}\,\mathrm{Pa} \tag{119}$$

where $b \approx 30\mu$m is the thickness of the layer of otoconia sitting on top of the hair cells, and $\rho_{o,f}$ are the densities of the otoconia and the endolymph, respectively.

Boselli *et al.* (2011) showed that the utricular vortex leads to shear stresses at the walls of the utricle which appear to be highest at the location of the utricular macula, i.e. the sensory epithelium of the utricle (figure 22.1). These wall-shear stresses reach values on the order of 10^{-3} Pa. Even though the above calculation of the sensitivity threshold of the utricle, Eq. (119), contains several rough assumptions, it appears fair to state that natural rotatory head maneuvers can lead to fluid flows which stimulate the utricular macula above its sensitivity threshold.

The coupling mechanism between angular motion and the otolith organs leads to a sensory crosstalk. Unfortunately, we were unable to find any experimental results which are able to confirm conclusively our theoretical and numerical results. Nevertheless, there exist phenomena which could be explained by the described

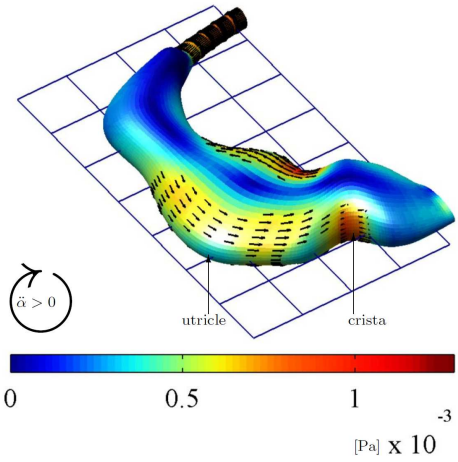

FIGURE 22.1. Shear stress at the walls of the utricle and the horizontal ampulla during angular acceleration ($120°/s^2$) in the plane of the horizontal canal (from Boselli *et al.*, 2011).

coupling mechanism. The utricular cavity of some vertebrates, for instance, contains a structure known as *papilla neglecta* which is known to respond to angular motion (Brichta & Goldberg, 1998). The papilla neglecta consists of a few hair cells embedded in a small cupula which is protruding from the utricular wall. It cannot be stimulated directly by inertial forces because there are no otoconia with higher density. Therefore, it appears likely that the utricular vortex is responsible for the response to rotation. Another possibly related phenomenon has been reported by Bockisch *et al.* (2005) who observed a lack of otolith contribution to yaw head rotations while there is such a contribution for rotations in other directions. This effect could be explained by the particular pattern of the wall-shear stress on the utricular macula. During a yaw head rotation the vortex rotates roughly in the plane of the utricular macula. This vortex does not deflect the hair cells on the macula unidirectionally but along the circular stream lines. We may conjecture that the opposing stimuli for the different hair cells cancel across the whole macula such that the otolithic contribution disappears for yaw rotations.

The previous reasoning points out the relevance of different wall-shear stress patterns for different planes of rotation. Obviously, the wall-shear stress pattern contains information about the angular velocity as well as about the plane of rotation. While a simple acceleration sensor with a mass and a spring would not be able to sense different patterns, the otolith organs may be able to do that because they contain a relatively large number of hair cells (even more than

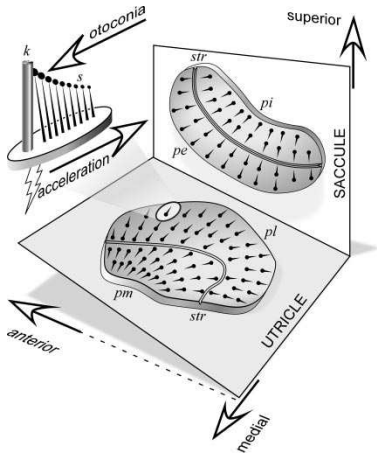

FIGURE 22.2. Schematic of the structure and orientation of the utricular and saccular maculae. The alignment of the hair cells is indicated by a dot for the kinocilia (k) and a thin line for the stereocilia (s). The firing rate of the hair cell increases when the stereocilia are deflected toward the kinocilium. The striola (str) separates each macula into two regions of opposing hair-cell alignment. Reprinted from Fitzpatrick & Day (2004).

the cochlea!) which are oriented in a structured but non-uniform manner across the cupula (figure 22.2). Therefore, we may speculate whether some anatomical features of the otoliths (e.g. the striola running through the center of the macula) are actually related to these wall-shear stress patterns.

Along the same line of thought, it is not unlikely that there exists a direct relation between the location of the maximum shear stress and the position of the macula within the utricular cavity. Boselli *et al.* (2011) have also shown that the elliptic cross-section of the utricular cavity increases the level of wall-shear stress at the macula. Therefore, it is not unlikely that this specific morphology is the result of an evolutionary optimization.

Finally, there is an interesting connection to a common disease of the inner ear known as Ménière's dis¡ease. In Ménière's disease, it is known that the pressure of the endolymph is increased (*endolymphatic hydrops*) which leads to a significantly enlarged utricle. Boselli *et al.* (2011) showed that size of the utricle increases strength of the vortex and thereby also the magnitude of the wall-shear stress on the macula. This suggests that vertigo (which can be a result of Ménière's disease) are related to an altered flow field in the utricle.

CHAPTER 23

Concluding remarks

In the various chapters of this book, we have laid out different aspects of the fluid mechanics of the inner ear. It should have become clear that this tiny organ hosts a remarkable variety of physical phenomena which are in a subtle balance. Only their tight interaction enables the three sensorial functions of the inner ear (hearing, linear and angular balance).

1. Biomedical applications

Next to satisfying our desire for a better understanding of human physiology, the presented models of the organs of the inner ear can serve quite practical purposes in the field of biomedical engineering.

Our models of BPPV (chapters 8 & 9) can support the medical practitioner in the diagnosis and therapy of this commonly occurring form of vertigo. Further refinements of these models (e.g. Boselli *et al.*, 2010*a*) in combination with patient-specific imaging of the SCC (e.g. Bradshaw *et al.*, 2010*b*,*a*) will eventually enable custom-tailored therapies for treating BPPV.

With the advent of new generations of micromechanical hearing aids, a detailed understanding of the hydrodynamics within the cochlea has regained the interest of scientists and manufacturers alike. Cochlear actuators which produce mechanical signals within the perilymphatic fluid space or artificial ciliary sensors to replace damaged hair cells interact directly with the fluids in the cochlea. Whereas the cochlear actuator stimulates traveling waves in a relatively large fluid space of about one millimeter diameter, the artificial hair cells are immersed in a fluid space of only a few micrometers height (tectorial gap). Nevertheless both flow systems are relevant for hearing and are in close interaction. Therefore, the design and optimization of this new generation of hearing aids requires a comprehensive model of the whole cochlea with a particular focus on the hydrodynamics in the various fluid spaces.

2. Toward a comprehensive mechanical model of the inner ear

In particular, in the last few chapters, we have tried to look at the inner ear as a complete system and not just as a sum of three different sensors. In

order to better understand complex pathologies which affect multiple organs (e.g. Ménière's disease) it is necessary to treat the inner ear as a single physiological system with a wide range of tightly coupled physical mechanisms and phenomena. The modeling concept proposed in the following is a step toward such a systemic understanding of the inner ear.

We showed in Chapter 20 that the SCCs and the cochlea are separated in terms of their relevant time scales. A comprehensive mechanical model of the whole inner ear must therefore be able to cover a very wide range of time scales. Moreover, there is obviously also a wide range of spatial scales which includes tiny displacements of the cupula and/or the basilar membrane as well as the full length of the uncoiled cochlea. Next to the spatial and temporal scales to be covered, a comprehensive model must describe the physics of the fluids (endolymph, perilymph), of the structural components which can be soft (cupula, basilar membrane, Corti organ, membranous labyrinth, etc.) or relatively stiff (stapes footplate, bony walls), and of the electrochemical and micromechanical processes in the OHC. We are therefore facing a multi-scale and multi-physics problem.

A multi-scale numerical model of the inner ear is a formidable challenge for computational science and, in particular, for high-performance computing. Only a careful selection of numerical methods and algorithms which are tuned for specific computer architectures will allow a simulation of the complete inner ear. Furthermore, the multi-physics aspect suggests that we should use different custom-tailored numerical approaches, e.g. discretization schemes, for the different physical system. It is not sensible to model the fluid dynamics, the solid mechanics and the active OHCs with one and the same numerical approach. This leads to separate simulation modules for different physical processes which requires an explicit coupling of the modules.

At the same time, it should be clear that a comprehensive model of the inner ear cannot consist of a large monolithic numerical simulation. We have shown in Chapter 19 that a monolithic computational model for the cochlea alone is within reach. But it is certainly out of reach, if this model should cover the whole inner ear. Moreover, we must not forget that there exist several phenomena and processes in the inner ear which we have not touched in this monograph. Most prominently, this is the bone conduction of acoustic signals which adds yet another wave guide to the inner ear. Of equal importance are the details of the electrochemical and micromechanical processes in the outer hair cells which we have described here only by heuristic lumped-parameters models. Furthermore, these are anatomical details of the Corti Organ, the micromechanics of the cupula, the flow in the endolymphatic duct and sac (two additional anatomical features of the membranous labyrinth), the electrophysiology within the cochlea (relevant for cochlear implants), the dynamics of the middle-ear ossicles and, last but not

least, the mechanical properties of the soft tissues in the inner ear. This list is certainly not exhaustive. Nevertheless, it already shows that the level of detail at which certain processes are to be modeled has to be chosen with great caution. In this context, the model of Tullio's phenomenon (Chapter 21) with its different modeling approaches for the various involved processes should serve as a guideline for the sensible design of a comprehensive mechanical model of the inner ear.

Bibliography

Abramowitz, M. & Stegun, I. A. 1965 *Handbook of Mathematical Functions*. Dover.

Allen, J. 1978 Two-dimensional cochlear fluid model: New results. *J. Acoust. Soc. Am.* **61**, 110–119.

Avrahami, I. & Gharib, M. 2008 Computational studies of resonance wave pumping in compliant tubes. *J. Fluid Mech.* **608**, 139–160.

Aw, S., Todd, M., Aw, G., McGarvie, L. & Halmagyi, G. 2005 Benign positional nystagmus – A study of its three-dimensional spatio-temporal characteristics. *Neurology* **64** (11), 1897–1905.

Baloh, R. W., Sloane, P. D. & Honrubia, V. 1989 Quantitative vestibular function testing in elderly patients with dizziness. *Ear Nose Throat J.* **68**, 935–939.

Baumgart, J., Chiaradia, C., Fleischer, M., Yarin, Y., Grundmann, R. & Gummer, A. W. 2009 Fluid mechanics in the subtectorial space. In *Concepts and challenges in the biophyics of hearing*, pp. 288–296. World Scientific Publishing.

Bender, C. M. & Orszag, S. A. 1978 *Advanced Mathematical Methods for Scientists and Engineers*. McGraw–Hill.

Beyer, R. P. 1992 A computational model of the cochlea using the immersed boundary method. *J. Comp. Phys.* **98**, 145–162.

Bockisch, C., Straumann, D. & Haslwanter, T. 2005 Human 3-D aVOR with and without otolith stimulation. *Exp. Brain Res.* **161**, 358–367.

Böhnke, F. & Arnold, W. 1999 3D-finite element model of the human cochlea including fluid-structure couplings. *ORL* **61**, 305–310.

Böhnke, F. & Arnold, W. 2006 Bone conduction in a three-dimensional model of the cochlea. *ORL* **68**, 393–396.

Böhnke, F. & Scharff, M. 2009 Acoustic streaming the cochlea. In *Concepts and challenges in the biophyics of hearing*, pp. 319–322. World Scientific Publishing.

Boselli, F., Kleiser, L. & Obrist, D. 2011 Vortical flow in the utricle and the ampulla — A computational study on the fluid dynamics of the vestibular system. *Biomech. Model. Mechanobiol.* Submitted.

Boselli, F., Obrist, D. & Kleiser, L. 2009 Numerical simulation of the flow in semicircular canals with the method of fundamental solutions. *Proc. Appl. Math. Mech.* **9**.

Boselli, F., Obrist, D. & Kleiser, L. 2010*a* A meshless boundary method for computation of Stokes flow with particles in the semicircular canals of the inner ear. *Proc. Appl. Math. Mech.* **10**, 459–460.

Boselli, F., Obrist, D. & Kleiser, L. 2010*b* Multilayer MFS for Stokes problems. In *Recent Studies in Meshless & Other Novel Computational Methods* (ed. Bozidar Sarler & Satya. N. Atluri), pp. 71–86. Tech Science Press.

Boselli, F., Obrist, D. & Kleiser, L. 2010*c* A new study on the fluid dynamics in the SCC and the utricle. *Journal of Vestibular Research* **20** (3), 168–169.

Boselli, F., Sim, J. H., Kleiser, L. & Obrist, D. 2010*d* New insights into the biofluid dynamics in the utricle of the vestibular system. In *17th Congress of the European Society of Biomechanics ESB 2010, July 5-8 2010, Edinburgh*.

Bradshaw, A., Curthoys, I., Todd, M., Magnussen, J., Taubman, D., Aw, S. & Halmagyi, M. 2010*a* Precise measurement of the human semicircular canals in CT and micro-CT. *Journal of Vestibular Research* **20** (3), 169–170.

Bradshaw, A. P., Curthoys, I. S., Todd, M. J., Magnussen, J. S., Taubman, D. S., Aw, S. T. & Halmagyi, G. M. 2010*b* A mathematical model of human semicircular canal geometry: a new basis for interpreting vestibular physiology. *JARO* **11**, 145–159.

Breuer, J. 1874 Über die Funktion der Bogengänge des Ohrlabyrinths. *Wien. Med. Jahrb.* **4**, 72.

Brichta, A. M. & Goldberg, J. M. 1998 The papilla neglecta of turtles: A detector of head rotations with unique sensory coding properties. *J. Neurosci.* **18** (11), 4314–4324.

Bronzino, J. 1995 *The Biomedical Engineering Handbook*. CRC Press.

Bungay, P. M. & Brenner, H. 1973 Pressure drop due to the motion of a sphere near the wall bounding a Poiseuille flow. *J. Fluid Mech.* **60** (1), 81–96.

Cai, H., Manoussaki, D. & Chadwick, R. 2005 Effects of coiling on the micromechanics of the mammalian cochlea. *J. R. Soc. Interface* **2**, 341–348.

Campos, A. 1990 Otoconial degeneration in the aged utricle and saccule. *Advances in Otorhinolaryngology* **45**, 143–153.

Carey, J. P., Hirvonen, T. P., Hullar, T. E. & Minor, L. B. 2004 Acoustic responses of vestibular afferents in a model of superior canal dehiscence. *Otology & Neurotology* **25**, 345–352.

Carey, J. P., Minor, L. B. & Nager, G. T. 2000 Dehiscence or thinning of bone overlying the superior semicircular canal in a temporal bone survey. *Arch Otolaryngol Head Neck Surg* **126** (2), 137–147.

Causin, P., Gerbeau, J. & Nobile, F. 2005 Added-mass effect in the design of partitioned algorithms for fluid–structure problems. *Comput. Meth. in Appl. Mech. Engrg.* **194** (42-44), 4506 – 4527.

Chadwick, R. S., Dimitriades, E. K. & Iwasa, K. H. 1996 Active control of waves in a cochlear model with subpartitions. *PNAS* **93**, 2564–2569.

Cheng, L., White, R. & Grosh, K. 2008 Three-dimensional viscous finite element formulation for acoustic fluid-structure interaction. *Comput. Methods Appl. Mech. Engrg.* **197**, 4160–4172.

Clift, R., Grace, J. & Weber, M. 1978 *Bubbles, Drops and Particles*. Academic Press.

Cohen, B., Matsuo, V. & Raphan, T. 1977 Quantitative analysis of the velocity characteristics of optokinetic nystagmus and optokinetic after-nystagmus. *J. Physiol.* **270**, 321–344.

Crum Brown, A. 1874 On the sense of rotation and the anatomy and physiology of the semicircular canals of the inner ear. *J. Anat. Physiol.* **8**, 327.

Curthoys, I. & Oman, C. 1987 Dimensions of the horizontal semicircular duct, ampulla and utricle in the human. *Acta Otolaryngol.* **103**, 254–261.

Curthoys, I. S., Markham, C. H. & Curthoys, E. J. 1977*a* Semicircular canal radii of curvature (r) in cat, guinea pig and man. *J. Morph.* **151**, 1–16.

Curthoys, I. S., Markham, C. H. & Curthoys, E. J. 1977*b* Semicircular duct and ampulla dimensions in cat, guinea pig and man. *J. Morph.* **151**, 17–34.

Dai, M., Klein, A., Cohen, B. & Raphan, T. 1999 Model-based study of the human cupular time constant. *J. Vest. Res.* **9** (4), 293–301.

Dallos, P., Popper, A. & Fay, R., ed. 1996 *The cochlea*. Springer.

Damiano, E. & Rabbitt, R. 1996 A singular perturbation model of fluid dynamics in the vestibular semicircular canal and ampulla. *J. Fluid Mech.* **307**, 333–372.

De Boer, E. 1996 Mechanics of the cochlea. Modeling efforts. In *The cochlea* (ed. P. Dallos, A.N. Popper & R.R. Fay), pp. 258–317. Springer.

De Boer, E. & Nuttall, A. L. 2009 Obvious and 'hidden' waves in the cochlea. In *Concepts and challenges in the biophyics of hearing*, pp. 34–40. World Scientific Publishing.

De Tullio, M. D., Cristallo, A., Balaras, E. & Verzicco, R. 2009 Direct numerical simulation of the pulsatile flow through an aortic bileaflet mechanical heart valve. *J. Fluid Mech.* **622**, 259–290.

Decraemer, W. F., de La Rochefoucauld, O., Dong, W., Khanna, S. M., Dirckx, J. J. J. & Olson, E. S. 2007 Scala vestibuli pressure and three-dimensional stapes velocity measured in direct succession in gerbil. *J. Acoust. Soc. Am.* **121** (5), 2774–2791.

Dix, M. & Hallpike, C. 1952 The pathology, symptomatology, and diagnosis

of certain common disorders of the vestibular system. *Proc. Roy. Soc. Lond.* **45**, 341–354.

Duke, T. A. & Jülicher, F. 2007 Critical oscillators as active elements in hearing. In *Active Processes and Otoacoustic Emissions in Hearing* (ed. Geoffrey A. Manley, Richard R. Fay & Arthur N. Popper), *Springer Handbook of Auditory Research*, vol. 30, pp. 63–92. Springer New York.

Eaton-Peabody Laboratory of Auditory Physiology. 2008 3-D virtual models of the human temporal bone and related structures. `http://research.meei.harvard.edu/otopathology/3dmodels/temporal_bone.html`, accessed 10.10.2011.

Edom, E., Sim, J., Huber, A. M., Kleiser, L. & Obrist, D. 2010*a* Numerical simulation of the fluid flow due to rocking stapes motion. *Biomedizinische Technik* **55 (suppl. 1)**, 209–211.

Edom, E., Sim, J., Huber, A. M., Kleiser, L. & Obrist, D. 2010*b* Numerical simulation of the fluid flow due to rocking stapes motion. In *44. DGBMT Jahrestagung, 5-8 October 2010, Rostock-Warnemünde, Germany*. Poster presentation.

Epley, J. 1992 The canalith repositioning procedure for treatment of benign paroxysmal positional vertigo. *Otolaryngol. Head Neck Surg.* **107**, 399–404.

Ewald, J. 1892 *Physiologische Untersuchungen über das Endorgan des Nervus Octavus*. J.F. Bergmann.

Fadlun, E. A., Verzicco, R., Orlandi, P. & Mohd-Yusof, J. 2000 Combined immersed-boundary finite-difference methods for three-dimensional complex flow simulations. *Journal of Computational Physics* **161** (1), 35 – 60.

Ferziger, J. H. & Perić, M. 2002 *Computational Methods for Fluid Dynamics*, 3rd edn. Springer.

Fettiplace, R. & Hackney, C. M. 2006 The sensory and motor roles of auditory hair cells. *Nature Reviews Neuroscience* **7**, 19–29.

Fitzpatrick, R. C. & Day, B. L. 2004 Probing the human vestibular system with galvanic stimulation. *Journal of Applied Physiology* **96** (6), 2301–2316.

Furman, J. M. & Cass, S. P. 1999 Benign paroxysmal positional vertigo. *N. Engl. J. Med.* **341** (21), 1590–1596.

Givelberg, E. & Bunn, J. 2003 A comprehensive three-dimensional model of the cochlea. *J. Comp. Phys.* **191**, 377–391.

Grant, J. W. & Van Buskirk, W. C. 1976 Experimental measurement of the stiffness of the cupula. *Biophys J.* **16** (6), 669–678.

Groen, J. & Jongkees, L. 1948 The threshold of angular acceleration perception. *J. Physiol.* **107** (1), 1–7.

Grossman, G. E., Leigh, R. J., Abel, L. A., Lanska, D. J. & Thurston, S. E. 1988 Frequency and velocity of rotational head perturbations during locomotion. *Exp. Brain Res.* **70** (3), 470–476.

Halmagyi, G. M., Curthoys, I. S., Colebatch, J. G. & Aw, S. T. 2005 Vestibular responses to sound. *Ann. N.Y. Acad. Sci.* **1039**, 54–67.

Happel, J. & Brenner, H. 1973 *Low Reynolds Number Hydrodynamics: with special applications to particulate media*, 2nd edn. Leyden: Noordhoff.

Hato, N., Stenfelt, S. & L., G. R. 2003 Three-dimensional stapes footplate motion in human temporal bones. *Audiol. Neurootol.* **8**, 140–152.

He, W., Fridberger, A., Porsov, E., Grosh, K. & Ren, T. 2008 Reverse wave propagation in the cochlea. *PNAS* **105** (7), 2729–2733.

van Hengel, P. 1996 Emissions from cochlear modelling. PhD thesis, University of Groningen.

Henniger, R., Obrist, D. & Kleiser, L. 2010 High-order accurate solution of the Navier–Stokes equations on massively parallel computers. *J. Comp. Phys.* **299** (10), 3543–3572.

Hepp, K. 1990 On Listing's law. *Commun. Math. Phys.* **132**, 285–292.

Highstein, S., Rabbitt, R., Holstein, G. & Boyle, R. 2005 Determinants of spatial and temporal coding by semicircular canal afferents. *J. Neurophysiol* **93**, 2359–2370.

House, M. G. & Honrubia, V. 2003 Theoretical models for the mechanisms of benign paroxysmal positional vertigo. *Audiol. Neurootol.* **8**, 91–99.

Huber, A., Linder, T., Ferrazini, M., Schmid, S., Dillier, N., Stoeckli, S. & Fisch, U. 2001 Intraoperative assessment of stapes movement. *Ann. Otol. Rhinol. Laryngol.* **110**, 31–35.

Huber, A. M., Sequeira, D., Breuninger, C. & Eiber, A. 2008 The effects of complex stapes motion on the response of the cochlea. *Otol. Neurotol.* **29** (8), 1187–1192.

Ifediba, M. A., Rajguru, S. M., Hullar, T. E. & Rabbitt, R. D. 2007 The role of 3-canal biomechanics in angular motion transduction by the human vestibular labyrinth. *Ann. biomed. Eng.* **35** (7), 1247–1263.

Inselberg, A. 1978 Cochlear dynamics: the evolution of a mathematical model. *SIAM Review* **20** (2), 301–351.

Jaeger, R., Takagi, A. & Haslwanter, T. 2002 Modeling the relation between head orientations and otolith responses in humans. *Hear. Res.* **173** (1-2), 29 – 42.

Karavitaki, K. D. & Mountain, D. V. 2007 Evidence for outer hair cell driven oscillatory fluid flow in the tunnel of Corti. *Biophys. J.* **92**, 3284–3293.

Kern, A. 2003 A nonlinear biomorphic Hopf-amplifier model of the cochlea. PhD thesis, ETH Zurich.

Kern, A., Heid, C., Steeb, W.-H., Stoop, N. & Stoop, R. 2008 Biophysical parameters modification could overcome essential hearing gaps. *PLoS Comput Biol* **4** (8).

Kern, A. & Stoop, R. 2003 Essential role of couplings between hearing nonlinearities. *Phys. Rev. Lett.* **91**, 128101–1–128101–4.

Kevorkian, J. 1990 *Partial Differential Equations - Analytical Solution Techniques*. Chapman & Hall.

Kiefer, J., Böhnke, F., Adunka, O. & Arnold, W. 2006 Representation of acoustic signals in the human cochlea in presence of a cochlear implant electrode. *Hearing Research* **221** (1-2), 36–43.

Kozlov, A. S., Baumgart, J., Risler, T., Versteegh, C. P. C. & Hudspeth, A. J. 2011 Forces between clustered stereocilia minimize friction in the ear on a subnanometre scale. *Nature* **474**, 376–379.

Kringlebotn, M. 1988 Network model for the human middle ear. *Scand. Audiol.* **17** (2), 75–85.

Lesser, M. B. & Berkley, D. A. 1972 Fluid mechanics of the cochlea. Part 1. *J. Fluid Mech.* **51**, 497–512.

Leveque, R. J. & Li, Z. 1994 The immersed interface method for elliptic equations with discontinuous coefficients and singular sources. *SIAM Journal on Numerical Analysis* **31** (4), 1019–1044.

Leveque, R. J., Peskin, C. S. & Lax, P. D. 1988 Solution of a two-dimensional cochlea model with fluid viscosity. *SIAM J. Appl. Math.* **48** (1), 191–213.

Lighthill, J. 1975 *Mathematical Biofluiddynamics*. SIAM.

Lighthill, J. 1978 Acoustic streaming. *J. Sound Vib.* **61**, 391–418.

Lighthill, J. 1981*a* Biomechanics of hearing sensitivity. *Trans. ASME: J. Vib. Acoust.* **113**, 1–13.

Lighthill, J. 1981*b* Energy flow in the cochlea. *J. Fluid Mech.* **106**, 149–213.

Lighthill, J. 1992 Acoustic streaming in the ear itself. *J. Fluid Mech.* **235**, 551–606.

Lim, D. 1984 Otoconia in health and disease. A review. *Ann. Otol. Rhinol. Laryngol. Suppl.* **112**, 17–24.

Lim, D. J. 1980 Cochlear anatomy related to cochlear micromechanics. A review. *J. Acoust. Soc. Am.* **67** (5), 1686–1695.

Lim, K.-M. & Li, H. 2007 A coupled boundary element/finite difference method for fluid-structure interaction with application to dynamic analysis of outer hair cells. *Computers & Structures* **85** (11-14), 911 – 922, fourth MIT Conference on Computational Fluid and Solid Mechanics.

Lim, K.-M. & Steele, C. R. 2002 A three-dimensional nonlinear active cochlear model analyzed by the WKB-numeric method. *Hearing Research* **170** (1-2), 190–205.

Lim, K.-M. & Steele, C. R. 2003 Response suppression and transient behavior in a nonlinear active cochlear model with feed-forward. *Int. Journal of Solids and Structures* **40**, 5097–5107.

Linder, T. E., Ma, F. & Huber, A. M. 2003 Round window atresia and its effect on sound transmission. *Otol. Neurotol.* **24** (2), 259–263.

Mach, E. 1875 *Grundlinien der Lehre von den Bewegungsempfindungen*. Leipzig: Wilhelm Engelmann.

Malcom, R. 1968 A quantitative study of vestibular adaptation in humans. In *Fourth Symposium on Role of Vestibular Organs in Space Exploration*, pp. NASA SP–187.

Manley, G., Fay, R. & Popper, A., ed. 2008 *Active Processes and Otoacoustic Emissions in Hearing*. Springer.

Manoussaki, D. & Chadwick, R. 2000 Effects of geometry on fluid loading in a coiled cochlea. *SIAM J. Appl. Math.* **61** (2), 369–386.

Manoussaki, D., Chadwick, R., Ketten, D., Arruda, J., Dimitriadis, E. & O'Malley, J. 2008 The influence of cochlear shape on low-frequency hearing. *PNAS* **105** (16), 6162–6166.

Manoussaki, D., Dimitriadis, E. & Chadwick, R. 2006 Cochlea's graded curvature effect on low frequency waves. *Phys. Rev. Lett.* **96**.

Manzari, L., Burgess, A. M., Macdougall, H. G. & Curthoys, I. S. 2011 Enhanced otolithic function in semicircular canal dehiscence. *Acta Oto-Laryngologica* **131**, 107–112.

Mao, X. & Sherwin, S. 2011 Continuous spectra of the Batchelor vortex. *J. Fluid Mech.* **681**, 1–23.

Martignoli, S., van der Vyver, J.-J., Kern, A., Uwate, Y. & Stoop, R. 2007 Analog electronic cochlea with mammalian hearing characteristics. *Applied Physics Letters* **91** (064108).

Marxen, M., Sullivan, P. E., Loewen, M. R. & Jahne, B. 2000 Comparison of Gaussian particle center estimators and the achievable measurement density for particle tracking velocimetry. *Exp. Fluids* **29** (2), 145–153.

McLaren, J. & Hillman, D. 1976 Configuration of the cupula during endolymph pressure changes. *Neurosci. Abstr.* **3**, 544.

Minor, L. B., Solomon, D., Zinreich, J. S. & Zee, D. S. 1998 Sound- and/or pressure-induced vertigo due to bone dehiscence of the superior semicircular canal. *Arch Otolaryngol Head Neck Surg* **124** (3), 249–258.

Mojallal, H., Stieger, C., Grasshof, E., Kompis, M., Bernhard, H., Haller, M., Haeusler, R. & Lenarz, T. 2007 DACS A new implantable hearing system for moderate to severe mixed hearing loss. In *World Congress on Medical Physics and Biomedical Engineering 2006* (ed. R. Magjarevic, J. H. Nagel, R. Magjarevic & J. H. Nagel), *IFMBE Proceedings*, vol. 14, pp. 3015–3017. Springer Berlin Heidelberg.

Nakajima, H., Dong, W., Olson, E., Merchant, S., Ravicz, M. & Rosowski, J. 2009 Differential intracochlear sound pressure measurements in normal human temporal bones. *JARO* **10**, 23–36, 10.1007/s10162-008-0150-y.

Nobili, R., Mammano, F. & Ashmore, J. 1998 How well do we understand the cochlea? *Trends Neurosci.* **21** (4), 159–167.

Obrist, D. 2007 Numerical simulation of the endolymph flow in a semicircular canal. *Proc. Appl. Math. Mech.* **7** (1), 4100029–4100030.

Obrist, D. 2008 Fluidmechanics of semicircular canals – revisited. *Z. angew. Math. Phys.* **59**, 475–497.

Obrist, D. 2009 Transient inviscid flow in a passive linear model of the cochlea. *Proc. Appl. Math. Mech.* **9**.

Obrist, D. & Hegemann, S. 2008 Fluid-particle dynamics in canalithiasis. *Roy. Soc. Interface* **5** (27), 1215–1229.

Obrist, D., Hegemann, S., Kronenberg, D., Häuselmann, O. & Rösgen, T. 2010 In-vitro model of a semicircular canal: Design and validation of the model and its use for the study of canalithiasis. *J. Biomech.* **43**, 1208–1214.

Obrist, D., Kleiser, L. & Rösgen, T. 2008 Particle trajectories in semicircular canals with canalithiasis. *J. Biomech.* **S308**.

Obrist, D. & Schmid, P. 2008 Resonance in the cochlea with wave packet pseudomodes. In *22nd Int. Congress of Theoretical and Applied Mechanics (ICTAM2008)*. Adelaide.

Obrist, D. & Schmid, P. J. 2010 Algebraically decaying modes and wave packet pseudomodes in swept Hiemenz flow. *J. Fluid Mech.* **643**, 309–331.

Obrist, D. & Schmid, P. J. 2011 Algebraically diverging modes upstream of a swept bluff body. *J. Fluid Mech.* **683**, 346–356.

Ohmi, K. & Li, H. Y. 2000 Particle-tracking velocimetry with new algorithms. *Meas. Sci. Technol.* **11** (6), 603–616.

Olson, E. S. 1998 Observing middle and inner ear mechanics with novel intracochlear pressure sensors. *J. Acoust. Soc. Am.* **103** (6), 3445–3463.

Oman, C., Marcus, E. & Curthoys, I. 1987 The influence of semicircular canal morphology on endolymph flow dynamics. *Acta Otolaryngol.* **103**, 1–13.

Otsuka, K., Suzuki, M. & Furuya, M. 2003 Model experiment of benign paroxysmal positional vertigo mechanism using the whole membranous labyrinth. *Acta Otolaryngol.* **123** (4), 515–118.

Parnes, L. S. & Mcclure, J. A. 1992 Free-floating endolymph particles: A new operative finding during posterior semicircular canal occlusion. *The Laryngoscope* **102** (9), 988–992.

Parthasarathi, A., Grosh, K. & Nuttall, A. 2000 Three-dimensional numerical modeling for global cochlear dynamics. *J. Acoust. Soc. Am.* **107** (1), 474–485.

Pau, H. & Limberg, W. 1988 Die Bedeutung von schleichenden Strömungen für die kalorische Erregbarkeit der Gleichgewichtsorgane in Schwerelosigkeit. *Laryng. Rhinol. Otol.* **67**, 616–620.

Pau, H. W. & Limberg, W. 1990*a* Fluid kinetics of endolymph during calorization. *Acta Otolaryngol (Stockh)* **109**, 331–336.

Pau, H. W. & Limberg, W. 1990*b* Fluid kinetics of endolymph during rotation. *Acta Otolaryngol (Stockh)* **110**, 7–10.

Pedley, T. J. 1980 *The fluid mechanics of large blood vessels*. Cambridge University Press.

Peskin, C. S. 2002 The immersed boundary method. *Acta Numerica* pp. 479–517.

Peters, R. 1969 Dynamics of the vestibular system and their relation to motion perception, spatial disorientation, and illusions. *Tech. Rep.* CR–1309. NASA.

Peterson, L. C. & Bogert, B. P. 1950 A dynamical theory of the cochlea. *J. Acoust. Soc. Am.* **22**, 369–381.

Pozrikidis, C. 2007 Hydrodynamics of a vibrating stapes prosthesis in stapedotomy. *Engineering Analysis with Boundary Elements* **31** (1), 1 – 9.

Pozrikidis, C. 2008 Boundary-integral modeling of cochlear hydrodynamics. *Journal of Fluids and Structures* **24** (3), 336 – 365.

Rabbitt, R. & Damiano, E. 1992 A hydroelastic model of macromechanics in the endolymphatic vestibular canal. *J. Fluid Mech.* **238**, 337–369.

Rabbitt, R., Damiano, E. & Grant, J. 2004 Biomechanics of the semicircular canals and otolith organs. In *The Vestibular System* (ed. Stephen Highstein, Richard Fay & Arthur Popper), *Springer Handbook of Auditory Research*, vol. 19, pp. 153–201. Springer New York.

Rabbitt, R. D., Boyle, R. & Highstein, S. M. 1999 Influence of surgical plugging on horizontal semicircular canal mechanics and afferent response dynamics. *Journal of Neurophysiology* **82** (2), 1033–1053.

Rabbitt, R. D., Breneman, K. D., King, C., Yamauchi, A. M., Boyle, R. & Highstein, S. M. 2009 Dynamic displacement of normal and detached semicircular canal cupula. *JARO* .

Rajguru, S. M., Ifediba, M. A. & Rabbitt, R. D. 2004 Three-dimensional biomechanical model of benign paroxysmal positional vertigo. *Ann. Biomed. Eng.* **32** (6), 831–846.

Rajguru, S. M., Ifediba, M. A. & Rabbitt, R. D. 2005 Biomechanics of horizontal canal benign paroxysmal positional vertigo. *J. Vest. Res.* **15**, 203–214.

Rajguru, S. M. & Rabbitt, R. D. 2007 Afferent responses during experimentally induced semicircular canalithiasis. *J. Neurophysiol.* **97**, 2355–2363.

Raphan, T., Matsuo, V. & Cohen, B. 1979 Velocity storage in the vestibulo-ocular reflex arc (VOR). *Exp. Brain Res.* **35**, 229–248.

Rayleigh, L. 1884 On the circulation of air observed in kundt's tubes, and on some allied acoustical problems. *Phil. Trans. R. Soc. Lond.* **175**, 1–21.

Repetto, R., Siggers, J. & Stocchino, A. 2008 Steady streaming within a

periodically rotating sphere. *J. Fluid Mech.* **608**, 71–80.

Riley, N. 2001 Steady streaming. *Annu. Rev. Fluid. Mech.* **33** (1), 43–65.

Robinson, D. 1977 Linear addition of optokinetic and vestibular signals in the vestibular nucleus. *Exp. Brain Res.* **30**, 447–450.

Robles, L. & Ruggero, M. A. 2001 Mechanics of the mammalian cochlea. *Physiological Review* **81**, 1305–1352.

Schmaltz, G. 1931 The physical phenomena occurring in the semicircular canals during rotary and thermic stimulation. *Proc. Roy. Soc. Med.* **25**, 359.

Schmid, P. & Henningson, D. S. 2000 *Stability and Transition in Shear Flows*. Springer.

Sim, J. H., Chatzimichalis, M., Lauxmann, M., Röösli, C., Eiber, A. & Huber, A. 2010 Complex stapes motions in human ears. *JARO* **11**, 329–341.

Songer, J. E. & Rosowski, J. J. 2007 A mechano-acoustic model of the effect of superior canal dehiscence on hearing in chinchilla. *J. Acoust. Soc. Am.* **122** (2), 943–951.

Songer, J. E. & Rosowski, J. J. 2010 A superior semicircular canal deshiscence-induced air-bone gap in chinchilla. *Hearing Research* **269**, 70–80.

Squires, T. M., Weidmann, M. S., Hain, T. C. & Stone, H. A. 2004 A mathematical model for top-shelf vertigo: the role of sedimenting otoconia in BPPV. *J. Biomech.* **37**, 1137–1146.

Steele, C. R. 1992 Electroelastic behavior of auditory receptor cells. *Biomimetics* **1** (1), 3–22.

Steele, C. R., Boutet de Monvel, J. & Puria, S. 2009 A multiscale model of the organ of Corti. *J. Mech. Mater. Struct.* **4** (4), 755–778.

Steinhausen, W. 1933 Über die Beobachtung der Cupula in den Bogengangsampullen des Labyrinths des lebenden Hechts. *Pflügers Archiv für die gesamte Physiologie des Menschen und der Tiere* **232**, 500–512.

Stoop, R., Jasa, T., Uwate, Y. & Martignoli, S. 2007 From hearing to listening: Design and properties of an actively tunable electronic hearing sensor. *Sensors* **7**, 3287–3298.

Stoop, R. & Kern, A. 2004 Two-tone suppression and combination tone generation as computations performed by the Hopf cochlea. *Phys. Rev. Lett.* **93** (26), 268103.

Stoop, R., Steeb, W.-H., Gallas, J. & Kern, A. 2005 Auditory two-tone suppression from a subcritical Hopf cochlea. *Physica A* **351**, 175–183.

Suzuki, M., Kadir, A., Hayashi, N. & Takamoto, M. 1996*a* Functional model of benign paroxysmal positional vertigo using an isolated frog semicircular canal. *J. Vestib. Res.* **6** (2), 121–125.

Suzuki, M., Kadir, A., Takamoto, M. & Hayashi, N. 1996*b* Experimental model of vertigo induced by detached otoconia. *Acta Otolaryngol.* **116** (2), 269–272.

Taber, L. A. & Steele, C. R. 1979 Comparison of "WKB" and experimental results for three-dimensional cochlear models. *J. Acoust. Soc. Am.* **65**, 1007–1018.

Thomann, H. 1978 Simple pumping mechanism in a valveless tube. *Z. angew. Math. Phys.* **29**, 169–177.

Trefethen, L. N. & Embree, M. 2005 *Spectra and pseudospectra: The behavior of nonnormal matrices and operators*. Princeton Univ. Press.

Trefethen, L. N., Trefethen, A. E., Reddy, S. C. & Driscoll, T. A. 1993 Hydrodynamic stability without eigenvalues. *Science* **261** (5121), 578–584.

Tullio, P. 1929 *Das Ohr und die Entstehung der Sprache und Schrift*, translated by a. jellinek edn. Berlin: Urban & Schwarzberg.

Tweed, D., Cadera, W. & Vilis, T. 1990 Computing three-dimensional eye position quaternions and eye velocity from search coil signals. *Vision Research* **30**, 97–110.

Valli, P., Botta, L., Zucca, G., Valli, S. & Buizza, A. 2008 Simulation of cupulolithiasis and canalolithiasis by an animal model. *J. Vestib. Res.* **18** (2-3), 89–96.

Valli, P., Buizza, A., Ghilardi, P., Pagliardi, M., Greco, G. & Favalli, V. 2006 Experimental approach to canalolithiasis by means of animal and physical models. In *24th Barany Society meeting, June 11-14 2006*. Uppsala, poster presentation.

Van Buskirk, W. & Grant, J. 1973 Biomechanics of the semicircular canals. In *Biomechanics Symposium*, pp. 53–54. ASME.

Van Buskirk, W., Watts, R. & Liu, Y. 1976 The fluid mechanics of the semicircular canals. *J. Fluid Mech.* **78** (1), 87–98.

Van Buskirk, W. C. 1977 The effects of the utricle on fluid-flow in semicircular canals. *Ann. Biomed. Eng.* **5** (1), 1–11.

Van Egmond, A., Groen, J. & Jongkees, L. 1949 The mechanics of the semicircular canal. *J. Physiol.* **110** (1), 1–11.

van Hengel, P., Duifhuis, H. & van den Raadt, M. 1996 Spatial periodicity in the cochlea: The result of interaction of spontaneous emissions? *J. Acoust. Soc. Am.* **99**, 3566–3571.

von Békésy, G. 1960 *Experiments in hearing*. McGraw–Hill, ed.: E. G. Wever.

Voss, S. E., Rosowski, J. J., Merchant, S. N. & Peake, W. T. 2000 Acoustic responses of the human middle ear. *Hear. Res.* **150** (1-2), 43 – 69.

Voss, S. E., Rosowski, J. J. & Peake, W. T. 1996 Is the pressure difference between the oval and round windows the effective acoustic stimulus for the cochlea? *J. Acoust. Soc. Am.* **100** (3), 1602–1616.

Welling, D. B., Parnes, L. S., O'Brien, B., Bakaletz, L. O., Brackmann, D. E. & Hinojosa, R. 1997 Particulate matter in the posterior semicircular canal. *The Laryngoscope* **107** (1), 90–94.

White, R. & Grosh, K. 2005 Microengineered hydromechanical cochlear model. *PNAS* **102** (5), 1296–1301.

Wit, H. P., Warmerdam, T. J. & Albers, F. W. J. 2000 Measurement of the mechanical compliance of the endolymphatic compartments in the guinea pig. *Hearing Research* **145** (1-2), 82 – 90.

Wittbrodt, M., CR, C. S. & Puria, S. 2006 Developing a physical model of the human cochlea using microfabrication methods. *Audiol Neurotol* **11**, 104–112.

Womersley, J. R. 1955 Method for the calculation of velocity, rate of flow and viscous drag in arteries when the pressure gradient is known. *J. Pysiol.* **127**, 553–563.

Xin, J. 2004 Dispersive instability and its minimization in time-domain computation of steady-state responses of cochlear models. *J. Acoust. Soc. Am.* **115** (5).

Yamauchi, A., Rabbitt, R., Boyle, R. & Highstein, S. 2001 Relationship between inner-ear fluid pressure and semicircular canal afferent nerve discharge. *JARO* **3**, 24–44.

Yoon, Y.-J., Puria, S. & Steele, C. 2007 Intracochlear pressure and derived quantities from a three-dimensional model. *J. Acoust. Soc. Am.* **122** (2), 952–966.

Zhou, G., Bintz, L., Anderson, D. Z. & Bright, K. E. 1993 A life-sized physical model of the human cochlea with optical holographic readout. *J. Accoust. Soc. Am.* **93** (3).

Index